Design of a Single-Sided Axial Flux PM In-Wheel Electric Vehicle Machine with Non-Overlap Stator Windings

Harold Junior Kierstead

Thesis presented in fulfilment of the requirements for the degree
Master of Science in Engineering at the
Stellenbosch University

Supervisor: Professor Maarten J. Kamper

December 2009

Declaration

By submitting this thesis electronically, I declare that the entirety of the work contained therein is my own, original work, that I am the owner of the copyright thereof (unless to the extent explicitly otherwise stated) and that I have not previously in its entirety or in part submitted it for obtaining any qualification.

Date: November 20 2009

.....

Harold Junior Kierstead

Abstract

With the current worldwide energy problems electric vehicles are set to replace conventional combustion engine vehicles. Electric vehicles with gearless in-wheel mounted brushless permanent magnet motors provide a more flexible and efficient means of vehicle propulsion but the electric motors, particularly the non-overlap stator winding type have not been fully researched.

This study focuses on the selection and design of suitable in-wheel hub drive machine. Several machine topologies are evaluated and the single-sided axial flux machine is chosen. The average vehicle requirements are determined and design optimisations are carried with the aid of finite element analysis and an optimisation algorithm. A comparison of torque quality between single-layer and double-layer machines is carried out and it is found that double-layer machines have the least torque ripple and single-layer machines with un-equal teeth the best torque per ripple characteristics. A 16 kW, 30-pole 27-slot prototype machine optimised for power density is built, and it is found fitting for the application meeting the design requirements. The prototype machine is extensively tested and good agreement is found between finite element and measured results. The well known axial flux attraction forces are encountered in the prototype machine and they are overcome by suitable bearing selection and mechanical design. It is found that theoretical and measured cogging torques are inconsistent, the reason for this is that practical machines are not absolutely ideal due to material and manufacturing tolerances. Excessive rotor losses are found in the prototype machine and appropriate methods for their reduction are presented. This work does not aim to find the best in-wheel hub drive solution, but instead looks to uncover some of the technical available solutions.

Opsomming

Met die huidige wêreldwye energie probleme, is elektriese voertuie bestem om konvensionele binnebrandenjin voertuie te vervang. Elektriese voertuie met ratlose binnewiel-geleë borsellose permanente magneet motors, voorsien ‘n meer aanpasbare en effektiewe metode van voertuig aandrywing, maar die elektriese motors, veral die oorvleulende stator winding tipe is nog nie ten volle nagevors nie.

Hierdie studie fokus op die keuse en ontwerp van ‘n binnewiel aandryf masjien. Verskeie masjien uitlegte word geëvalueer en ‘n enkelkant aksiaalvloed masjien is gekies. Die gemiddelde voertuig behoeftes word bepaal en ontwerp optimalisering word uitgevoer met behulp van eindige element analise en ‘n optimaliserings algoritme. Enkellaag en dubbellaag masjiene se draaimoment kwaliteit word vergelyk. Die bevinding is dat dubbellaag masjiene die laagste draaimoment rimpel toon terwyl die enkellaag masjiene, met oneweredige tande, die beste draaimoment per rimpel karakteristieke toon. ‘n 16 kW, 30 pool, 27 gleuf prototipe masjien, wat vir drywingsdigtheid ge-optimaliseer is, is gebou en is geskik vir die toepassing en die vereistes. Die prototipe masjien is getoets en goeie vergelykings word getref tussen die eindige element analise en die gemete resultate. Die alom bekende aksiaal vloed aantrekkings kragte word in die prototipe masjien gesien en word oorkom deur die regte rollaer keuse en meganiese ontwerp. Nog ‘n bevinding is dat die teoretiese en gemete waardes vir die vertandings draaimoment nie ooreenstem nie. Die rede hiervoor is dat die praktiese masjien nie ideaal is in terme van materiaal en vervaardigings toleransies nie. Groot rotor verliese in die prototipe masjien is gevind en goeie metodes vir die minimering daarvan word voorgestel. Hierdie werk is nie ‘n soektog na die beste binnewiel aandrywings oplossing nie, maar mik eerder om sommige van die tegniese beskikbare oplossings te onthul.

Acknowledgements

I wish to express my sincere gratitude to:

Jesus Christ our Lord and Saviour. Without you we would all be lost.

Professor Maarten J. Kamper for his insight, support, and with giving me the opportunity to study in his research group.

Dr Rong-Jie Wang for his help with finite element programming and creative deliberation during the project.

Dr Edward Rakgati at the University of Botswana, for motivating me to pursue this study and for giving me constant support.

Mr. Arnold Rix for his assistance and in setting up of the DSP controller.

The technical personnel of the Electrical Engineering Faculty Mr. A. Swart and Mr. P.H. Petzer for their help with technical support during the building of the prototype machine.

My fellow colleagues at the Electrical Machines Laboratory for their support, help and companionship.

The South African Nation Energy Research Institute for funding the project.

Lionah Cleopatra Ockhuizen, for her endearing love and companionship.

My family for their patience and understanding during my absence from home, particularly my father Harold Rodney Kierstead.

Table of Contents

List of Figures

List of Tables

List of Symbols and Abbreviations

Symbols

F_{te} - tractive effort force

F_{rr} - rolling resistance force

F_{ad} - aerodynamic drag force

F_{hc} - gradient / slope force

T - torque, **Nm**

μ_{rr} - coefficient of rolling resistance

m - mass, **kg**

g - gravity, **m/s**

ρ_a - air density, **kg/m^3**

C_d - drag coefficient

I - moment of inertia, **kgm^2**

r - radius, **m**

J - current density in the stator conductors, **A/mm^2**

v - instantaneous voltage, **V**

i - instantaneous current, **A**

λ - flux linkage, **Wb-turns**

R_s - stator phase resistance, **Ω**

L - inductance, **H**

Ψ - current angle

A - end winding area, **m^2**

α - slot width, **m**

h - tooth width at outer diameter

L_{ce} - end winding length

Q - number of stator slots

$2p$ - number of machine poles

k_w - winding factor

k_d - distribution factor

k_p - pitch factor

m - number of phases

u - number of coils per phase group

N_s - number of series turns per phase

E - induced electromagnetic force, **V**

f - frequency, **Hz**

ϕ - flux per pole, **Wb**

B_{avg} - average magnetic flux density, **T**

ρ - material resistivity, **Ωm**

L - total conductor length per phase, **m**

A_{con} - single conductor area, $\mathbf{m^2}$

w - active stack length, **m**

P_{cu} - copper loss in stator windings, **W**

N_p - number of parallel circuits

A_{slot} - active slot area, $\mathbf{m^2}$

k_f - fill factor of stator coil conductors

N_{slot} - number of conductor per slot

P_e - stator winding eddy current loss, **W**

P_{core} - stator core losses, **W**

B_{mt} - maximum flux density in the stator teeth, **T**

B_{my} - maximum flux density in the stator yoke, **T**

M_t - stator teeth mass, **kg**

M_y - stator yoke mass, **kg**

P_{PM} - permanent magnet loss, **W**

P_{rot} - rotor core losses, **W**

P_{mech} - mechanical losses

P_{tot} - total machine losses

η - efficiency, **%**

k_{TW} - inner to outer tooth width ratio

Y - optimisation objective

w_i - weighting factor

ε_i - penalty function

D_o - outer machine diameter, **m**

D_i - inner machine diameter, **m**

k_d - diameter ratio

L_{eff} - effective stack length, **m**

r_{avg} - average radius, **m**

h_Y - stator yoke height, **m**

h_S - stator slot height, **m**

h_M - magnet height, **m**

h_R - rotor yoke height, **m**

w_T - stator tooth width, **m**

w_S - stator slot width, **m**

w_M - magnet width, **m**

α_i - magnet to pole pitch ratio

τ - pole pitch

k_s - number of computational planes

H_c - coercivity, **A/m**

μ - permittivity, **N/A^2**

R_c - core loss resistance, **Ω**

k_{ST} - stator slot to tooth width ratio

e - instantaneous back electro magnetic force, **V**

I_{sc} - short circuit current, **A**

X_s - per phase synchronous reactance, **Ω**

Abbreviations

EV	Electric Vehicle
PM	Permanent Magnet
DC	Direct Current
AC	Alternating Current
EMF	Electromotive Force
BLDC	Brushless Direct Current
BLAC	Brushless Alternating Current
PWM	Pulse Width Modulation
RFPM	Radial Flux Permanent Magnet
AFPM	Axial Flux Permanent Magnet
FE	Finite Element
FEM	Finite Element Modelling
SMC	Soft Magnetic Powder Composites
MMF	Magneto Motive Force
FOC	Field Orientated Control
MTPA	Maximum Torque Per Ampere
GCD	Greatest Common Divisor
LCM	Least Common Multiple
SL	Single-Layer
SLu	Single-Layer with Un-Equal Teeth
DL	Double-Layer
GOSS	Grain Orientated Silicon Steel
DSP	Digital Signal Processor

1. Introduction

Electrical machines are electromagnetic devices which convert electrical power to mechanical power or mechanical power to electrical power. The two conversions are more generally know as motoring and generating respectively. For purposes of vehicle propulsion, the motoring regime is of particular interest. Since the 1800's, electric machines for vehicle propulsion started gaining interest. By the 20th century, electric cars and trains were commonplace. Today in the 21st century, many companies offer hybrid / electric vehicles to the public. With escalating fuel costs, uncertainty to future energy resources, stricter emission regulations and technological progress, hybrid / electric vehicles are destined to replace internal combustion vehicles.

There are two major ways of coupling electric machines to a vehicle drive train; machines could be either:

- Conventional: Similar to typical combustion vehicles with combustion engine replaced by electric motor, as shown in Figure 1.
- In-wheel: With hub mounted in-wheel electric motors, either geared or directly driven as shown in Figure 2.

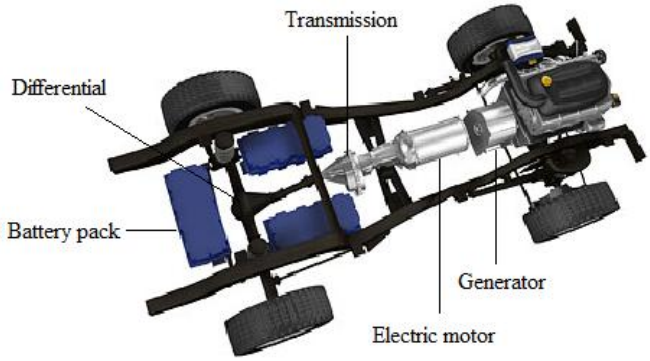

Figure 1. Conventional series hybrid drivetrain layout of Hummer ER-EV H3 Hybrid.

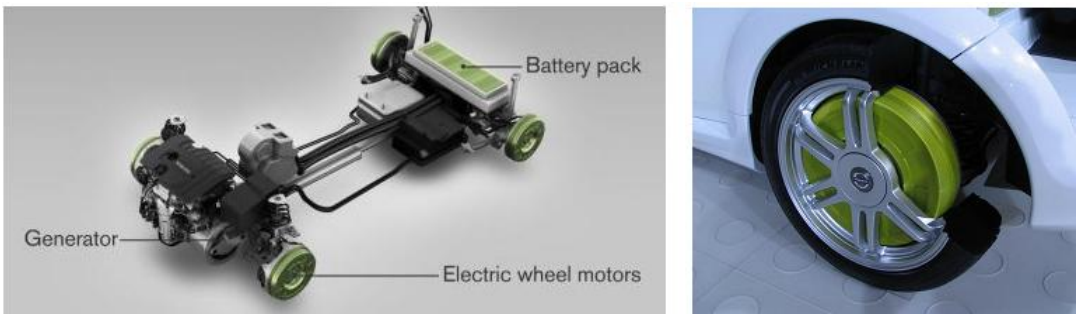

(a) (b)

Figure 2. In-wheel layout of Volvo C3 ReCharge Hybrid EV, a) chassis view and b) in-wheel motor.

Currently all automotive manufacturers are competing head to head in hybrid / eclectic vehicle development. Toyota currently markets several hybrid vehicles, most commonly, the Toyota Prius hybrid, which is powered electrically by a single 50 kW brushless permanent magnet (PM) machine with a power split hybrid drivetrain [1]. GM also is investigating electric vehicles, chiefly being the Chevy Volt power by a 120 kW PM motor [2]. GM research development also includes a S10 truck; it has been built and tested using two 25 kW toroidal in-wheel axial flux brushless PM machines and a front mounted induction motor gearbox drive [2] [3]. Raser Technologies in 2009 unveiled an extended range hybrid H3 Hummer driven by a 200 kW induction machine as shown in Figure 1 [4]. Volvo and Protean Electric Ltd in 2007 unveiled a Volvo C3 hybrid with four in-wheel PML Flightlink Hi-Pa Drive^{TM} units as shown in Figure 2. The top of the range PML Flightlink wheel drive unit is a 24-phase 120 kW brushless PM unit [5].

Conventional layouts with chassis mounted machines provide excellent protection from the harsh conditions endured by vehicle wheels. By having machines chassis mounted they are mechanically protected by the damped vehicle suspension. The placement of machines is flexible within the vehicle body and enclosing them is possible to further protect from environmental conditions. The setback with the conventional layouts is the fact that they utilise additional components such as transmissions, differentials and drive shafts to direct torque to the drive wheels. These associated components increase complexity, enlarge the vehicle layout, add extra mass and take up valuable space, essentially reducing the overall reliability and efficiency of the vehicle. In-wheel hub motors have unique features to counter some of these disadvantages.

1.1 In-Wheel Hub Machines

In-wheel hub mounted machines are fitted within the vehicle wheels and drive the wheels directly or driven through reduction gears. In-wheel hub machines have the advantages of weight savings, reduced drive-line components, simple mechanical layout, and possible improved overall efficiency [6] [7] . The gearless direct hub drive system has further reduced drive line components, significantly simplifying the mechanical layout since gear reductions are not used [3] [8].

In-wheel hub machines also allow flexibility with the design of the vehicle interior and front/rear compartments. Without chassis mounted machines and drive line components, the vehicle can have a flat floor and empty front/rear compartments. The additional space and flat floor could provide endless design innovations essential in the automotive industry.

Safety is another key factor the automotive industry; by being able to direct each wheel independently stability systems can be immensely improved. In-wheel machines are also extremely adaptable as one modular in-wheel hub machine design could be used for several vehicle models, standardising vehicle production. The production of two and four wheel drive arrangements would also be greatly simplified by their use.

As with all systems there are always obstacles, and those affecting in-wheel hub motors are:

- Harsh vibrations and shocks, due to no shock absorbing media.
- The limited space availability within the wheel rim [3] [9].
- Having to supply high torque directly at low speed, requiring a high number machine poles [3] [10].
- Un-sprung mass must be minimal, to avoid handling and stability problems [3].
- Flexible cabling is required, particularly if part of the steering system.
- Mechanical brake integration, for safety and parking.

1.2 Brushless Permanent Magnet Machines

Traditionally, DC motors were used for traction due to their inherent variable speed capability, but with the development of high power semiconductor devices, asynchronous and synchronous AC machines are now the preferred choice.

Currently brushless PM drives are being immensely used in vehicle applications due to their high efficiency, high power density, high overload capability, compact size, simple maintenance, regenerative features, and ease of control [3] [6] [11] [12]. In particular for direct drive applications requiring low speed high torque machines, brushless PM machines are the best choice [9].

Brushless PM machines are essentially synchronous machines with performance characteristics of DC shunt machines. Structurally they have three-phase windings placed upon the stator as with synchronous machines, but their rotor excitation is provided by permanent magnets instead of a field winding. This feature eliminates rotor copper losses and mechanical commutator brushes; leading to higher power densities and reduced maintenance [13]. Brushless PM machines can also be constructed in many non-standard shapes and sizes, which is a good advantage in the automotive industry [14]. The two main distinct shapes of brushless PM machine are the radial flux and axial flux topologies shown in Figure 3. The names are derived upon the flux direction within the machines airgap.

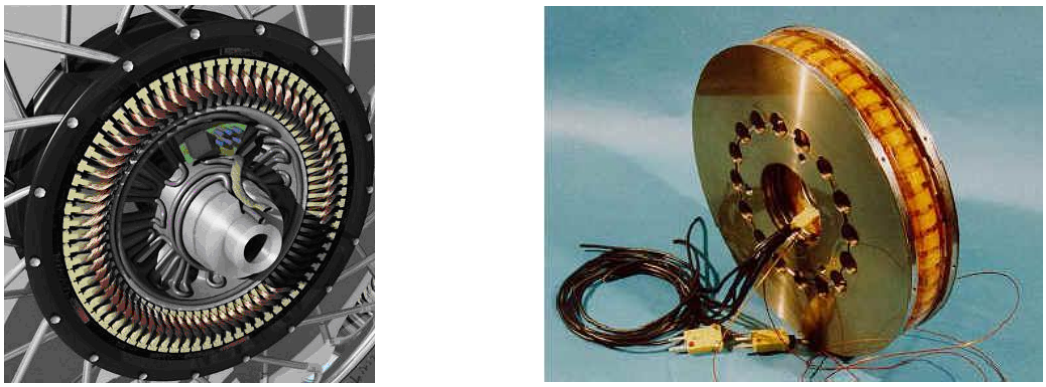

(a) (b)

Figure 3. Two main machine topologies, a) radial flux and b) axial flux.

Brushless PM machines can also be designed to either have square / trapezoidal or sinusoidal back electromagnetic force (EMF) waveforms by respectively using concentric or sinusoidal distributed windings. Machines with square-wave back EMF are commonly referred to as brushless DC machines (BLDC), and those with sinusoidal back EMF as brushless AC (BLAC) or synchronous PM.

1.2.1 Non-Overlap Windings

Brushless PM machine stators can hold either non-overlap or conventional distributed type windings as shown in Figure 4. Non-overlap windings are made up of individual preformed coils as shown in Figure 5. The coils are placed in a manner that the end windings do not overlap. Non-overlap windings provide significant advantages over distributed type windings. By using pre-formed coils, the end windings of a machine can be significantly shortened and manufacturing is simplified. This shortening leads to a reduced copper mass and copper loss leading to higher machine efficiency [12] [15]. Due to limited space available for hub drives, non-overlap windings with their small end winding build are particular suited for the application.

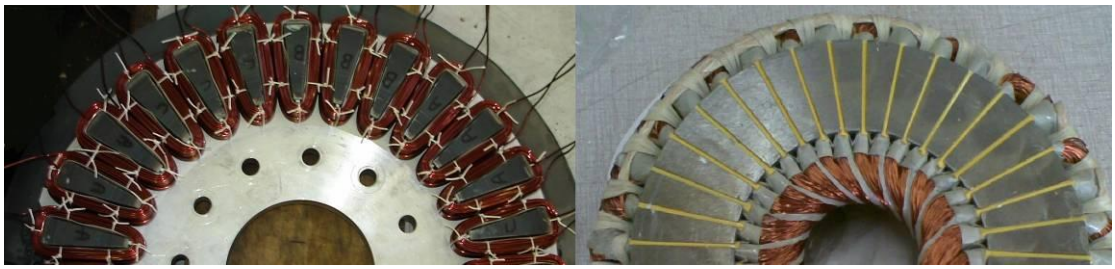

(a) (b)

Figure 4. Axial flux machine stators: a) double-layer non-overlap winding with open slots, b) distributed winding with semi-closed slots.

Figure 5. Non-overlap winding pre-formed coil.

1.2.2 Brushless PM Machine Drives

Unlike other electric machines which are run directly off voltage sources, brushless PM machines require power electronic control circuits (drives) for their operation. The typical drive system of a brushless motor is shown in Figure 6. In applications, such as battery electric vehicles, there is no AC rectification to provide DC, and DC is provided by batteries. A DC to AC inverter is then used to provide variable frequency / voltage to the motor by pulse width modulation (PWM) switching via high power semiconductor switches. The controller directs the operations of the inverter by comparing desired commands from the user and feedback sampled motor currents. A position sensor is usually included in the feedback loop so as to ensure correct synchronisation of phase currents with respect to the rotor position. The whole process can be thought of a kind of "electronic commutation", similar to the role played by commutator brushes in traditional DC machines. These extra systems have previously been against brushless PM machine development, but with the advances in power electronics, semiconductor materials, sensor-less synchronisation and decreasing costs, brushless PM machines are becoming more commonplace in the automotive industry.

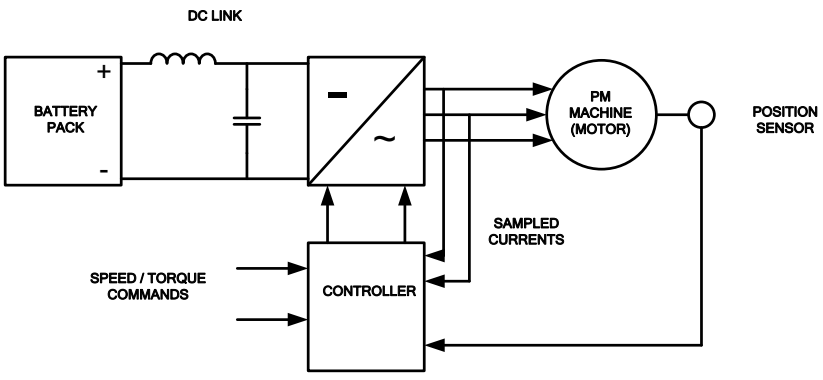

Figure 6. Battery powered brushless PM machine drive layout.

Without any control brushless PM drives have torque speed characteristics that are rather rectangular as compared to the desired traction characteristics shown in Figure 7. This is due

to the fact that as rotor speeds increase, the back EMF voltage increases to a point where the maximum output voltage of the inverter is reached, at this point the maximum speed of the machine is also reached, termed base speed. Further trying to drive the machine beyond its base speed (ω_b) leads to a collapse in machine torque, and damage to the bus capacitors as the higher back EMF is then rectified by the inverter diodes back to the DC bus. This characteristic is a main disadvantage of brushless PM drives used for traction applications. The reason for this is because the flux produced by PMs is constant and cannot be controlled like in machines with field windings. Previously, the only solution to obtain higher drive speeds was to increase the inverter size, but currently there are control techniques such as flux weakening to counter this problem as discussed in Section 3.2.

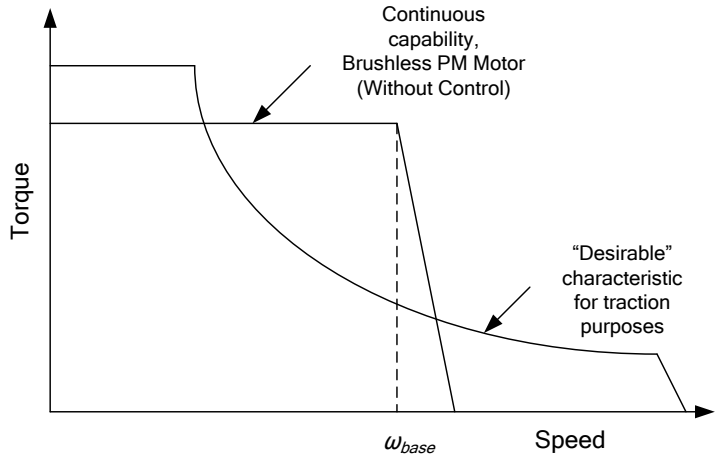

Figure 7. Torque-speed characteristics of PM machine versus desirable traction characteristics.

Analogous to brushless PM machines, brushless PM drives can have square-wave currents (BLDC) or sinusoidal wave currents (BLAC). The main difference between BLDC and BLAC drives is the switching scheme of the inverter. Both inverters utilise a standard three-phase inverter with six transistor switches. In order for optimal utilisation, the machine back EMF should match the inverters switching scheme.

On the machine level, there is no remarkable torque density difference between BLDC and BLAC drives. BLDC drives are simple to implement and do not require an expensive position sensor, but they draw higher currents implying higher copper losses and have commutation problems at higher speeds. BLAC drives are shown to be more efficient than the BLDC drives; in addition BLAC drives have the capability of producing smoother torque at higher speeds with reduces audible noise. In-wheel hub drives require good high speed (flux weakening) operation; therefore BLAC drives are better suited [16].

1.3 Radial Flux PM Machines and Topologies

The radial flux machine is the most familiar machine type recognised with its cylindrical shape. A flow chart showing the different radial flux machine topologies is show in Figure 8. The radial flux permanent magnet (RFPM) machines are classified based upon their rotor / stator configuration, and type of stator. The machine stators are made of laminated steel with either slotted or slotless windings. In double-sided and multistage machines, there are possibilities of coreless stators and rotors. Coreless stators refer to the fact that they are not built with ferromagnetic materials and are normally built using epoxy-encapsulated windings.

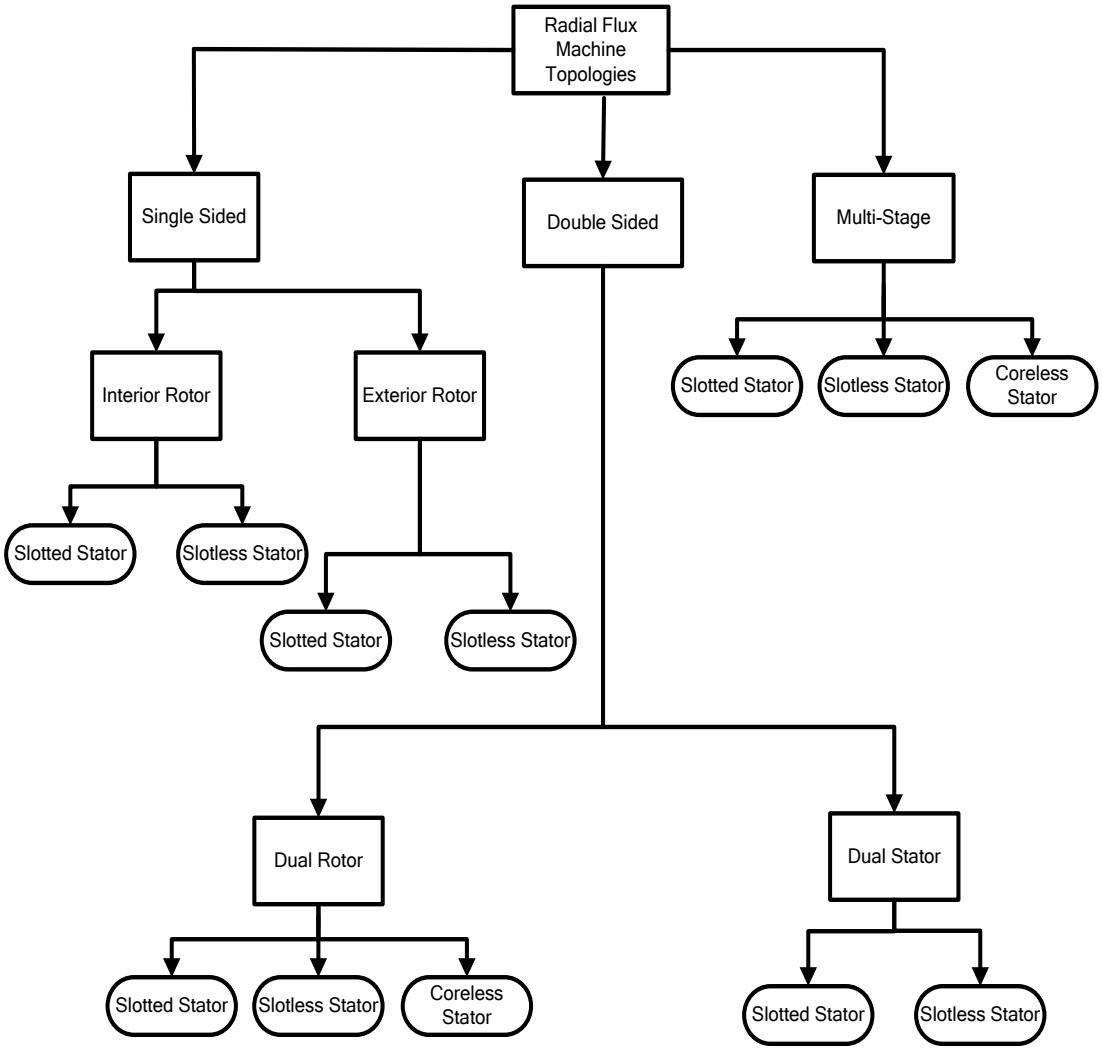

Figure 8. Radial flux machine topologies.

1.3.1 Single-Sided Radial Flux Machines

RFPM machines come in two main topologies, the interior rotor configuration (Figure 9) and the exterior rotor configuration (Figure 10). The interior rotor machine is realised by a cylindrical outer body, the stator, and an inner drum-type body, the rotor which carries the PMs. The stator of the interior rotor machine closely resembles that of a conventional induction machine. In the exterior rotor configuration, the positions of the rotor and stator are swapped (turned inside out). The rotor is then an outer ring/cup supporting the PMs, while the stator is an inner rigid body closely resembling that of a DC brush type armature.

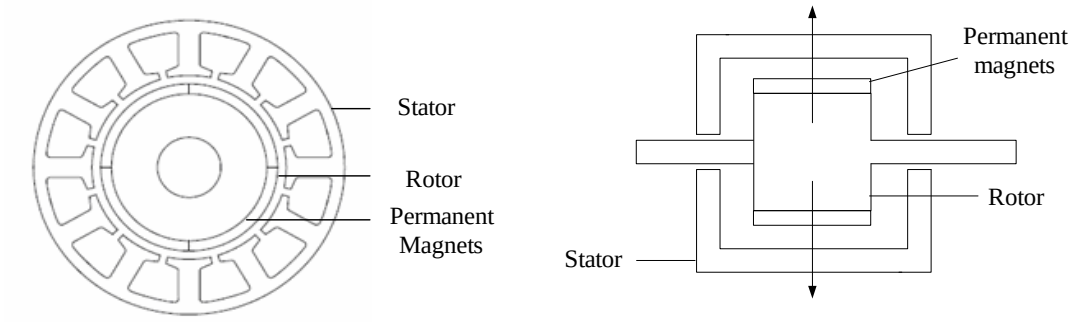

Figure 9. Interior rotor RFPM machine a) end view and b) side view (arrows show flux direction).

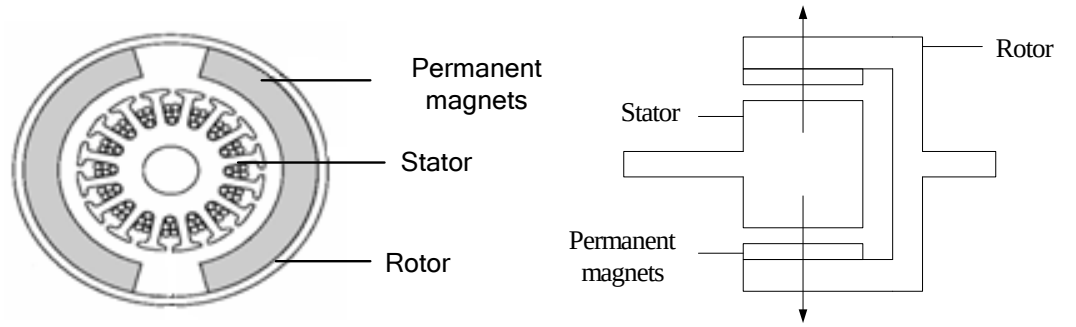

Figure 10. Outer rotor RFPM machine a) end view and b) side view (arrows show flux direction).

Interior rotor RFPM machines do not have many advantages over other RFPM machines as hub drives, except for the fact that they are cheap and easily sourced. Outer rotor configurations offer cost effective use of magnets, simple stator windings, possible single bearing configurations and improved quietness over the interior rotor machine [10]. The working airgap diameter in outer rotor machines is larger, thus a greater torque is achieved for the same volume. They are also easy to manufacture, have good performance in applications

requiring continuous operation, and mechanically couple well with a vehicle rim due to their large diameter.

1.3.2 Double-Sided Radial Flux Machines

The double-sided RFPM are machines which have either two rotors one stator or two stators one rotor, for example two rotors and one stator shown in Figure 11. Double-sided RFPM machines have high power density levels than the single-sided machines due to better winding utilisation, but these machines require more magnet material and are somewhat more complicated to design.

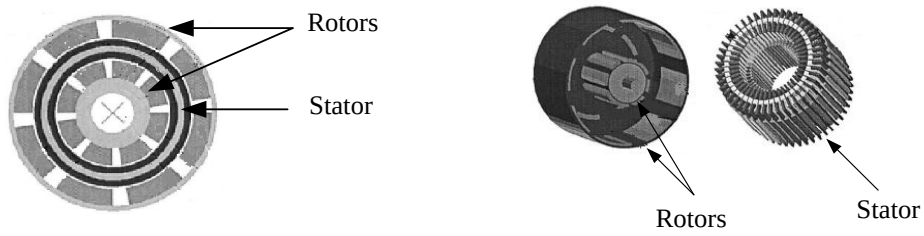

(a) (b)

Figure 11. Double-sided RFPM machine a) end view and b) 3D dismantled view.

1.3.3 Multistage Radial Flux Machines

Multistage RFPM are machines which have a combination of stator(s) and rotor(s) as shown in Figure 12. Multi-stage RFPM machines have the highest overall power density levels but are impractical due to their complex manufacturability [10].

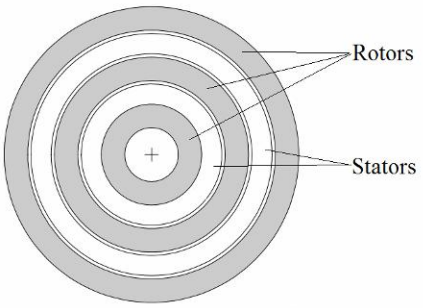

Figure 12. End view of multistage radial flux machine.

1.4 Axial Flux PM Machines and Topologies

Axial flux permanent magnet (AFPM) machines are realised as flat pancake like structures, with disk shaped stators and rotors as shown in Figure 14. The active part of the machine is from the inner radius to the outer radius. AFPM machines are a fairly recent development and only started becoming of interest in the mid 70's [17] and are currently of great interest as alternatives to radial flux machines. The use of AFPM machines is increasing due to their compact flat shape, ideal applications requiring such a profile. AFPM machines are more involving to build, but their demand is increasing as the complexities of manufacture are being solved [18]. Similar to radial flux machines, AFPM machines are also classified based upon their rotor / stator relation and stator structure. Just like RFPM machines, AFPM stators can be made of laminated steel with either slotted or slotless windings, with possibilities of coreless stators and rotors in double-sided and multistage machines. The chart in Figure 13 outlines most of the different configurations.

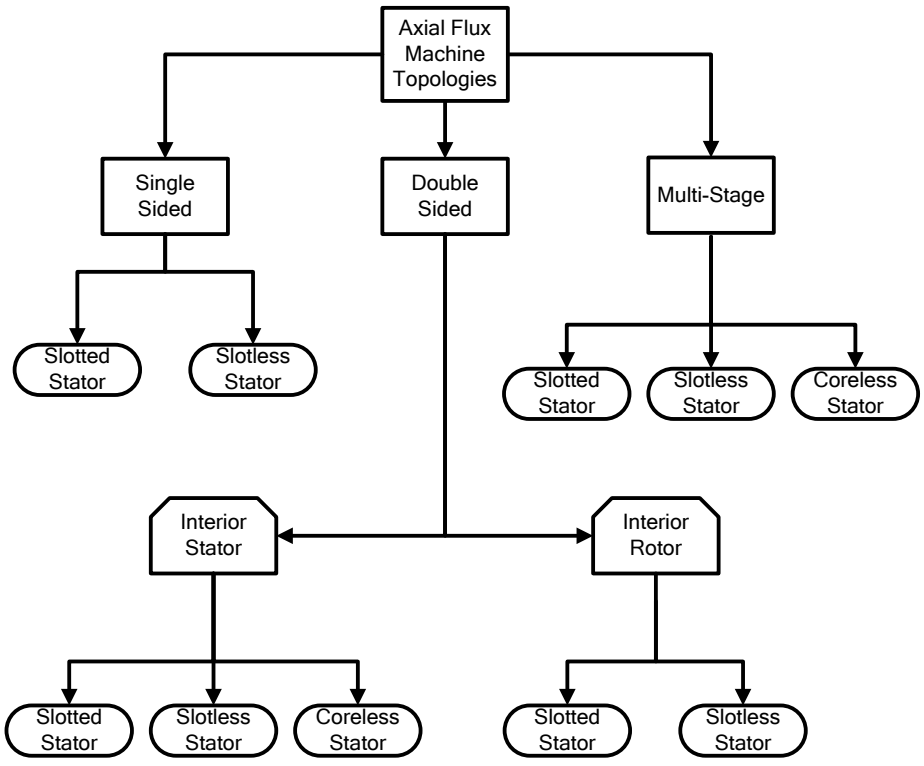

Figure 13. Axial flux machine topologies.

1.4.1 Single-Sided Axial Flux Machines

Single-sided axial flux machines are of the one stator one rotor configuration shown in Figure 14. The single-sided axial flux machines have the main advantage of simplicity. The machines are simple to design, manufacture and assemble. Despite their simplicity, they have lower torque densities and poor copper utilisation compared to other axial flux topologies [13]. The main drawback of the topology is the major attractive force problem; due to the magnet flux being from one side only, the attractive forces cause high bearing losses and bending of the yokes.

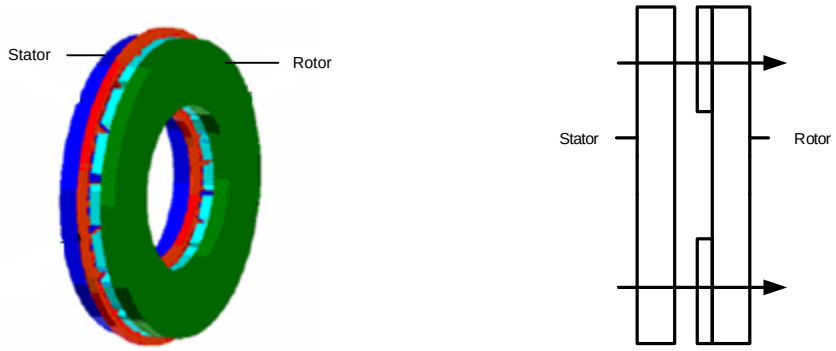

(a) (b)

Figure 14. Single-Sided AFPM machine a) 3D view and b) side view (arrows show flux direction).

1.4.2 Double-Sided Axial Flux Machines

The double-sided AFPM machines form a large diverse group, with either interior stator or interior rotor as shown in Figure 15. Double-sided AFPM machines are advantageous as hub drives because they have good torque density due to double-sided configuration, the attractive forces can be somewhat balanced from both sides and they have twice the air gap area of single-sided machines leading to higher power densities [13]. The main disadvantage of double-sided machines is that they are more complicated to build and assemble.

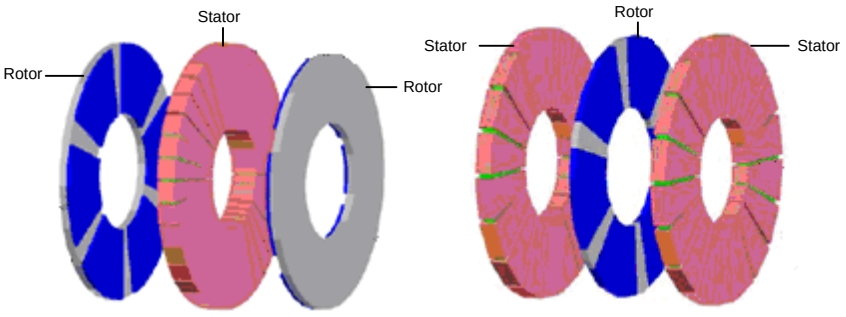

(a) (b)

Figure 15. Double-sided AFPM machines: a) interior stator machine and b) interior rotor machine.

1.4.3 Multistage Axial Flux Machines

Multi-stage AFPM machines, like RFPM multi-stage machines, are simply a combination of stator(s) and rotor(s), for example three stators and four rotors as shown in Figure 16. Multistage AFPM machines have many advantages such as having the highest overall power density [13]. Their structure can overcome restriction of rim diameter [9] and their multiple stators can be used to a controller advantage, by having possible series and parallel connections. Multistage AFPM machines are not impractical like the multistage RFPM machines, as all the multiple parts are all of the same size and are stackable. This stackable feature is very advantageous as existing machines can be upgraded by simple addition of more stators or rotors. Although very capable, they have several drawbacks such as complicated configuration, design and assembly. Further they require a lot of magnet material.

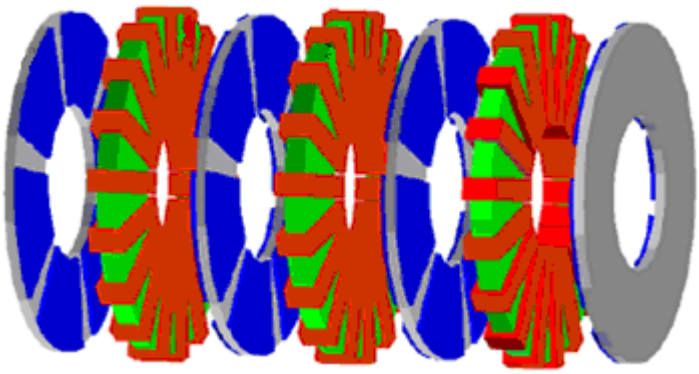

Figure 16. Multi-stage AFPM machine with slotless toroidal stators.

1.5 Literature Comparison of RFPM and AFPM Machines

Several studies on radial and axial flux machines have been carried out in literature, some of the studies are herein highlighted. Further in section 1.5.1 the important characteristics of the various machines with particular relevance to hub drives is summarised.

There have been many previous attempts at comparing the performance of AFPM machines with that of RFPM machines. Traditionally in literature, comparison between electric motors is performed by using “sizing equations” [19]. Sizing equations link electromagnetic torque to machine length and diameter through coefficients depending on the machine material. The coefficients and magnetic loading are chosen based upon experience. For new machine prototypes, this presents a problem as this “experience” is often not available [20].

Huang et al [21] did a comparison of a toroidal and a two stator internal rotor AFPM machine to the general induction machine on the basis of power density using general purpose sizing equations. The results show that the two AFPM machines have higher power densities over the common induction machine, with the toroidal machine achieving the highest overall power density.

Cavagnino et al [20] proposed comparing the different machines on a basis of simple thermal considerations as compared to traditional sizing equations. The two motor topologies are compared in terms of electromagnetic torque. The results show that, when axial length is very short and pole number high, the axial flux machine can be an attractive alternative to the conventional radial flux machine. The comparison did not investigate manufacturing problems.

Profumo et al [22] investigated three axial flux machine topologies for hub drive applications: the axial flux induction, surface PM, and interior PM machines. A comparison of the axial flux induction machine was done with respect to the radial flux induction machine. Comparison of the axial flux machines to radial flux machines was not carried out. It was stated that "because of the structural differences in PM machines, the PM quantity can be very different for the two cases and the power density comparison seems to be difficult at this stage".

Sitapi and Krishnan [23] also did performance comparisons on RFPM and AFPM machines. For the comparison several parameters were selected and held constant in the analysis, and sizing equations were not used in the comparison. It was concluded that axial flux machines have very high power densities and lower weight, compared to radial flux, machines which showed higher values of inertia. On the magnet material comparison, it was shown that slotless machines required more magnet material than the slotted machines. In terms of copper losses, slotless machines recorded higher figures than slotted machines.

In general, it is alleged that a comparison is not possible due to the large number of possible technical solutions, but a detailed performance comparison is required to help in determining the best machine suited for particular applications [23].

1.5.1 Comparison Specifically as Hub Drives

The previous section highlighted literature of general machine comparison without looking specifically to application, this section on literature relates specifically to the integration of the axial and radial flux to hub drive applications. As hub drives, radial flux machines have several advantages compared to their axial flux counterparts. They have higher field intensities across the stator winding due to a better magnetic path [24]. They are simpler and cheaper to manufacture due to their dominance in the motor industry. They are more robust than axial flux machines and have no problems with attractive forces between the stator and rotor.

The disadvantages of radial flux machines are that the radial machine shape offers few topologies. They also have lower power densities than axial flux machines, and the number of poles is limited by machine diameter [24].

As hub drives, the axial flux machines are more advantageous than radial flux machines primarily due to profile of the available space within a wheel as shown in Figure 17. AFPM hub drives machines offer higher efficiencies and specific torque for placement within the vehicle wheel [11] [3] [13]. Other advantages include that the motor can be mounted in the wheel, where there is insufficient axial length for end windings in radial field design [11]. Rotating rotor magnets could be mounted on wheel side walls [11]. The stationary stator winding could be mounted centrally on the axle [11]. Windings and magnet discs could be manufactured on flat formers [11]. They have higher power to weight ratios, resulting in less core material and higher efficiencies [20] [22] [25]. They are smaller in size and have disk shaped rotor and stator structures, crucial for hub drive applications having size/space limitations. They also have planar and adjustable airgaps [25]. Significant volume savings over radial flux machines [25]. Inherently good low speed high torque characteristics [25]. The direction of main airgap flux can be varied, and many discrete topologies can be derived [13] [22] [25] and they have large diameters; hence they can accommodate large pole numbers.

The disadvantages of the AFPM machine include, that they are not as robust as radial flux machines. Their manufacturing is not as easy as radial flux machines, leading to higher costs (particularly the stator). They have strong attraction forces, which are not a problem in radial flux machines and their torque is function of radius; and radius is limited in hub drive applications [3].

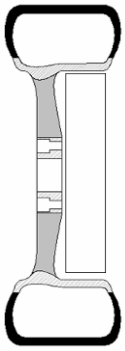

Figure 17. Cross section of vehicle rim showing available space for hub machine.

1.6 Problem Statement

Based on the current literature reviewing the different machine topologies and types it is unclear as to which machine(s) are best suited for hub drive applications. Brushless PM machines come in many variants and the integration of these as in-wheel hub drives has not been fully researched, therefore it is important to investigate some of the options available. The foremost issues that this thesis wishes to address are with respect to:

- Selection of suitable machine topologies.
- The mechanical integration of the electrical machine to the vehicle wheel.
- Construction and manufacturing of axial flux electrical machines.
- Compare some of the solutions available.
- Investigate the new technology available for electrical machines, particularity non-overlap PM machines.
- Utilise new design techniques like finite element analysis and optimisation.
- Prior to this work, two radial flux outer rotor PM in-wheel machines had been developed at the University of Stellenbosch, therefore there is a need to investigate the other options available.

1.7 Approach to the Problem

To solve the problem of selecting a suitable hub drive machine, a general literature review was carried out previously. Following this the typical requirements of an average vehicle will be sought out to find the general performance figures needed. With the typical performance required known, different machine topologies will be looked at with particular emphasis to mechanical integration to an electric vehicle, the most suited will be selected for further investigation.

The theory and control of brushless PM machines will then investigated, in order to further narrow down the search for suitable machines. Once several appropriate machines are identified, they will be modelled and designed with the aid of finite element modelling. Further the designed will subjected to an optimisation algorithm, to further fine tune designs. Once several design proposals available, one will be selected to be implemented into a working prototype machine. This prototype machine will then be tested to verify its design and find any anomalies. Conclusions of the overall findings will be drawn and any recommendations for future study.

This work does not aim to find the best machine out there as each machine type has its own set of distinct advantages for this application; instead this work looks to uncover some of the available solutions.

1.8 Thesis Layout

Following the introduction to in-wheel hub machines and the PM machine topologies available, the remainder of this thesis is as follows:

Chapter 2: In this chapter vehicle dynamic modelling is carried to determine the average requirements of a typical small vehicle, followed by mechanical integration solutions. Several machines topologies are proposed and one selected. Construction challenges of axial flux machines are also investigated.

Chapter 3: This chapter covers the main theory of brushless PM machines with non-overlap windings. The machine *d-q* models are derived and their relevance for control explained. Pole-slot combinations are covered along with machine losses.

Chapter 4: In this chapter the AFPM machine is designed with the aid of finite element modelling (FEM). An optimisation algorithm is used to further enhance the design and investigate torque quality.

Chapter 5: The design is verified by the building and testing of an AFPM prototype machine.

Chapter 6: Conclusions are drawn with recommendations for further research.

2. Hub Drive Requirements and Configurations

In this chapter the mechanical hub drive design criteria is laid out. Vehicle dynamic equations are used to find the traction requirements for an average family vehicle. The mechanical integration of several machine topologies is investigated, and one topology is selected for further evaluation. The challenges of axial flux construction methods are also highlighted.

2.1 Hub Drive Design Criteria

Electrical machines used in the automotive industry should be easy to install, service and maintain. The main key points of a hub drive design involve assessing the following:

- Vehicle performance data:
  -To design the drive according to the required performance.
- Wheel / rim size:
  -To know the size limitations of the hub drive motor.
- Thermal capacity:
  -To design for adequate cooling.
- Required mechanical strength:
  -Vehicles need robust, durable hub motor with good sealing.
- Max permissible un-sprung mass:
  -To design the drive to be within tolerable mass limitations of the hub.
- Mechanical coupling:
  -Need information on how the motor is to be coupled to the wheel.
- Auxiliary systems:
  - The make up of connecting cables and cooling pipes if necessary.
- Mass impact of system auxiliary equipment:
  -Performance reduction due the mass of batteries / generators / controller etc.
- Ease of maintenance:
  -Hub design should be done such that the hub motor is easy to maintain and service.
- Controller information:
  -To aid in motor sizing and selection.

2.2 Total Tractive Effort

In the design of traction drive motors for electric vehicles, the forces acting on the vehicle need be known. With these forces calculated, a suitable motor can be sized; performance refers to vehicle tractive effort, acceleration and top speed. The electric vehicle performance should at the very least allow it to blend in with ordinary city traffic [26].

Tractive effort (F_{te}) is the force that propels a vehicle ahead through the drive wheels. This force has to overcome:

- Rolling resistance (F_{rr}),
- Aerodynamic drag (F_{ad}),
- Gradients / slopes (F_{hc}) and
- Accelerate the vehicle.

The total tractive effort needed for the motor sizing is the sum of all the forces as shown in Figure 18, and can be written as [26],

$$F_{te} = \frac{T}{r} = \mu_{rr} mg\cos(\varphi) + \tfrac{1}{2} A\rho_a C_d v^2 + mg\sin(\varphi) + ma + I\frac{a}{r^2}. \qquad (2.1)$$

where μ_{rr} is the coefficient of rolling resistance, m the vehicle mass, g gravity, ρ_a air density, A vehicle frontal area, C_d the drag coefficient, v the vehicle velocity, φ the gradient of accent, r the wheel radius, I the rotor moment of inertia, and a the acceleration. For in-wheel motors

$$\frac{nT_n}{r} = F_{te}, \qquad (2.2)$$

where n is the number of in-wheel motors and T_n the total torque of a single in-wheel motor.

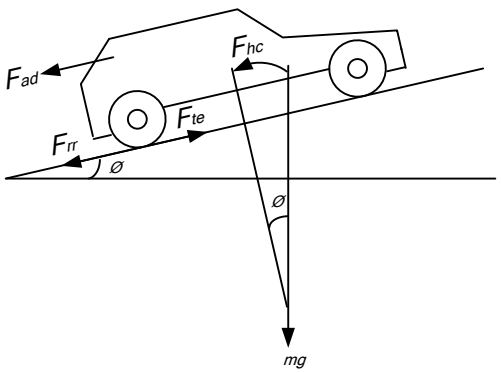

Figure 18. Forces acting on vehicle moving up a slope.

2.3 Vehicle Acceleration

Vehicle acceleration is a key performance indicator of all vehicles. For electric vehicles this is carried out under maximum torque conditions. There are two regions of operation for the PM motor namely at, $\omega<\omega_{base}$, where $T = T_{max}$ and $\omega\geq\omega_{base}$ where $T < T_{max}$. In the constant torque region, $\omega<\omega_{base}$, and assuming constant torque delivery, for a vehicle on level ground ($F_{hc} = 0$), air density $\rho_a = 1.25\text{kg/m}^3$ and from (2.1) noting $a = dv/dt$ we have [26],

$$\frac{T}{r} = \mu_{rr} mg + 0.625 AC_d v^2 + \left(m + I\frac{1}{r^2}\right)\frac{dv}{dt}. \tag{2.3}$$

With motor torque known, the equation can be reduced to a 1st order equation for velocity v. Once the constant torque region is passed ($\omega\geq\omega_{base}$) and operation is into the constant power flux weakening region, the torque in (2.3) is given by

$$T = T_{\max}\frac{\omega_{base}}{\omega} = T_{\max}\omega_{base}\frac{r}{v}. \tag{2.4}$$

For a well balanced performing electric vehicle, there needs to be optimal balance between the maximum speed, acceleration performance and travelling range [27]. In order to carry out vehicle performance modelling, a number of important characteristics of the proposed vehicle are required such as:

- Vehicle mass (including batteries and converter)
- Tyre rolling resistance
- Aerodynamic data
- Maximum gradient required to climb
- Desired Acceleration

2.4 Tractive Effort Case Study

The following example investigates the performance requirements of a typical small vehicle with the following specifications:

- 2000 Model Opel Corsa 140i

  Vehicle mass: 982 kg

  Rolling resistance coefficient of tyres: 0.015

  Number of wheels: 4

  Wheel radius: 0.267 m (195/50-R15 tyre)

  Vehicle frontal area: 2.28 m^2

  Drag coefficient: 0.32

From (2.1), considering constant velocity, the total tractive effort can be arranged as

$$\frac{T}{r} = \mu_{rr} mg\cos(\varphi) + 0.625 AC_d v^2 + mg\sin(\varphi)\,. \tag{2.5}$$

By plotting torque against velocity for several road gradients, the graph of Figure 19 is obtained. Depending on the required specifications, the required torque can be selected directly from the graph. In this particular case, the vehicle must be able to cruise on a flat road at 120 km/h and up a 6 % gradient (typical maximum on highways) at 80 km/h. This corresponds to a torque of 174 Nm on a flat road at 120 km/h and 367.3 Nm for 80 km/h on a 6 % gradient. The hub motor top speed can be calculated from the highest required velocity, at 120 km/h,

$$\frac{v}{r} = \frac{33.33}{0.267} = 124.8\,rad/s = 1191.75\,r/\min\,. \tag{2.6}$$

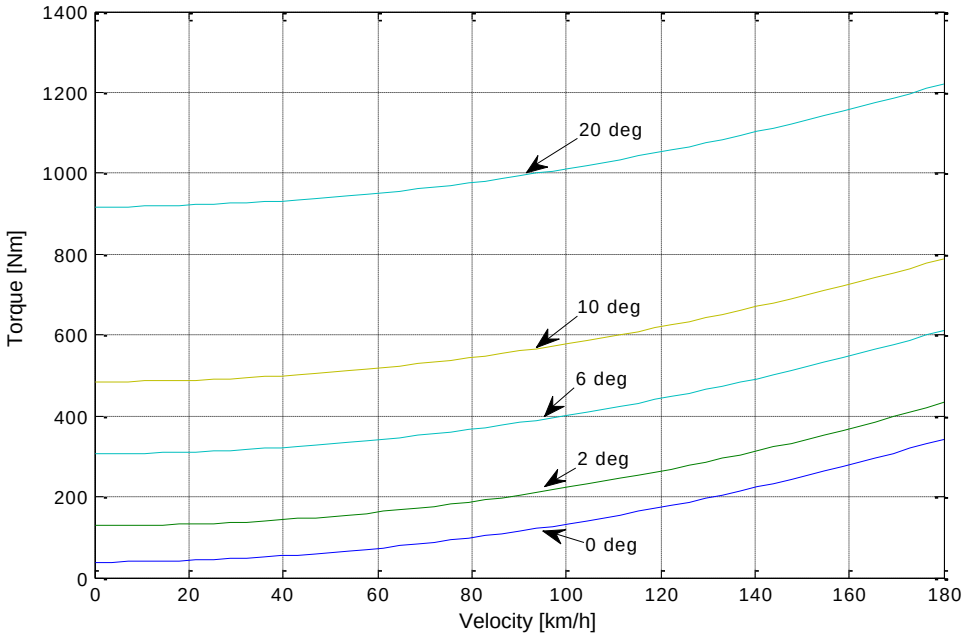

Figure 19. Plots of torque against velocity for different road gradients.

The peak mechanical power of the drive can be calculated based upon its most demanding instance, which is on a 6 % gradient at 80 km/h. This is found from

$$P = \omega T = 83.23 * 367.3 = 30.6\,kW\,. \tag{2.7}$$

Considering two hub drives to deliver this power, each would have to be rated at 15.3 kW, 1192 r/min.

To calculate the vehicle acceleration, equation (2.3) and the previously calculated values are used. Plotting *v* as a function of *t*, the graph in Figure 20 is obtained. From the graph of Figure 20, it is shown that it takes 26.3 seconds to accelerate the vehicle from 0-100km/h. The acceleration is only valid assuming operation in the constant torque region. Based on the following case study, typical performance requirements for an average hub drive can be realised as about two 16 kW wheel motor which can fit within a 15" vehicle rim.

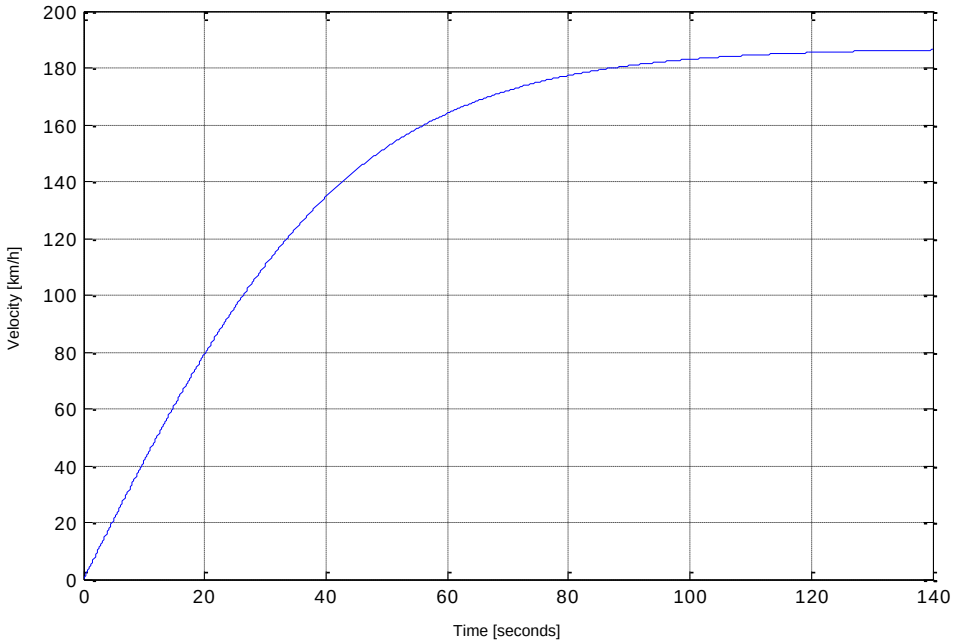

Figure 20. Acceleration of case study vehicle.

2.5 Possible Hub Motor Configurations

Several in-wheel motor configurations are proposed here along with short notes with respect to mechanical advantages and disadvantages as hub motors.

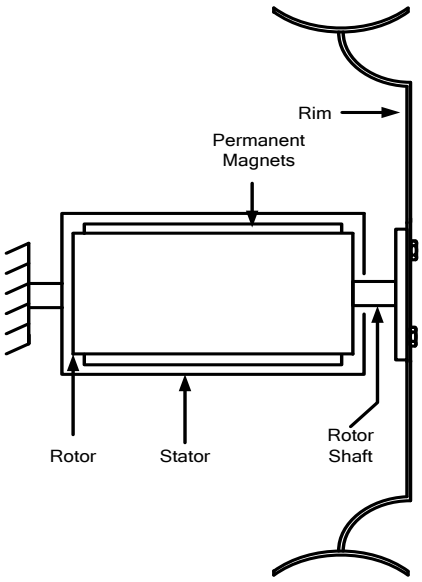

Interior Rotor Radial Flux Hub Drive

Advantages

- Simple, robust and easily sourced machine
- Power / Cooling cabling relatively easy to employ
- Easily sealed

Disadvantages

- Aspect ratio does not fit well into vehicle rim
- Could not be part of a steered wheel system due to the long axial length
- The mechanical coupling (Rotor Shaft) would provide a weak link
- Machine not protected from road hazards such as curbs and potholes

Figure 21. Interior rotor radial flux hub motor.

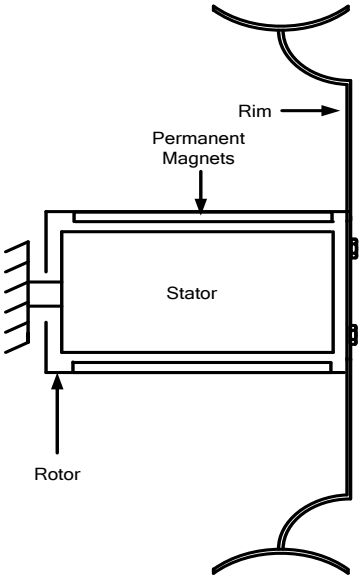

Exterior Rotor Radial Flux Machine

Advantages

- Robust and quite easily sourced machine
- Mechanical coupling much easier than interior rotor radial flux machine (No Shaft)
- Power / Cooling cabling not so easy to employ
- Easily sealed

Disadvantages

- Could not be part of a steered wheel system due to the long axial length
- Machine not fully protected from road hazards such as curbs and potholes
- Like interior rotor machine, aspect ratio does not fit well in vehicle rim

Figure 22. Exterior rotor radial flux hub motor.

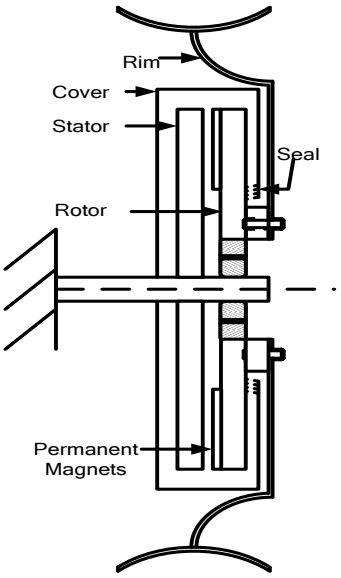

Single-Sided AFPM Machine

Advantages

- Simple machine
- Fits very well in vehicle rim
- Machine fully protected from road hazards such as curbs and potholes
- Power / Cooling cabling relatively easy to employ

Disadvantages

- Strong axial attraction forces could twist structure
- Difficult to sealing
- Single bearing reduces vehicle loading capacity
- Requires a cover

Figure 23. Single-sided axial flux hub motor.

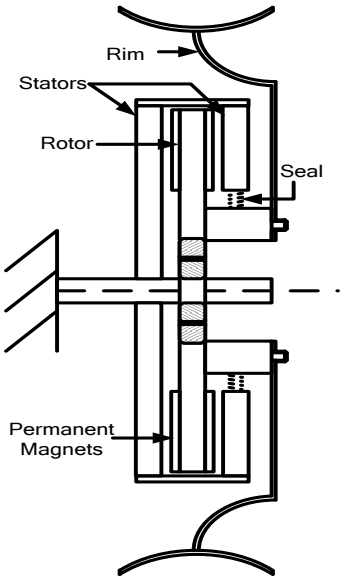

Double-Sided Interior Rotor AFPM Machine No: 1

Advantages

- Fits very well in vehicle rim
- Machine fully protected from road hazards such as curbs and potholes
- Power / Cooling cabling relatively easy to employ

Disadvantages

- Strong axial attraction forces on stator
- Second stator does not have sufficient support structures
- Single bearing reduces vehicle loading capacity
- Not easy to assemble
- Requires seal

Figure 24. Double-sided interior rotor axial flux hub motor (1).

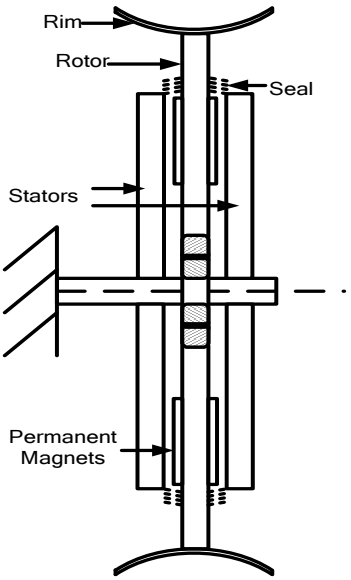

Double-Sided Interior Rotor AFPM Machine No: 2

Advantages

- Fits very well in vehicle rim
- Allow for new rim topology
- Machine fully protected from road hazards such as curbs and potholes

Disadvantages

- Strong attraction forces with insufficient structural supports
- Single bearing reduces vehicle loading capacity
- Stators supported at one end only
- Power / Cooling cabling not easy to implement
- Complicated sealing arrangement

Figure 25. Double-sided interior rotor axial flux hub motor (2).

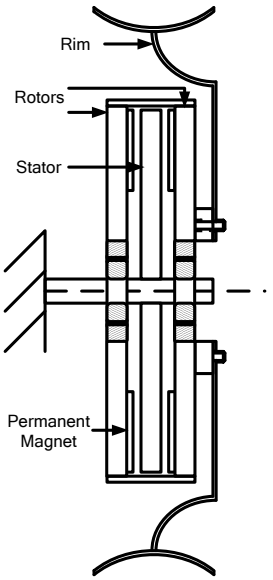

Double-Sided Interior Stator AFPM Machine No: 1

Advantages

- Fits very well in vehicle rim
- Machine fully protected from road hazards such as curbs and potholes
- Double bearing support improves vehicle loading capacity
- Rotors supported at both ends making it structurally sound
- Does not require seals

Disadvantages

- Strong attraction forces on rotor disks
- Power / Cooling cabling not easy to implement
- Stators supported at one end only
- Strong axial forces on bearings

Figure 26. Double-sided interior stator axial flux hub motor (1).

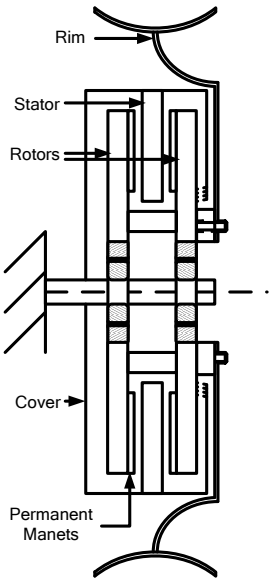

Double-Sided Interior Stator AFPM Machine No: 2

Advantages

- Fits very well in vehicle rim
- Machine fully protected from road hazards such as curbs and potholes
- Double bearing support improves vehicle loading capacity
- Attractive forces on bearings removed
- Power / Cooling cabling relatively easy to implement
- No axial forces on bearings

Disadvantages

- Stator support and cover would be challenging, and would increase size
- Stator supported at one end only
- Requires seals

Figure 27. Double-sided interior stator axial flux hub motor (2).

From the various configurations outlined, it is apparent that the AFPM machines suit the rim aspect ratio better, and are fully protected as compared to the radial machines. Of the radial machines, the exterior rotor machine is a better choice due to its robust coupling nature. From the axial flux machines, the double-sided machines are more robust due to their double-sided nature which can somewhat balance the attractive forces. From the double-sided machines, the interior stator machines are the better choice due to their double bearing configuration and better sealing characteristics. As both radial and axial flux machines seem quite excellent candidates, the practicality of constructing them needs to be assessed.

2.6 Axial Flux Machine Construction

As opposed to radial flux machines which are mass produced and quite easily manufactured, axial flux machines have several manufacturing challenges discussed as follows.

2.6.1 Rotor Yoke

Most brushless PM machine requires an iron back yoke. In order to reduce rotor iron losses, laminated steels are normally used. Unlike radial flux machines where thin laminations are punched / laser cut and then stacked, axial flux machines require iron laminations orientated

in a circular ring-like structure. This can be done by using narrow iron laminated tape wound into a toroidal / spiral ring as shown in Figure 28. The problem with iron tape is mechanical strength. Most AFPM machines have large axial attractive forces and narrow tape does not have enough mechanical strength to prevent bending. To overcome this additional backing supports can be used, but these increase the machine size.

Solid mild steel disks can be used for the rotor yoke. These are very strong and cheap, but are suitable only in applications with low rotor losses. The use of solid iron disk rotors is predominant in coreless machines.

Soft magnetic powder composites (SMC) can also be used for iron yoke manufacture, these simplify the overall machine manufacturing, but the mechanical strength is less than solid steel and the tensile strength is poor [12]. The manufacturing of these composites is also very involving. For applications not requiring any rotor yoke iron, composite materials such as epoxy glass resin can be used.

The magnets of a brushless AFPM machine rotor can be either surface mounted, in-set, or of interior design as shown in Figure 29. Surface mounting of magnets is the simplest and most common type of rotor structure. It is simple to build and assemble as magnets are simply gluing to the rotor yoke. Due to the low permittivity between the magnets, leakage flux is minimal and most of the magnetic flux is driven directly into the airgap, this leads to a rectangular airgap flux density shape. The problem of surface mounting magnets is that the structure is not very robust as the magnets are subject to high centrifugal forces. The magnets are also subjected to high demagnetisation stresses [26]. The rotor can be reinforced by the addition of a non-magnetic sleeve or belt.

Figure 28. Strip wound (toroidal) laminated steel cores.

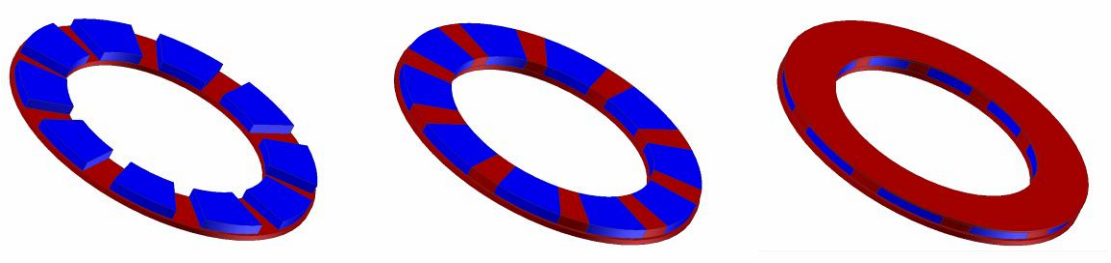

(a) (b) (c)

Figure 29. AFPM rotor configurations a) surface, b) in-set, and c) buried.

In-set permanent magnets are almost a derivative of surface mounted magnets, but with the rotor iron extending into the gaps in-between the magnets. The additional iron adds a reluctance component to the motor torque, which improves the constant power speed range, excellent for traction applications [28]. This addition is more complex to manufacture but it is structurally very strong. The problem of in-set magnets is increased leakage flux between the permanent magnets caused by the additional iron, which leads to lower flux densities [29].

A buried arrangement is the most complex to manufacture and design, but has significant advantages. The magnet arrangement is more robust, which allows for very high speed operation. There is a high flexibility in the magnet arrangement such as 'V-shaped' magnets, which can provide near sinusoidal flux density waveforms by flux shaping [29]. Buried arrangements also have low cogging torque and the lowest risk of magnet demagnetisation. Buried magnets also provide the highest reluctance component due to their salient nature. The problems of this arrangement are high manufacture cost and a high leakage flux provided by the surrounding rotor iron, but this can be reduced by the addition of flux barriers [29].

2.6.2 Stator Yoke

Slotless and coreless machine windings are stressed by electromagnetic forces and mechanical vibrations. They have large airgaps which requires more PM material and have low inductances leading to limited flux weakening operation, making them unsuitable for hub drives [22]. Slotted machine windings are more suited for hub drive applications. Two main slot types exist; the semi-closed slot and the open slot as shown in Figure 30. Semi-closed slots have advantages of higher airgap flux density, minimal winding eddy current losses, reduced cogging torque, higher inductance, and superior mechanical, thermal and electro-magnetic shielding [12] [30]. The problem with semi-closed slots is the difficulty with insertion of the winding during assembly. Either special winding machines have to be used or it is very labour intensive.

Fully open slots on the other hand have primarily the main advantage of ease of manufacture [31] [32]. Additionally there are reported cases of reduced torque ripple when using open slots in certain pole-slot combinations [33] [34]. With the fully open slots, the winding is simply slipped over the stator teeth; particularly simple when preformed coils are used. Although the advantages of semi-closed slots apparently outweigh those of fully open slots, there are applications where manufacture is of primary concern.

There is a technique to simplify insertion of windings into semi-closed of slots radial flux machines; by constructing the machine teeth separate from the stator back yoke as shown in Figure 30 (c). By this method the teeth are place over the winding and together slid into the yoke. In Axial flux topologies, the implementation of the technique would be very challenging as axial flux machines do not have teeth of a constant cross section, but have teeth that taper along their length. The technique also introduces minute airgaps and small deviation of the teeth from their exact position can occur.

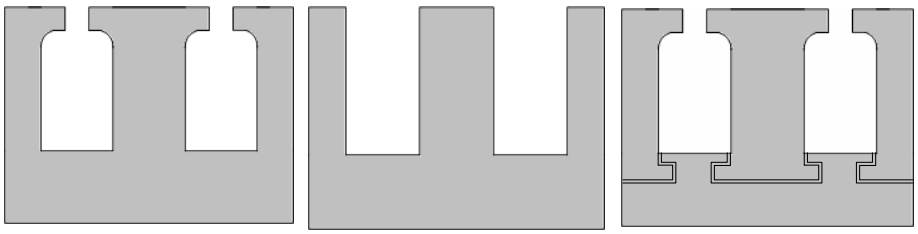

(a) (b) (c)

Figure 30. Slot types: a) semi-closed, b) open slot and c) separate.

Brushless PM machines require laminated iron stators as stator iron losses are quite high. The manufacture of laminated slotted iron stators presents the greatest problem; several construction methods are presented here.

a) Milling of Toroidal Core

Milling of slots into a toroidal core is shown in Figure 31. The problem with this approach is the possibility of short circuiting laminations and causing increased core losses. During milling, the toroidal core must be adequately supported to avoid deforming. This method is quite expensive as it requires intensive machining.

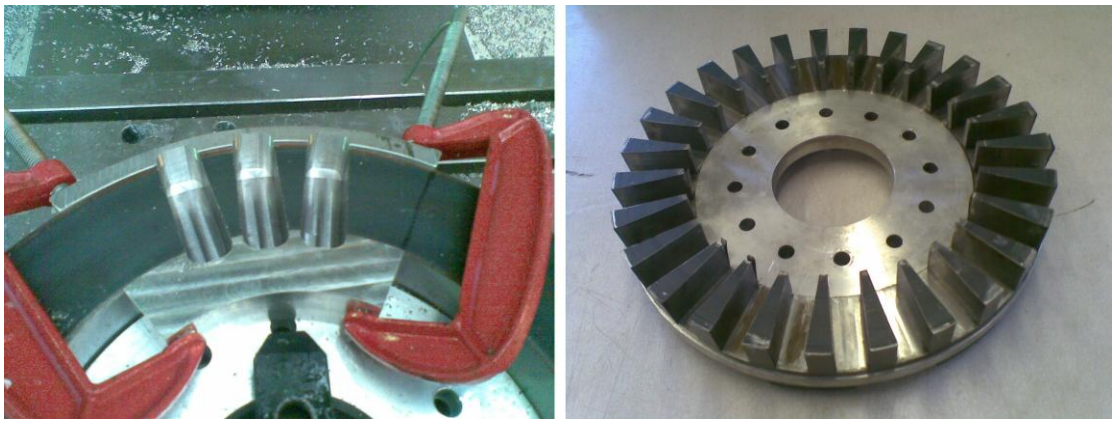

(a) (b)

Figure 31. Milling of toroidal core, a) slots being milled and b) finished stator on aluminium backing.

b) Incremental Punching

Incremental punching is done by punching slots into laminated iron tape before it is wound into a toroid as shown in Figure 32. The punched slots must be spaced incrementally so that the slots line up correctly as it is wound. This method provides high quality stators, but it requires specialised machinery [6] [12].

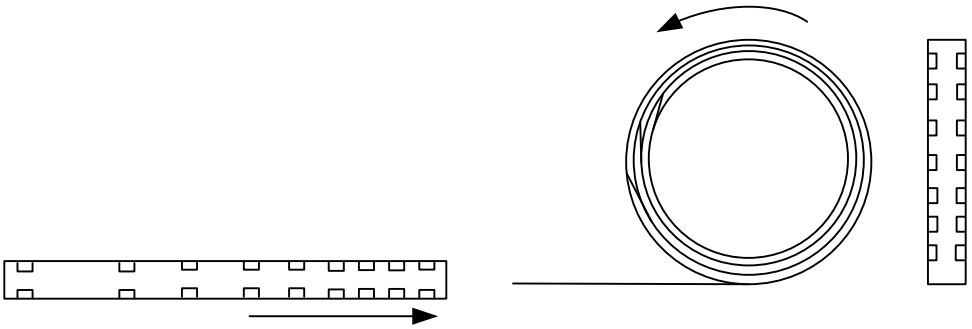

Figure 32. Incremental punching of slots into strip iron before rolling.

c) Rectangular Segmentation

This could be done by building the stator using rectangular interlocking segments with slots as shown in Figure 33. The segments are fixed together and stacked to complete the stator. This method would require very precise assembly any gaps between the segments would obstruct the electromagnetic circuit.

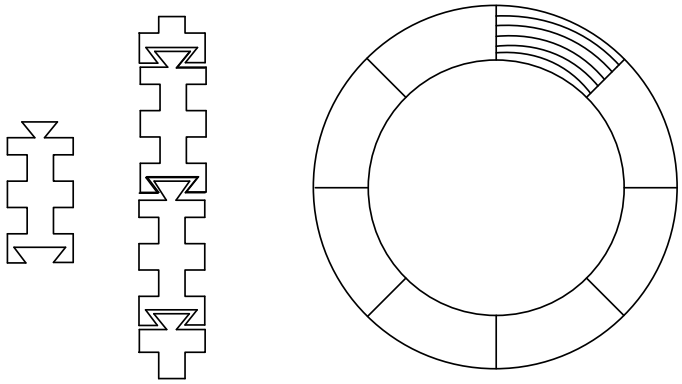

(a) (b)

Figure 33. Segmented building up of stator: a) interlocking segments, b) assembled stator.

d) Folded Segmentation

The stator could be formed from trapezoidal segments, each corresponding to a pole pitch [12]. This could be done by grooving a rectangular iron strip at several lengths corresponding to the radius and folding it as in Figure 34. The segments are compressed and assembled into a final stator as in Figure 35. The problem with this approach is ensuring that the compression of each segment is done completely with the required curvature to attain the final fit. Gaps in assembly would affect the electromagnetic circuit.

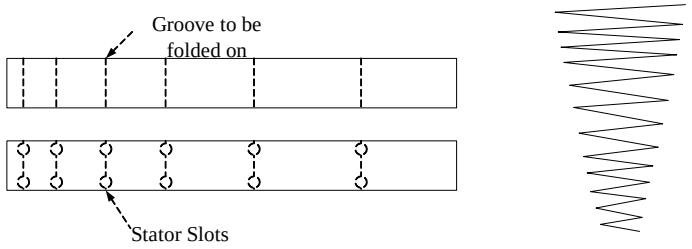

(a) (b)

Figure 34. Iron strip, a) with grooves and slots and b) folding on grooves.

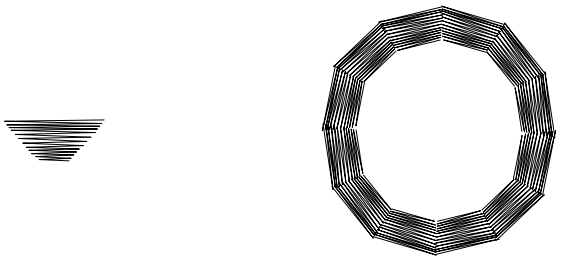

(a) (b)

Figure 35. Folded segmentation a) compressed segment and b) assembled stator.

2.7 Cooling

PM machine rotors are normally cooled by natural air convection. Heat in the rotor comes about due to losses that materialise due to stator magneto motive force (MMF) harmonics caused by slotting effects. It is important to select a suitable magnet grade to cope with the expected temperatures. Typical maximum magnet ratings range from 80 °C for entry level magnets up to 240 °C for AH grade magnets, dependant on operating conditions [35]. Forced air cooling and cooling fins can further aid in rotor cooling.

In the stator heat is generated from iron and copper losses. Suitable laminated iron must be used to limit the core losses and the current density level in the copper windings must be set according to the cooling available. In-wheel hub drives are normally designed to provide high power density levels, leading to high current densities (J >10 A/mm^2) requiring forced water cooling [10]. Upon thermal considerations, it can be assumed that based upon the machine size, 1200 W of copper loss can be adequately cooled.

2.8 Proposed Machines

After outlining the various machine topologies of Chapter 1 and the mechanical aspects herein, several machine types shown in Figure 36 stand out as good candidates for direct hub drive traction applications. From the proposed machines, the outer rotor radial flux machine is not selected as much work has already been done on it, unlike the axial flux machines. Of the axial flux machines, the single-sided is selected for evaluation in this thesis mainly due to its particular simple and compact nature. Further open slots, in-set magnets, and a sinusoidal drive are selected.

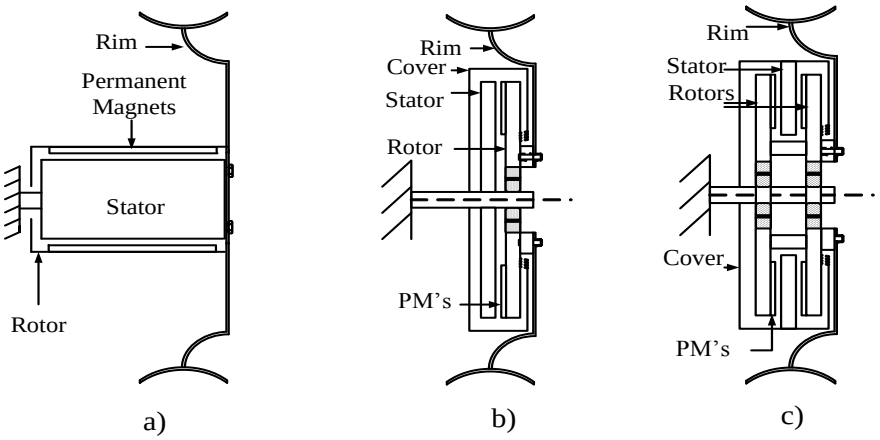

Figure 36. Selected machines a) exterior rotor RFPM, b) single-sided AFPM, and c) double-sided AFPM.

2.9 Conclusion

From the proposed machines above, the single-sided is selected for further evaluation. Table 1 gives the basic selected design criteria.

Table 1. Mechanical Design Inputs

Power	16 kW
Torque	± 340 Nm
Base/Max Speed	450 / 1350 r/min
Outer Diameter	330 mm
Outer Width	< 70 mm
Air Gap	1.6 mm
Current Density	< 11.5 A/mm^2
Operating Temp	80 °C
Stator Type	Laminated Iron
Rotor Type	Solid Mild Steel
Mass	< 25 kg
Cooling	Forced Water
Copper Losses	1200 W
Rotor	In-Set
Slot Type	Open
Drive	Sinusoidal
Phases	3

3. Brushless AFPM Machine Theory

The different types and integrations of PM machines have been highlighted in Chapter 1 and in Chapter 2, leading to selection of the single-sided AFPM topology. In this chapter the theory and control of brushless PM machines is covered. The mathematical PM machine models are set up in the *d-q* reference frame, followed by the control techniques. Particular interest is given to non-overlap windings and their winding factors, followed by PM machine losses and efficiency. Closing, torque quality is explained and un-equal tooth machines are introduced.

3.1 *d-q* Modelling

The phase voltage of any three-phase electrical machine can be represented in the conventional *a-b-c* reference frame as

$$v_{ABC} = R_s i_{ABC} + \frac{d\lambda_{ABC}}{dt}, \tag{3.1}$$

where v_{ABC} is the instantaneous phase voltage, R_s the phase resistance, i_{ABC} the instantaneous phase current and $d\lambda_{ABC}/dt$ the per phase flux linkage derivative. When working with electrical machines which contain inductances which vary with rotor speed, time varying differential equations are needed to describe the machine behaviour, except for stalled rotor cases. By doing a transformation to refer machine variables to a reference frame fixed to the rotor, rotating with it at an arbitrary angular velocity, the complexity of the differential equations can be reduced and most importantly the implementation of control strategies becomes possible [36].

In order to achieve the transformation, the Park or Clark transformations are used [36]. They are in effect a change of variable such as voltages, currents and flux linkages associated with the stator winding to a fictitious winding rotating at any angular arbitrary velocity with the rotor. The transformations are done by a mathematical matrix operation which involves employing the products and sums of variables with trigonometric functions of rotor position. More detailed information on the transforms can be found in [36]. By taking the park transformation of the mathematical model (3.1), the following equations are obtained [12]

$$v_q = R_s i_q + \frac{d}{dt}\lambda_q + \omega\lambda_d, \tag{3.2}$$

$$v_d = R_s i_d + \frac{d}{dt}\lambda_d - \omega\lambda_q. \tag{3.3}$$

In the equations v_d and v_q are the *d-q* axis components of the terminal voltage, i_d and i_q the *d-q* components of the armature currents, and λ_d and λ_q the *d-q* flux linkage components. The flux linkages are further defined as

$$\lambda_q = L_q i_q , \tag{3.4}$$

$$\lambda_d = L_d i_d + \lambda_m . \tag{3.5}$$

L_d and L_q are *d-q* the synchronous inductances and λ_m the excitation linkage flux of the PMs. By replacing the flux linkages, the *d-q* axis voltage equations can be further written as

$$v_q = R_s i_q + \frac{di_q}{dt} L_q + \omega L_d i_d + \omega \lambda_m , \tag{3.6}$$

$$v_d = R_s i_d + \frac{di_d}{dt} L_d - \omega L_q i_q . \tag{3.7}$$

On the basis of the two voltage equations above, the *d-q* equivalent circuits of a sinusoidal AFPM machine can be developed, shown in Figure 37. Figure 38 shows the *d-q* phasor diagrams for motoring operation of a PM machine. The current angle Ψ is measured from the q-axis positively into the anti-clockwise direction. With additional derivation from [12] the general torque in the *d-q* reference frame for a PM machine with *p* pole pairs can be expressed as

$$T = \frac{3}{2} p(\lambda_d i_q - \lambda_q i_d) . \tag{3.8}$$

Further by substituting the flux linkages once more the torque equation can be written as

$$T = \frac{3}{2} p\left[\lambda_m + (L_d - L_q) i_d \right] i_q , \tag{3.9}$$

where (L_d - L_q) is the reluctance torque component. For surface mounted machines it can be assumed $L_d = L_q$, hence the torque directly proportional to I_q. In machines with in-set magnets, $L_d < L_q$, negative i_d is required in order to generate positive reluctance torque. With the *d-q* machine models setup, the relevance of the *d-q* transformations is realised in the next section.

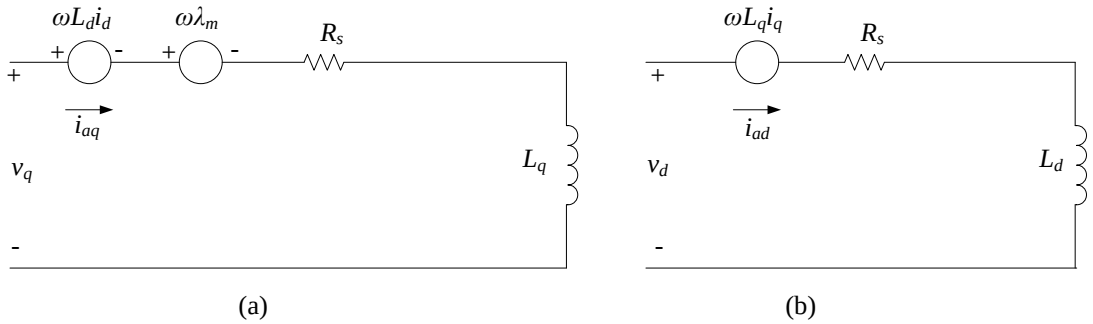

Figure 37. *d* and *q* equivalent circuits of sinusoidal brushless PM machine.

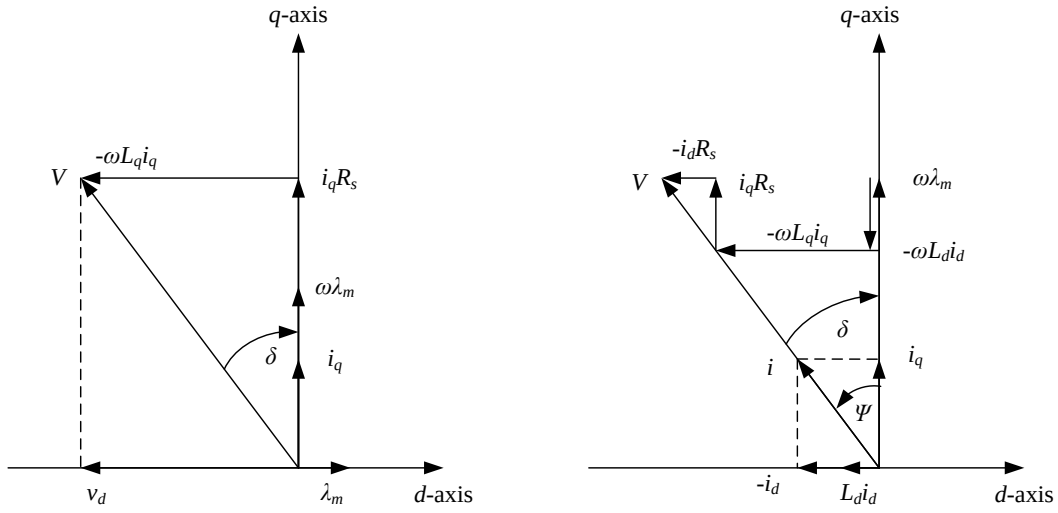

Figure 38. Phasor diagrams for motoring operation of over excited PM machine, a) with pure i_q and b) at unity power factor.

3.2 Current / Torque Control

With the basic *d-q* machine models defined, it is clear that machine control can be implemented by controlling the stator currents. The *d*-axis current essentially controls the field, while the *q*-axis current controls the torque. The problem of directly controlling the currents is the cross-coupling effect in the voltage equations. In (3.6) the *d*-axis current affect the *q*-axis voltage, with a similar phenomena in (3.7). In order to counter the cross coupling effects, a control system can be implemented.

The typical control system of a PM machine uses field orientated control (FOC) to perform all actions in the *d-q* reference frame fixed to the rotor. FOC allows for independent control of the motor flux and torque, thus allowing AC machines to be controlled in a manner similar to DC machines. In FOC the variables from the three-phase *a-b-c* system are transformed to the *d-q* reference frame where the control actions take place and then re-transformed back to the *a-b-c* reference frame with an arbitrary angular velocity of ω. The *d-q* current control system can be represented by the block diagram in Figure 39. In the block diagram the *d-q* current regulator act on feedback errors between desired commands and actual *d-q* machine currents. Additionally the *d-q* speed voltage terms are added / subtracted to the regulator outputs, thus decoupling and eliminating the cross coupling effects. This type of machine control is implemented into a DSP unit used in this research.

Operation with maximum torque per ampere (MTPA) is desirable for optimal efficiency [12] [37]. As long as there is sufficient voltage so that the current controllers do not saturate, typically in the sub base speed region ($\omega < \omega_b$), this is achieved with only i_q in surface mounted machines. For machines with saliency, this is achieved at an advanced current angle Ψ as shown in Figure 38.

By increasing the current angle from the MTPA point, the flux linkage decreases so that the induced voltage $\omega\lambda$ decreases as well, keeping the terminal voltage constant and allowing for constant power operation. This increases the speed, but the torque falls away as shown in Figure 40, which essentially changes the drive characteristics to closely resemble the desired traction characteristics of Figure 7. This "flux weakening" also allows for smaller and cheaper inverters to be used [10]. Additionally Figure 40 shows the torque, current, power and voltage characteristics in the constant torque and constant power speed regions.

Torque control can be further expanded upon to implement speed control. In speed control a speed regulator acts upon the errors between desired and measured speed to control the machine currents accordingly. Further information regarding speed control can be found in [10] [12] [37].

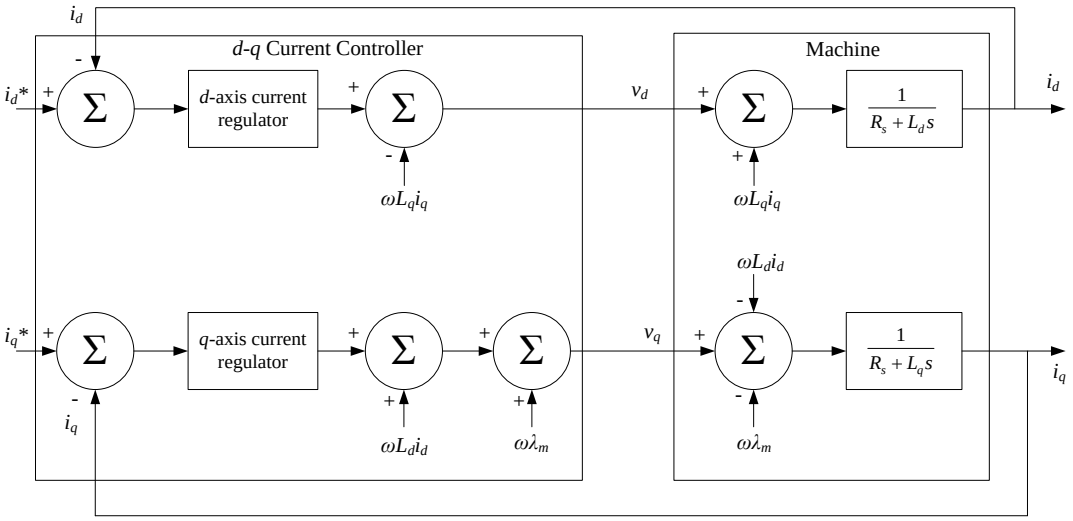

Figure 39. Block diagram of *d-q* current control system of brushless PM drive.

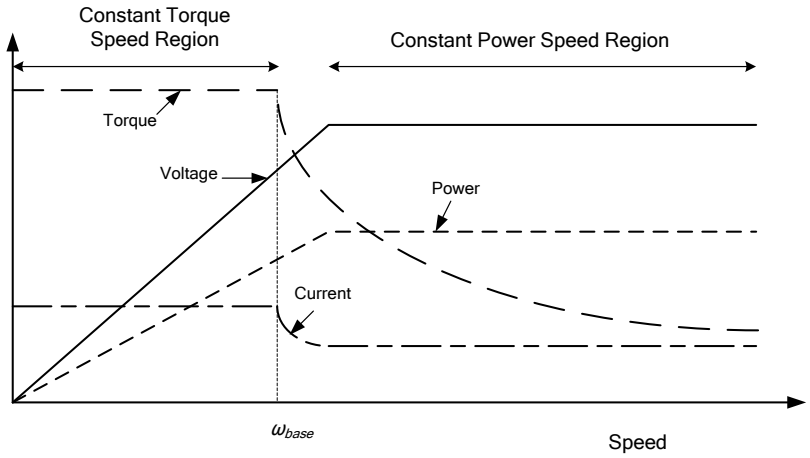

Figure 40. Torque, current, power, and voltage versus speed within the constant torque and constant power speed regions.

3.3 Single and Double-Layer Non-Overlap Windings

Non-overlap windings can be classified into single or double-layer, concentrated or distributed, integral or fractional, and air cored or iron cored groupings defined and highlighted in [38]. Single-layer windings have coils on every alternate tooth and double-layer windings have coils on every tooth as shown in Figure 41. Much work has been done in comparison of single-layer and double-layer windings with particular interest to winding factors, fault tolerance and harmonics [15] [39] [40] [41] [42]. These works show that single-layer windings prove superior with regard to self inductances, winding factors and fill factors over their double-layer counterparts. Several single-layer variants (such as the 10 pole 12 slot machine) posses zero mutual inductance attributes, which lead to a very high degree of fault tolerance [39]. Single-layer machines also tend to also have higher torque capability over their double-layer counterparts.

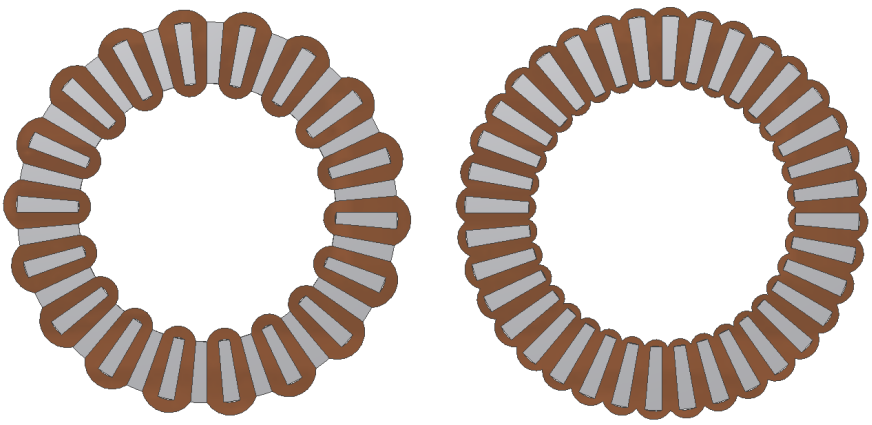

(a) (b)

Figure 41. Non-overlap windings of axial flux machine, a) single-layer and b) double-layer.

On the down side single-layer configurations tend to contain higher harmonics in their MMF distribution. These higher harmonic contents, particularly the sub-harmonics lead to inferior torque quality and higher rotor losses [39] [42]. Although single-layer machine with their high inductances appear as good candidates for flux weakening applications [43] states that they are not the best practical solution and that double-layer machines with increased inductance due to buried magnets or magnetic slot wedges are better suited. Such double-layer machines with reluctance torque are better suited for achieving higher efficiency since their armature reaction flux is lower and that they have lower rotor eddy current losses. Furthermore, single-layer machines have a larger end windings size which increases their size. The end winding surface area of a non-overlap axial flux winding can be calculated from [31]

$$A = \frac{1}{2}\pi\left[\left(\alpha + h/2\right)^2 - \left(h/2\right)^2\right], \tag{3.10}$$

where α is the slot width and h the tooth width at the machine outer diameter as shown in Figure 42. In double-layer machines the slot width becomes half that of the single-layer with α replaced by $\alpha/2$.

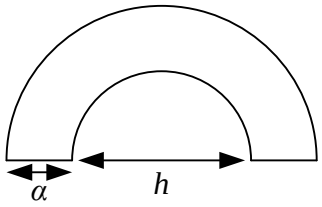

Figure 42. Non-overlap winding outer end winding.

The average end windings length of each coil is calculated by [44]

$$L_{ce} = \frac{2\pi(R_{out} + R_{in})}{Q}, \tag{3.11}$$

where Q is the number of stator slots, R_{out} the outer and R_{in} the inner machine radii. This equation is valid for both single and double-layer windings. Assuming a similar stator is used for a single and double-layer machine, the number of turns of a single-layer coil can be assumed to be double that of the double-layer coil.

3.4 Pole-Slot Combinations and Winding Factors

Non-overlap PM Machines provide an abundant range of possible pole-slot combinations. The greatest common denominator (GCD) between the machine poles $2p$ and slots Q combination [38] [45]

$$GCD(2p, Q), \tag{3.12}$$

gives information to the symmetry of the machine, vibration modes, balancing forces. The symmetry becomes particularly useful when modelling the machine. Subsequently the least common multiple (LCM) between the poles and slots

$$LCM(2p, Q), \tag{3.13}$$

provides indication to the cogging periods per cycle; in general the higher the cogging cycles the lower the magnitude [46]. Generally a high LCM and GCD are desirable, but values often contradict, such as those with high LCMs having low GCDs etc. The fundamental winding factor of a non-overlap PM machine (k_{w1}) is given by the product of the distribution factor and the pitch factor by [38]

$$k_{w1} = k_{d1} k_{p1}, \tag{3.14}$$

where the distribution factor is given by

$$k_{d1} = \frac{\sin(\pi / 2m)}{u \sin(\pi / 2mu)}, \tag{3.15}$$

where m is the number of phases and u the number of coils in a phase group. Additionally the pitch factor is given by

$$k_{p1} = \sin\left(\frac{\pi}{2}\frac{2p}{Q}\right). \tag{3.16}$$

The winding factor gives an indication to the utilisation of the winding and a high value is normally sought, but a high value does not always guarantee high torque capability [30].

Appropriate selection of the pole-slot combination is very important. For low speed high torque requirements as needed for in-wheel hub drives, the basic rule of thumb is to have a high pole number [10]. If a low number of poles is selected, it would lead to large PMs which would increase the machine axial size due to a thicker yoke requirement and this would also increase the end winding size; causing higher leakage inductance and copper losses. However having a high pole number can be limited by the available space and manufacturability; as small magnets and windings are difficult to work with and can involve a higher cost. Additionally, if the number of poles selected is too high, the frequency would be high increasing core losses. A high pole number would also cause restriction on the control response frequency of the PWM inverter and resolution of the position resolver [27]. On the basis of the previously outlined theory and in [38] [45], when selecting pole-slot combinations it is best to aim for a high winding factor, high LCM and high GCD. Based upon this several potential pole-slot combinations of non-overlap machines are identified and given in Table 2. It can be seen not one combination has the best of all aspects, making pole-slot selection ambiguous and more so a design preference.

Table 2. Pole-Slot Combinations

2p	*Q*	k_{w1}	*LCM*	*GCD*	Winding
30	27	0.945	270	3	DL
30	36	0.966	180	6	SL
30	36	0.933	180	6	DL
40	30	0.866	120	10	DL

3.5 Voltage Calculation

The winding factor described previously plays a vital role in determination the machine voltages. Using the winding factor the EMF induced in an AC winding can be calculated by [12] [39]

$$E = 4.44 f k_{w1} N_s \phi , \tag{3.17}$$

where N_s is the number of turns in series per phase, f the excitation frequency and ϕ the flux per pole given by

$$\phi = B_{avg} \frac{\pi}{2p} (R_{out}^2 - R_{in}^2), \tag{3.18}$$

where B_{avg} is the average airgap flux density. This voltage calculation is used to verified by FE and measured results presented later in chapter 5.

3.6 Losses and Efficiency

Brushless PM machines have loss components in their stator and rotor. The stator losses are attributed to copper resistive losses, copper eddy current losses and iron yoke losses. In the rotor circuit there are magnet losses and rotor yoke losses. Additionally there are also mechanical rotational losses.

3.6.1 Stator Winding Losses

The total per phase stator resistance is calculated by

$$R_s = \rho \frac{L}{A_{con}} \frac{N_s}{N_p}, \tag{3.19}$$

where ρ is the resistivity of copper taken as 17 x 10^{-9} Ω·m at 20 °C, A_{con} the copper area of a single conductor, N_p number of parallel circuits and L the total conductor length given by

$$L = 2w + L_{ce}, \tag{3.20}$$

where w is the stack length. The resistive copper losses P_{cu} in the stator winding are given by

$$P_{cu} = 3 I_a^2 R_s . \tag{3.21}$$

The presence of the machine currents causes a current density J in the conductors given by

$$J = \frac{i_{a_{peak}}}{\sqrt{2}A_{con}}. \tag{3.22}$$

As slots are filled with copper windings, a fill factor k_f is used to indicate the amount of copper present. The copper fill factor is given by

$$k_f = \frac{A_{con}}{A_{slot}} N_{slot}, \tag{3.23}$$

where A_{slot} is the available slot area and N_{slot} the number of conductors per slot. Typical fill factors for non-overlap iron core machines range between 0.3 - 0.5.

3.6.2 Stator Winding Eddy Current Losses

For semi-closed slot PM machines, the eddy current losses in the stator winding P_e are insignificant as very little leakage flux penetrates the conductor slot space. In coreless, slotless and open slot machines the stator windings are exposed to the rotating airgap magnetic flux leading to induced eddy current losses in the conductors. Computational methods for eddy current losses are presented in [12].

3.6.3 Stator Core Losses

The stator core losses P_{core} due to the main flux and fundamental supply frequency can be given by [47] ,

$$P_{core} = cf_1^{\,x}(B_{mt}^{y}M_t + B_{my}^{y}M_y), \tag{3.24}$$

where c, x and y are coefficients from steel manufacturers loss-frequency curves, B_{my} and B_{mt} the flux densities in the yoke and teeth, f_1 the fundamental supply frequency and M_t and M_y the teeth and yoke iron mass respectively. This equation is implemented in the finite element program used.

3.6.4 Permanent Magnet Losses

Unlike conventional overlapping winding PM machines in which PM losses P_{PM} are negligible, non-overlap PM machines have a stator MMF distribution containing a rich set of space harmonics and a pulsating flux component in slotted machines caused by airgap reluctance variations. These phenomena result in lower and higher order space harmonic MMFs with rotational speeds asynchronous to the rotor, which induce eddy current losses in

the magnets. Care must to be taken to predict eddy current losses as they can cause overheating of the magnets.

Works in [12] [48] [49] [50] present analytical methods of determining eddy current losses in magnets and show that the eddy current losses can be reduced by using segmented magnets. This segmentation of magnets is analogous to using laminated steels to reduce iron losses in rotor and stator yokes. Additionally in [49] machines with open slots were found to increase magnet losses. In the scope of this thesis magnet losses were not particularly dealt with.

3.6.5 Rotor Core Losses

The MMF harmonics and slotting effects described previously also lead to iron losses P_{rot} in the rotor iron yoke. Rotor losses in slotted machines are primarily comprised of eddy current losses. Hysteresis losses are present in the rotor circuit, but the pulsations are not flux reversing as like in the stator and only minor B-H loops are setup, yielding small hysteresis losses. Analytical and computational methods are presented in [12] [51], and show significant loss reduction by using laminated irons over solid iron. In coreless PM machines rotor losses are negligible as the rotor flux distribution is fixed and can be termed as almost DC.

3.6.6 Mechanical Losses

The mechanical losses P_{mech} in PM machines arises from bearing losses due to friction and windage losses due to aerodynamics of the rotating rotor. Windage losses are normally assumed upon the machine size, and bearing losses calculations are highlighted in Appendix A.

3.6.7 Efficiency

The total losses in a PM machine ΔP_{tot} are therefore

$$\Delta P_{tot} = \Delta P_{cop} + \Delta P_e + \Delta P_{core} + \Delta P_{PM} + \Delta P_{rot} + \Delta P_{mech}\,, \tag{3.25}$$

and the efficiency η is

$$\eta = \frac{P_{out}}{P_{out} + \Delta P_{tot}}\,. \tag{3.26}$$

The losses and efficiency explained can also be obtained by finite element modelling; these results are presented in Chapter 5.

3.7 Cogging and Torque Ripple

Cogging torque in PM machines occurs from the interaction between the airgap permeance variations due to the stator slotting and the PM MMF harmonics as the machine rotates unexcited. Further when the machine is excited, the cogging effects along with MMF harmonics from the stator winding, current harmonics from inverters and saturation in the magnetic circuit of the machine manifest as torque ripple [33][43][52]. The only methods of obtaining design results of these torques is by finite element analysis. Chapter 4 explains how the torques are obtained and investigates torque quality extensively.

It is desirable to minimise cogging and torque ripple in PM machines, their reduction leads to reduced vibration and longer machine life with smooth and quiet operation. In order to reduce these parasitic effects several approaches are available; either control based [53] or machine design based as focused on herein. Some of the major machine design techniques used are [12] [33] [43] [52] - [56]:

- Pole-slot combination selection with high LCM
- Relative magnet width
- Skewing of stator or rotor
- Slot Opening width
- Magnetic wedges across stator teeth
- Pole shaping

There are additional methods available in [54] [56] [57], but some most of the methods are impractical, not applicable to axial flux machines and are not justified by their complexity and additional cost. Applicable only to single-layer machines is one other unique design technique to minimise torque pulsations; the use of un-equal teeth.

3.8 Single-Layer Machines with Un-Equal Teeth

To further enhance the torque performance of the single-layer PM machines, novel topologies with un-equal teeth have been introduced in [58]. By employing un-equal teeth, the slots become irregularly distributed and the winding factor becomes adjustable, allowing for enhancement of the main winding factor, an aspect not possible with double-layer structures. The typical method is to increase the width of the teeth holding a single-layer coil, and decreasing the width of the remaining teeth as shown in Figure 43. By this adaptation, the

coils can link higher magnetic flux and better magnetic exploitation is achieved [59]. A new machine dimension is defined, the tooth width ratio k_{TW} given as

$$k_{TW} = \frac{inner\,tooth\,width}{outer\,tooth\,width}. \tag{3.27}$$

All the work found by the author relating to machines with un-equal teeth [32] [39] [58] - [61] practice fully maximising the fundamental winding factor or adjusting for maximum flux linkage. With unity winding factor under BLDC operation, these machines exhibit higher torque capability and reduced torque ripple compared to single and double-layer machines with equal teeth [59] [61]. Under BLAC operation, the machines still exhibit high torque capability, but their torque quality is very poor [61].

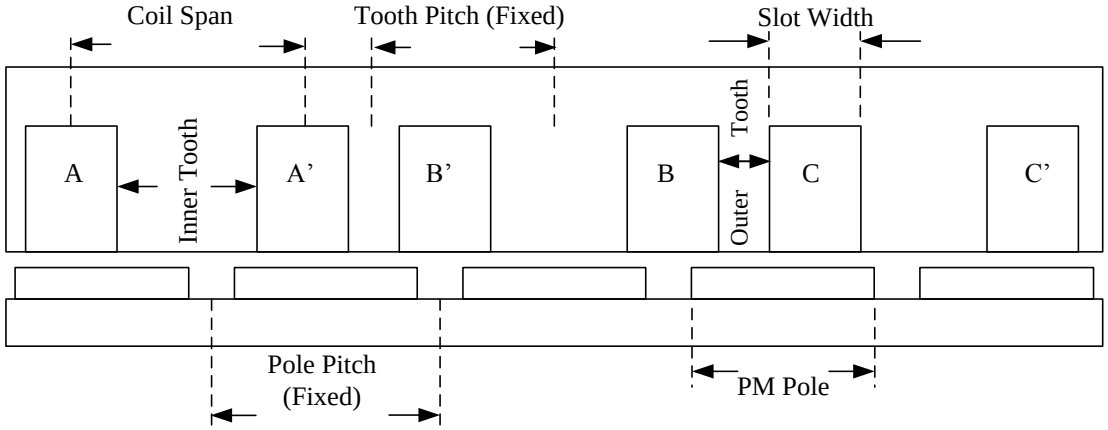

Figure 43. Linearised section of 30-pole 36-slot machine with un-equal teeth.

3.9 Conclusions

In this section the *d-q* machine models are derived and their significance for control is explained. Non-overlap windings are highlighted and several pole-slot combinations proposed. Cogging torque and torque ripple are explained with some minimisation techniques given.

4. Design and Optimisation

Having the basic design choices carried out and the *d-q* models setup, the design of a suitable AFPM machine can be carried out. In this chapter, finite element modelling (FEM) is used to model AFPM machines, based upon a linearised modelling technique. The resulting designs are fine tuned further with the aid of an optimisation algorithm. Thereafter the parasitic effects of cogging torque and torque ripple are investigated, with several techniques applied for minimisation.

4.1 Design Specifications

The basic design selections made in the preceding chapters can be summarised to form the design inputs given in Table 3.

Table 3. AFPM Machine Design Inputs

Power	16 kW
Torque	± 340 Nm
Base/Max Speed	450 / 1350 r/min
Outer Diameter	330 mm
Outer Width	< 70 mm
Air Gap	1.6 mm
Current Density	< 11.5 A/mm^2
Cooling	Water
Operating Temp	80 °C
Stator Type	Laminated Steel
Rotor Type	Solid Mild Steel
Mass	< 25 kg
PM Rotor	In-Set
Magnets	NdFeB - N40SH
Winding	SL or DL
Slot Type	Open
Pole-Slot Combination	30-27 or 30-36
Drive	Sinusoidal
DC Bus	440 V
Winding	Star
Copper Losses	1200 W

4.2 Finite Element Analysis

When designing electrical machines, analytical equations are limited as they only describe the electrical and magnetic circuits. For a more accurate performance evaluation, higher level numerical methods are required that can more accurately describe the dynamic machine performance and certain aspects that cannot be obtained under practical tests, thus a virtual approach is needed. Currently, finite element (FE) is the most commonly accepted numerical method, which can be used to solve 2D and 3D electromagnetic field problems. Further information on finite element analysis can be found in [47] and Appendix B.

By using symmetry in electrical machines, most FE solutions can be obtained by 2D modelling, which is less computer processing intensive than 3D modelling. Even though 2D modelling is a somewhat approximation of the full model, it has been proved accurate. Additional model reduction is achieved by symmetry about the pole-slot combination (GCD) which further reduces the model into a section with periodic boundary conditions.

Several finite element packages are used throughout this research. For the electromagnetic simulations, a non-commercial package is used. The package is developed in collaboration by the Universities of Cambridge and Stellenbosch. A second electromagnetic commercial package Magnet 6® is also used, primarily for verification purposes. Structural and thermal finite element simulations are also done using ANSYS® 12.0 Multiphysics.

4.3 Design Optimisation

Electrical machine design is a highly non-linear process and trying to optimise machine parameters for example by graphing / tabulation is not efficient by any means. Optimisation algorithms based on the Powell's method for example [47], provide a far superior method of searching for optimal points. Optimisation is a point orientated process with which one must clearly state the

- Design Objective,
- Design Variables and
- Fixed Constraints.

These must be defined otherwise the optimisation will be unconstrained. The objective function of the optimisation can be defined as

$$F = Y - \sum_{i=1}^{n} w_i \varepsilon_i , \tag{4.1}$$

where Y is the value to be maximised, ε_i the penalty functions, and w_i the respective weighting factors. The penalty functions are added to the objective function in order to avoid violating the limits of secondary functions (constraints) such as less than average torque T_{ave} or higher than maximum current densities J. These penalty factor are defined as

$$\varepsilon_1 = \begin{cases} (T_{\min} - T_{ave})^2 & : T_{ave} < T_{\min} \\ 0 & : T_{ave} \geq T_{\min} \end{cases}, \tag{4.2}$$

$$\varepsilon_2 = \begin{cases} (J - J_{\max})^2 & : J > J_{\max} \\ 0 & : J \leq J_{\max} \end{cases}. \tag{4.3}$$

The optimisation procedure for optimising machine design can be best explained by the use of the flow chart of Figure 44. Using the FE solution, the optimisation algorithm (Powell's method), assigns values to the machine variables, X, that maximise the performance, Y, of the machine. Note that with each iteration i, the optimisation algorithm determines directions of search in multiple dimensions along which Y is maximised. The optimisation algorithm is linked with the FE program in such a way that each time the optimisation algorithm requires the output, Y, for a given input, X, it calls the FE program. The FE program then generates a new mesh according to the changed inputs (the new meshes must be checked for violations). The program then does the pre-processing and the non-linear solution to determine the magnetic vector potentials. From this the FE program calculates the flux linkages and the torque. Due allowance is made for saturation by using the correct B-H curve of the machine steel in the FE program. The FE program can be called more than once by the algorithm. At the end of each iteration a test is carried out to determine if the maximum is reached; if not the next iteration is executed. Therefore, optimisation can be a time consuming process especially if the number of variables to be optimised are many. Re-running the optimisation with different initial values and checking if it still converged to the same optimum values must be done to verify the design optimisation. This must be done as there could be local maxima (or minima) in the optimisation process.

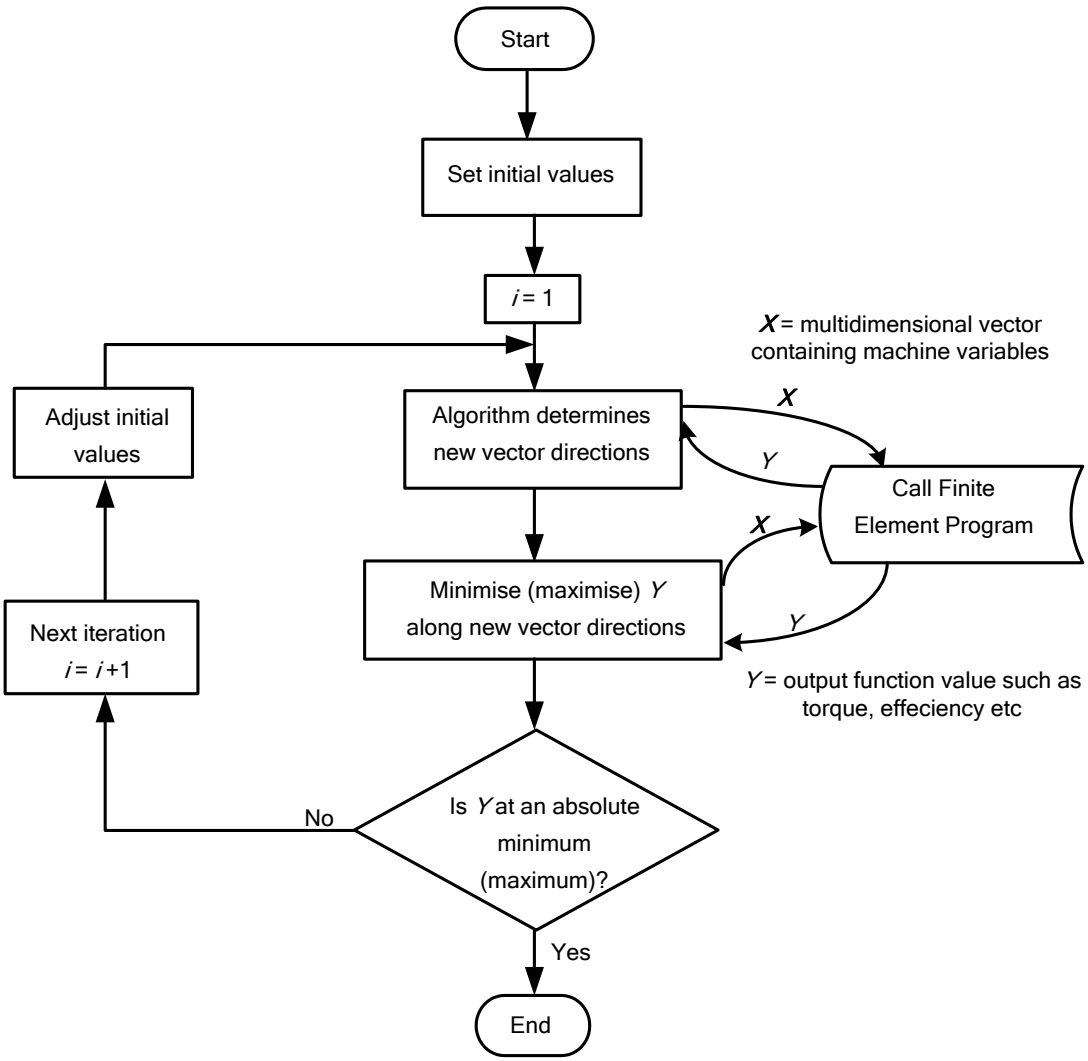

Figure 44. : Optimisation procedure using FE method [47].

4.4 AFPM Machine Linearised Modelling

The most important dimensions pertaining to AFPM machines are the inner and outer diameters D_i and D_o respectively, shown in Figure 45. The ratio of the two diameters k_d considerably affects machine performance and is given by

$$k_d = \frac{D_i}{D_o}. \tag{4.4}$$

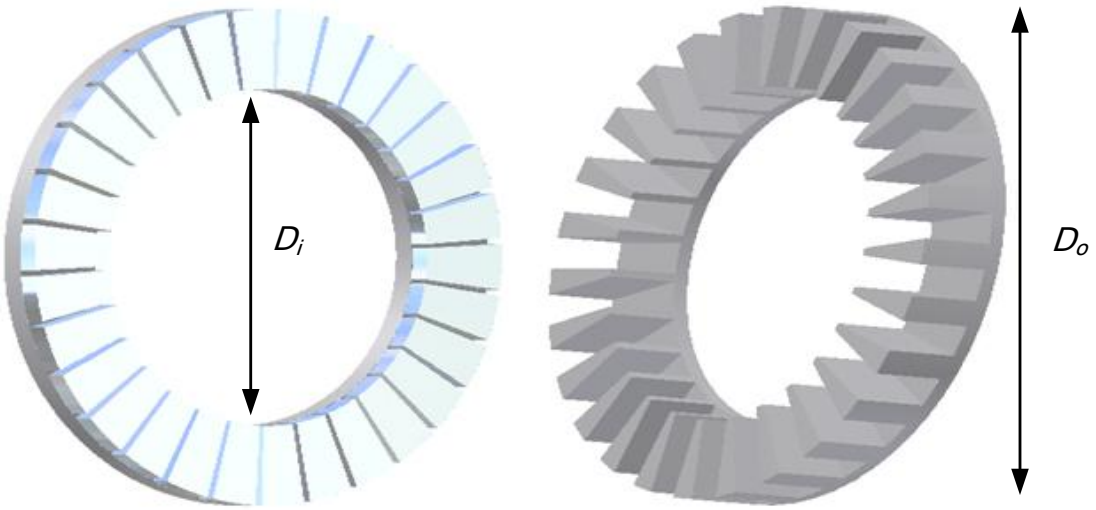

Figure 45. Axial flux machine main dimensions.

The active stack length of an axial flux machine is given by

$$L_{eff} = \frac{D_o - D_i}{2}. \tag{4.5}$$

The additional machine dimensions of axial flux machines such as the magnet and stator teeth widths are difficult to define as they vary along the machine diameter. As axial flux machines taper in towards their inner centres and unlike radial flux machines which have symmetry about their lengthwise cross section, axial flux machines present no such symmetry. The only way to model these machines is by complete 3D modelling or by linearised 2D modelling. Linearised 2D modelling is done based on a computational plane along the machine stack, usually the average radius r_{avg} between the outer and inner radii given as

$$r_{avg} = R_{in} + \frac{R_{out} - R_{in}}{2}, \tag{4.6}$$

and shown in Figure 46. The width wise dimensions of slots, teeth and magnets are all based upon the average computational plane and modelled as a linear (side view) section reduced upon the *GCD* as shown in Figure 47. Further the machine active stack length is applied as the model depth. This linearised 2D modelling technique has been proved reliable and tremendously reduces solution time of the FEM [44] [58].

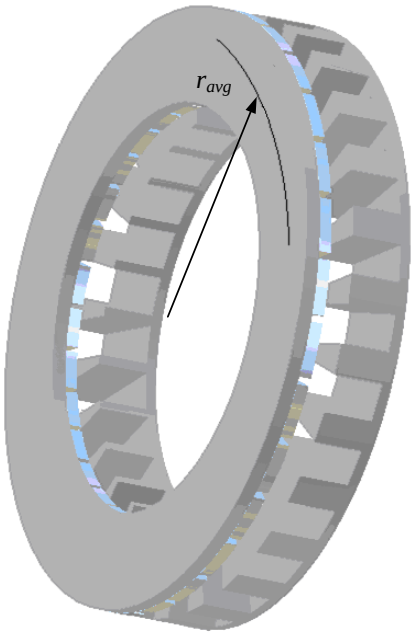

Figure 46: Axial flux machine, average radius plane.

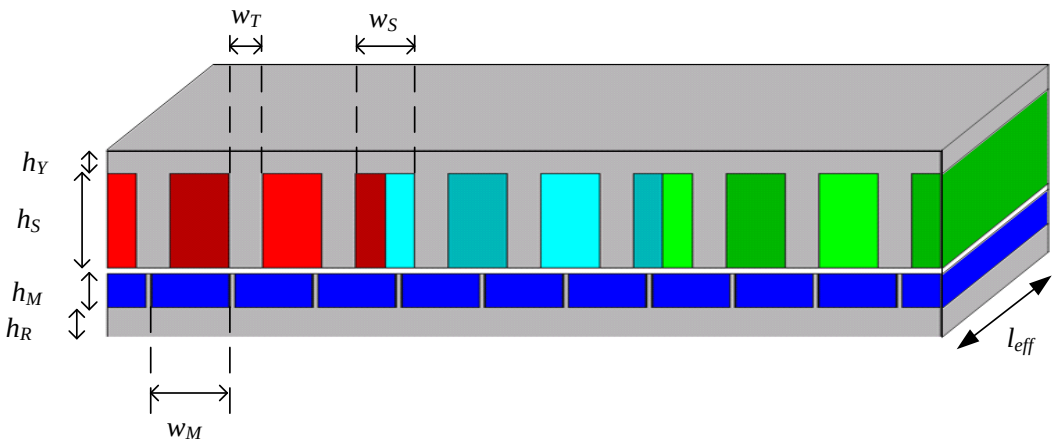

Figure 47. Linearised model of 30-pole 27-slot AFPM machine.

In Figure 47 h_Y is the stator yoke height, h_S the stator slot height, h_M the PM height, h_R the rotor yoke height, w_T the stator tooth width, w_S the slot width and w_M the magnet width. The magnet to pole pitch ratio α_i can now be defined by

$$\alpha_i = \frac{w_M}{\tau}, \tag{4.7}$$

where w_M is the magnet width at the computational plane and τ the pole pitch given by

$$\tau = \frac{2\pi r_{avg}}{2p}. \tag{4.8}$$

4.5 Multi-Slice Analysis

As the previous approach is suitable for solving most matters, issues such as instantaneous torque profiling require more precise modelling. 3D FE modelling would be ideal, but when used in conjunction with an optimisation algorithm which cycles a large number of FE computations it becomes computationally intensive and time consuming. The alternative approach, adopted in this work is multi-slice or quasi-3D modelling, first proposed in [44]. This method involves modelling upon several linear 2D computational planes, based on several radii along the machine stack, and taking the average of results. This approach is well accepted and has been proved accurate to 3D modelling [58].

For instances requiring instantaneous torque profiling, the Maxwell Stress Tensor or Virtual Work methods are used. The two methods are explained in Appendix B. The instantaneous torque T_n at a position n of a multi-slice approach can be defined as

$$T_n = \frac{\sum_{1}^{k_s} T_{ks,n}}{k_s}, \tag{4.9}$$

where k_s is the number of computational planes and $T_{ks,n}$ the instantaneous torque on plane k_s at position n.

4.6 Design and Optimisation of 30-Pole 27-Slot Machine

One of the selected topologies is the 30-pole 27-slot machine. This machine is modelled as a ⅓rd section (GCD=3) as 10 poles and 9 slots, with positive boundary condition (even pole pairs). This pole-slot combination can only support a double-layer winding as the slot number is uneven. The model materials are defined as follows in the FEM:

- Stator – M5 GOSS (input B-H curve)
- Rotor – Mild Steel (input B-H curve)
- Windings – Copper (relative permeability 1.0)
- Permanent magnets – NdFeB N35SH (relative permeability 1.067)

In order to define the PMs, thin current carrying sheets are used on the sides of the PMs. For the selected magnet grade, the coercivity H_c in the sheets is set 880 kA/m. For magnets of opposite polarity, the defining currents are reversed. The stator winding is modelled as current carrying conductors wound in and out of the z-plane. In the 30-pole 27-slot model, 9 non-overlap coils are present, with 3 series connected coils to a phase group. Figure 48 shows

the model winding layout and in Figure 49 it is shown again in the FEM. As the machine model is repeated 3 times, the phase groups of each section can be either series or parallel connected, herein the connection is parallel with the number of parallel circuits N_p = 3. Further three-phase 120° phase displaced current sources are defined accordingly based upon rotor position. The machine currents are calculated from the copper losses, by defining the currents in this manner, the copper loss are kept constant which allows for comparison of different designs. The peak value of the phase currents from the copper loss is defined as

$$i_{a_{peak}} = \frac{\sqrt{\frac{2P_{cu}}{3R_s}}}{N_p}. \tag{4.10}$$

The operating conditions of the machine also need to be defined in the FEM. The base speed is set 450 r/min and from the pole pairs the excitation frequency is 112.5 Hz. An offset of the rotor is done to correctly synchronise the magnetic *q*-axis to the stator phase *a*-axis as it peaks. The phase rotation and rotor direction are also synchronised. With the model defined, a mesh is generated as shown in Figure 50. With the mesh applied, the FE solution is run to obtain the field solution shown in Figure 51.

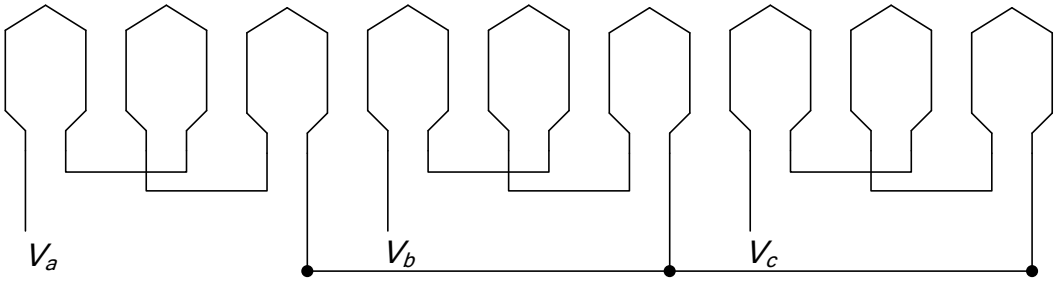

Figure 48. Winding layout of 30-pole 27-slot AFPM model.

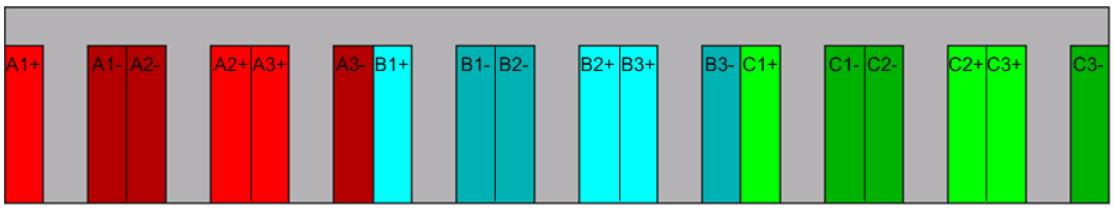

Figure 49. Winding layout of 30-pole 27-slot model.

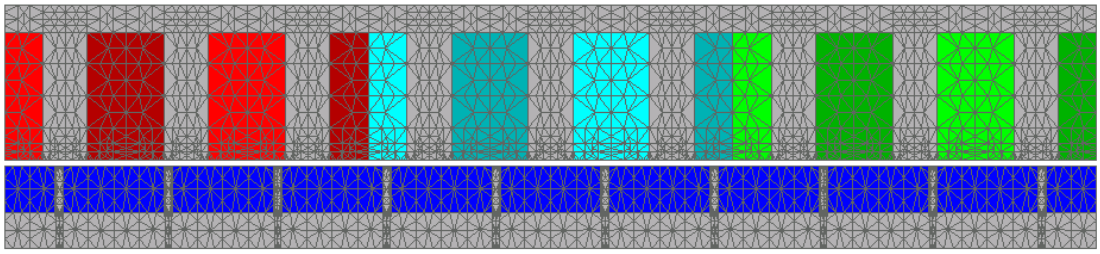

Figure 50. FE mesh of 30-pole 27-slot model.

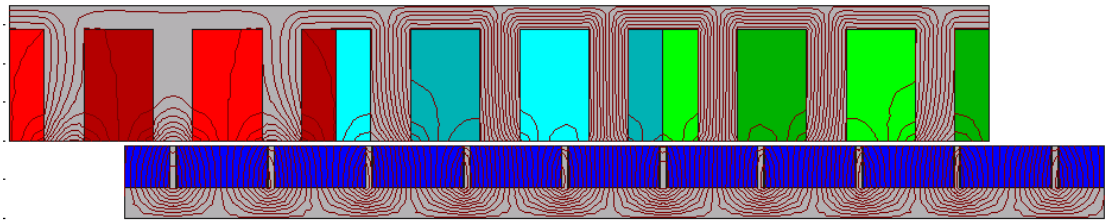

Figure 51. FE field solution of 30-pole 27-slot model.

With the FEM in place, a design optimisation is carried out with the aim to optimise seven machine parameters of the AFPM machine, highlighted in Figure 52. Two machine design objectives are pursued constrained by equal copper loss and the outer machine dimensions, namely:

PM 1 : Efficiency Optimisation (T_{avg}/*copper losses*),
and
PM 2 : Power density Optimisation (T_{avg}/ *volume*).

The results of the optimisations are given in
Table **4**.

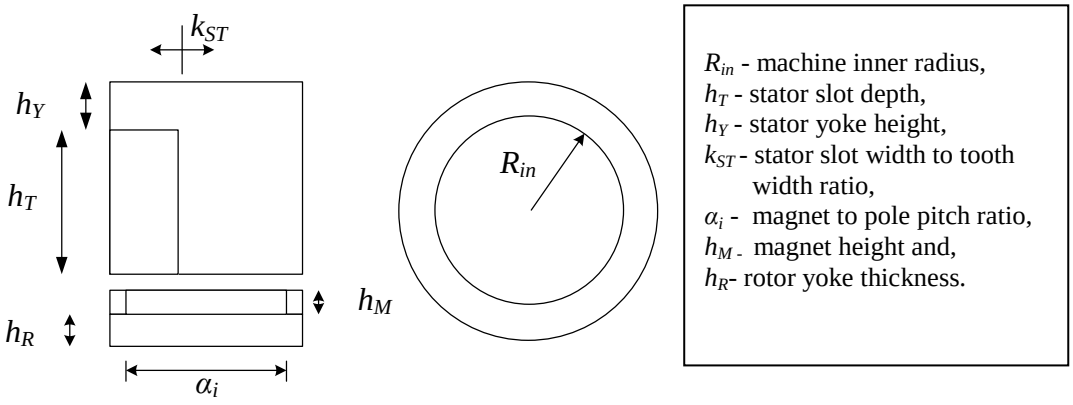

Figure 52. Machine parameters to be optimised.

Table 4. Optimisation Results of 30-Pole 27-Slot Machine

			Optimal	
Variable	Min	Max	**PM 1 (η)**	**PM 2 (P/m^3)**
R_{in} [mm]	50	140	69.31	112.51
h_T [mm]	20	40	31.51	29.0
h_Y [mm]	4	12	5.91	6.0
k_{ST}	0.3	0.8	0.5953	0.6329
α_i	0.7	0.96	0.94	0.94
h_M [mm]	4	12	9.26	10.6
h_R [mm]	4	12	6.92	8.0
Torque [Nm]			400	340
Current density [A/mm^2]			8.88	10.23
Copper Losses [W]			1200	1200
Active volume [m^3]			0.003874	0.002517
Magnet mass [kg]			4.57	3.4
Total Mass [kg]			24.35	16.9
Power density [kW/m^3]			4875.8	6427.3
Attraction forces [kN]			20	13.8
Stack length [m]			0.096	0.0525
Diameter ratio k_D			0.42	0.68

From the results the efficiency optimisation (PM1) provides the best torque performance overall, exceeding the required 340 Nm. With regard to application, the result provides several drawbacks, mainly due to the large stack length which reflects upon the size and mass of the machine. In-wheel hub drives need to take up a small size within the vehicle rim so as to provide extra room for support structures and un-sprung mass must be kept minimal. Another drawback of the long active stack is that it aggravates the attraction forces. The attraction force calculations are presented in Appendix C. Finally the large resulting mass of PM1 reflects directly to cost, as it would require more material for construction.

The results of the power density based optimisation (PM2) are constrained to the required torque of 340 Nm. The results yields a shorter stack length (45% less), and thus a lighter and more compact design with reduced attraction forces. The torque is lower by 15%, but this comes in a 35% smaller volume, 31% lower mass and with 31% lower attraction force. Axial flux machines provide their highest power density levels at diameter ratios of around 0.6 - 0.7 [12] [21] [44] which closely agrees with the result of 0.68 found here. On the downside, the higher current density of PM2 would require additional cooling compared to PM1. It is also

worth noting that PM2 requires a slightly higher magnet height to attain a high power density level. Although not to scale, Figure 53 illustrates the optimised structures. With the majority of advantages in support of power density based PM2, it is therefore selected as the superior candidate.

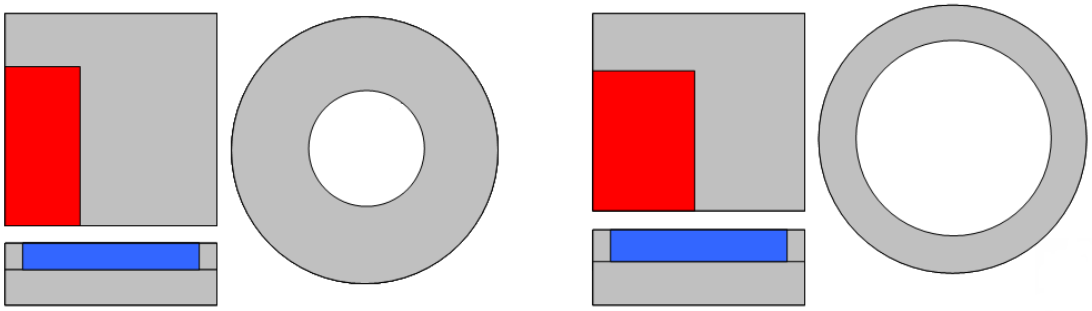

(a) (b)

Figure 53. Illustration of optimised machines a) PM1 and b) PM2

Finally, the machine voltage can be set by adjusting the number of series turns per phase. Assuming a 20 % buffer on the 440 V DC bus, the maximum machine phase voltage is calculated by

$$V_{\phi} = \frac{4}{\pi\sqrt{2}} \frac{V_{DC}}{2}, \tag{4.11}$$

yielding a phase voltage of 158 V_{RMS}. In the finite element program with 153 series turns per phase, this phase voltage is matched.

4.6.1 Results of 30-Pole 27-Slot Machine Model

A plot of the airgap flux density distribution for the linearised 30-pole 27-slot model is given in Figure 54. The open stator slots cause the unsymmetrical nature and the in-set magnet design causes the spikes showing up between the magnets. Figure 55 show the FE phase flux linkage waveforms from the two FE packages, Magnet 6® and Cambridge package. From the waveforms it can be seen that both packages are identical, thus verifying the result. In Figure 56, the *d*-*q* flux linkage components are shown against current angle. From the figure, the *q*-axis component is higher due to the in-set rotor design which provides the *q*-axis with a path of least reluctance.

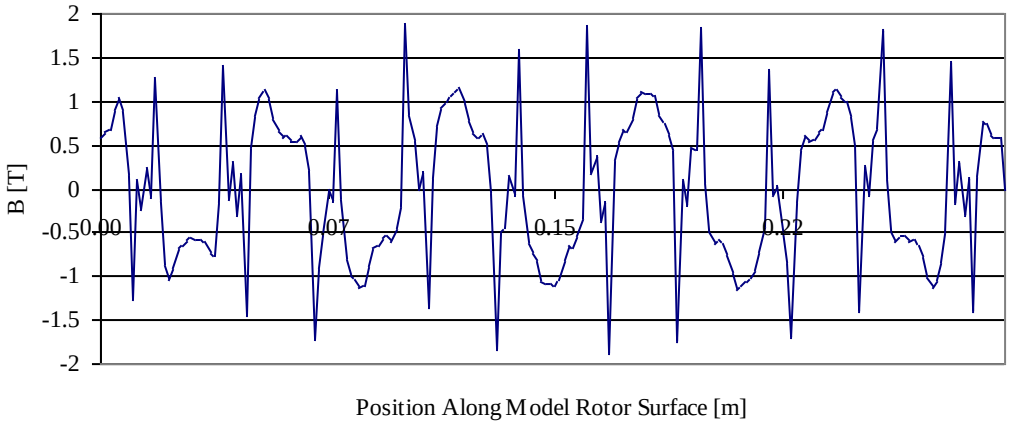

Figure 54. Magnetic airgap flux density plot of 30-pole 27-slot model rotor surface at no-load.

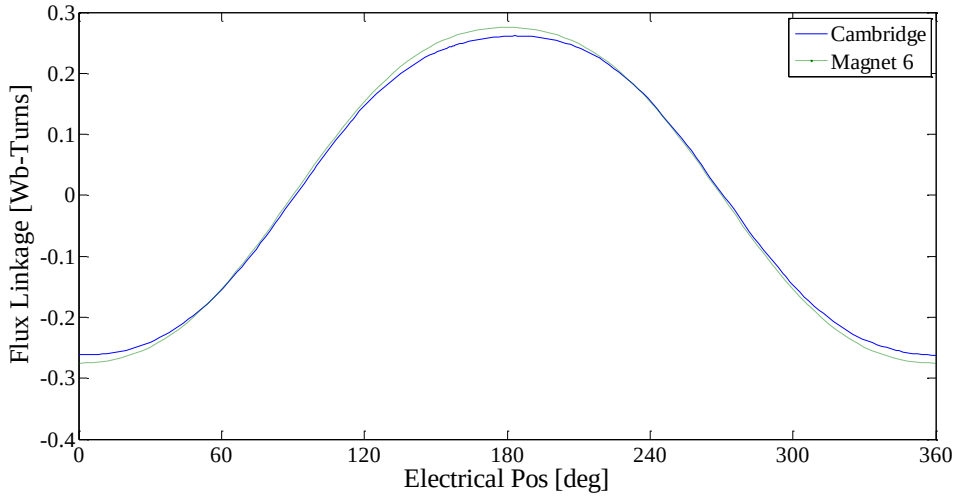

Figure 55. Per phase flux linkage obtained by two FE packages.

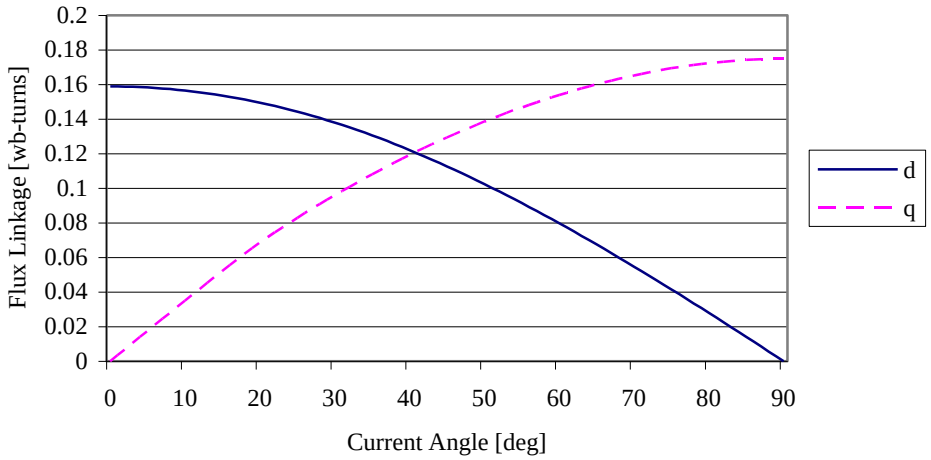

Figure 56. Flux linkage *d*-*q* components against current angle.

Due to the in-set rotor design, it is also interesting to look at the *d*-*q* inductances. Figure 57 shows the direct and quadrature inductances against current angle, which are calculated with the magnets in the off state in FE by equations (3.4) and (3.5). Like the flux linkages the *d*-*q* inductances of Figure 57 are also not equal. The *q*-axis inductance is higher as the quadrature path provided by the additional iron offers a better magnetic pathway. These inductances and equation (3.9) show that negative i_d is required for positive reluctance torque.

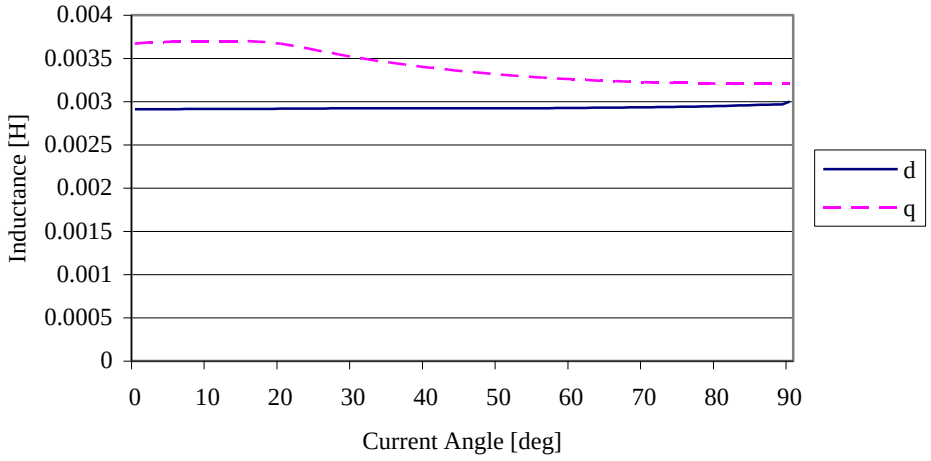

Figure 57. *d*-*q* inductances against current angle.

4.6.2 Torque Quality of 30-Pole 27-Slot AFPM

Of the several proposed design techniques to minimise torque ripple mentioned in section 3.7, here a basic variation of the magnet to pole pitch is investigated. This approach is the most practical, simple and least costly to implement. Peak to peak torque ripple is calculated by incrementally rotating the machine in small increments up to one cycle of 60 electrical degrees based upon the average computational plane. This is repeated for different values of magnet to pole pitch ratios, and the result is shown in Figure 58. The result shows the least torque ripple (11.2 Nm) is achieved at a magnet to pole pitch ratio of 0.94, 3.3% of the average. Further the instantaneous torque waveform at this point is shown in Figure 59.

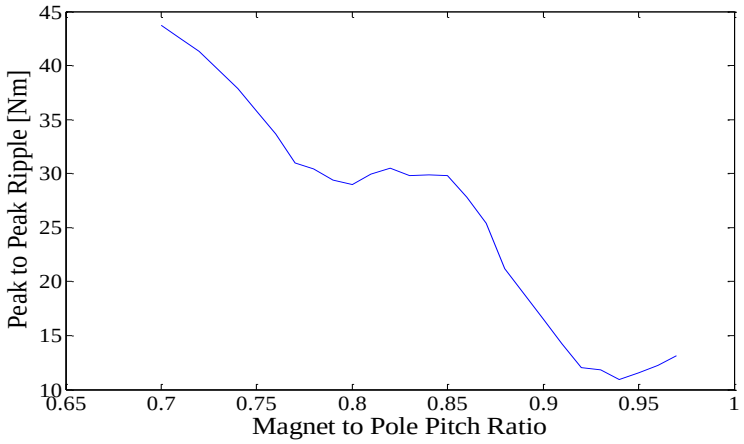

Figure 58: Peak to peak ripple torque against magnet to pole pitch ratio.

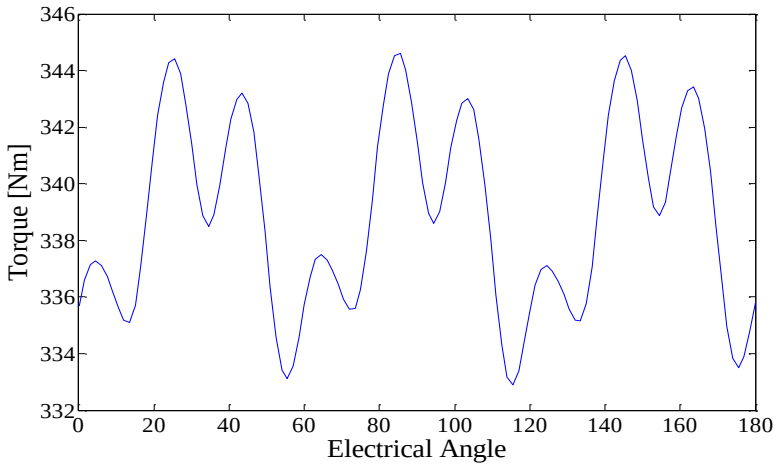

Figure 59. Instantaneous torque waveform at magnet to pole pitch ratio of 0.94.

4.7 Design Optimisations of 30-Pole 36-Slot Machines

Two additional design optimisations are carried out for 30-pole 36-slot single and double-layer machines for use as base machines in torque quality analysis. For the analysis of these machines, surface mounted magnets were used instead of in-set type. The models of these machines are based upon a $1/6^{th}$ sections (*GCD*=6) and with negative boundary conditions (odd pole pairs). The linearised models of the single-layer and double-layer 30-pole 36-slot machines are shown in Figure 60. The dimensions, materials and operating conditions used are the same as used in section 4.6. The winding layouts of the two machines are shown in Figure 61.

Both machines are optimised for T_{avg}*/volume* constrained by equal copper loss and outer dimensions as done previously, the results of which are presented in Table 5. From the

results the double-layer machine attains a higher power density level, but with a lower average torque.

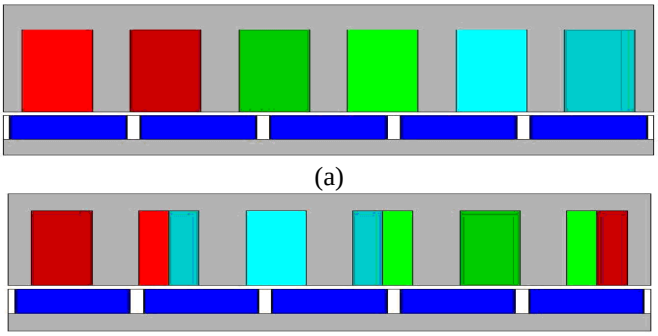

(a)

(b)

Figure 60. Linear models of 30-pole 36-slot AFPM machines, a) single-layer and b) double-layer.

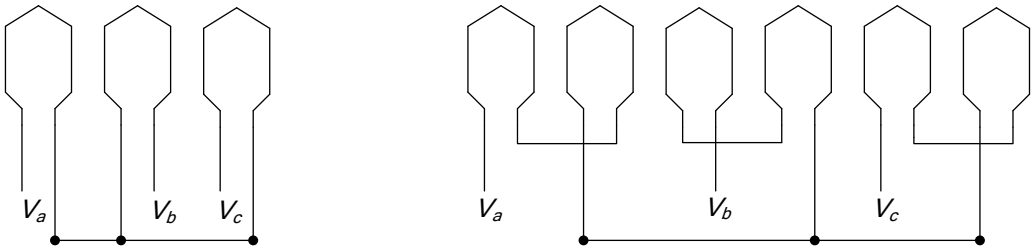

(a) (b)

Figure 61. Winding layouts of 30-pole 36-slot models a) single-layer and b) double-layer.

Table 5. Design Data of 30-Pole 36-Slot Base Machines

	Single-Layer	**Double-Layer**
Copper Loss	1200 W	1200 W
Stator outer diameter	330.0 mm	330 mm
Total axial length	55 mm	55 mm
Diameter Ratio	0.619	0.652
Magnet arc to pitch ratio	0.915	0.9
Slot to teeth width ratio	0.653	0.563
Tooth width ratio	1	1
Power Density	4366.39 kW/m^3	6343.55 kW/m^3
Average Torque	361 Nm	334 Nm
Synchronous Inductance	1.091 mH	0.58 mH
Cogging Torque p-p	0.459 %	0.543 %
Torque Ripple p-p	1.55 %	1.1 %

4.7.1 Results of 30-Pole 36-Slot Machine Models

The instantaneous cogging torque and torque ripple profiles of the two base machines are shown in Figure 62 and Figure 63. Multi-slice analysis is used to obtain the waveforms with by 5 computational planes (k_s = 5). The waveforms show similar cogging torques, but the double-layer torque ripple is smoother than the single-layer machine. It is convenient to express peak to peak cogging and ripple torque on a per unit / percentage system as

$$T_{p.u.} = \frac{\Delta T_{p-p}}{T_{avg}}, \tag{4.12}$$

with $\Delta T_{p\text{-}p}$ the peak to peak torque and the base selected as the machines average torque T_{avg}. In this manner it is possible to compare different machines without disregarding torque capability.

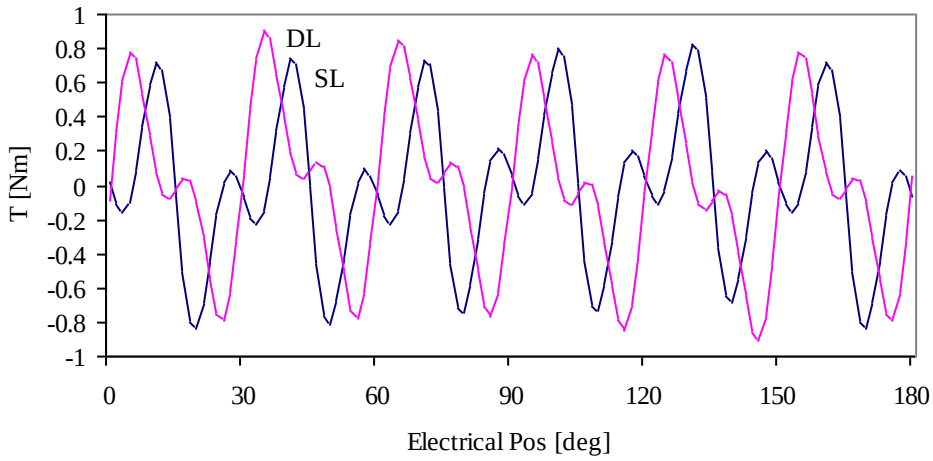

Figure 62. Instantaneous cogging torque waveforms of 30-pole 36-slot machines.

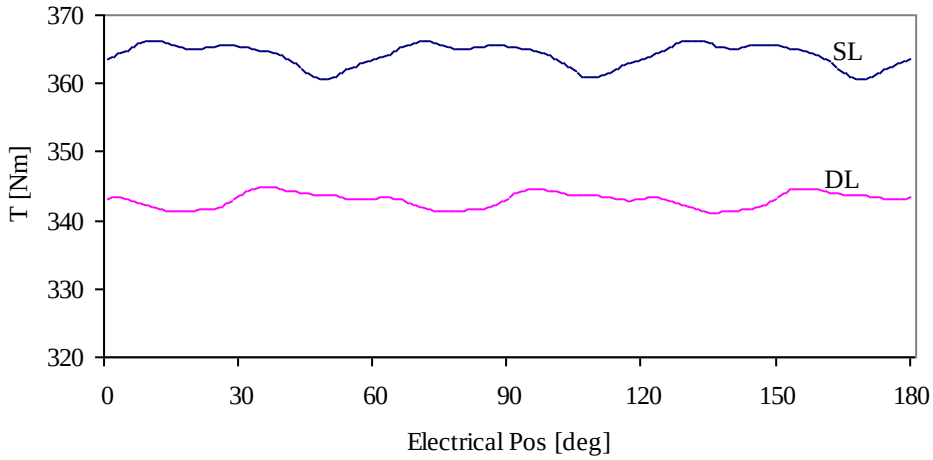

Figure 63. Instantaneous torque ripple waveforms of 30-pole 36-slot machines.

4.7.2 Optimising 30-Pole 36-Slot Machines for Torque Quality

In this section three design techniques mentioned in section 3.7 of cogging and torque ripple reduction are investigated, the effects of:

- Magnet to pole pitch ratio α_i,
- Slot to tooth width ratio k_{ST}, and
- Tooth width ratio k_{TW} (single-layer machines only).

Three machines are derived upon the two in section 4.7 are investigated for torque quality:

- A. DL machine with equal teeth,
- B. SL machine with equal teeth, and
- C. SL machine with un-equal teeth.

By using separately optimised single and double-layer machines, a fair basis is obtained, as compared to using one base machine which holds either a single or double-layer winding as was done in [61]. The problem of using one base machine is that the machine dimensions could be more suited to one winding type over the other.

Of all the work involving un-equal teeth machines mentioned in section 3.4, none deal with optimising the teeth ratio, particularly with other machine dimensions for torque quality. The optimisation objectives pursued here are:

- $T_{avg}/cogging_{p\text{-}p}$,
- $T_{avg}/ripple_{p\text{-}p}$ and
- $T_{avg}/copper\ loss$.

Two optimisation methods are used; the first involves a linear search and graphing method, applied to the DL machine. The second involving the Powell based optimisation algorithm is applied to both SL machines. The two methods are explained in the flow diagrams of Figure 64 and the results of which follow.

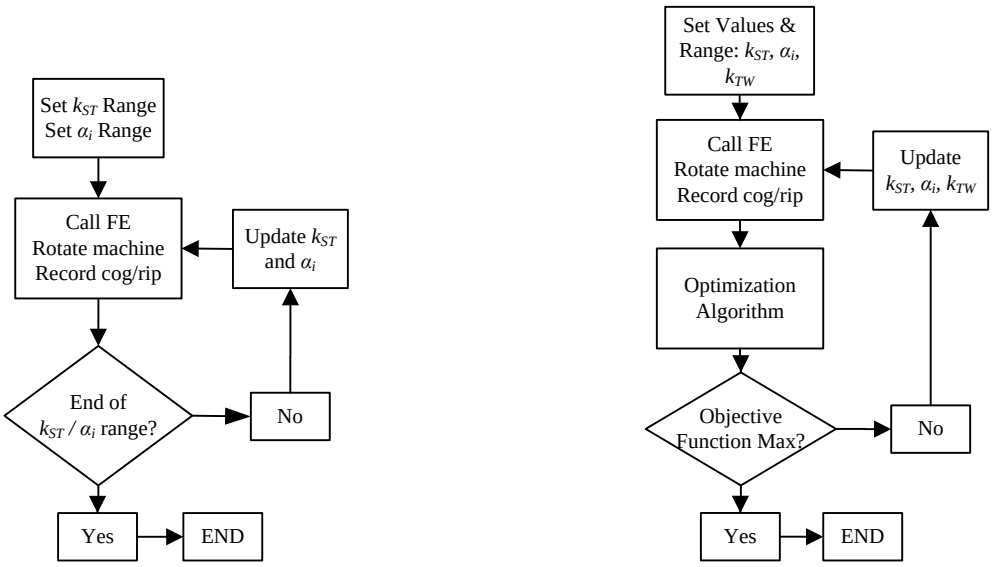

Figure 64. Flow charts of design techniques for a) double-layer machine and b) single-layer machines.

A. Double-Layer Machine (DL)

As double-layer topologies cannot use un-equal teeth, the optimisation parameters are limited to only two:

- Magnet to pole pitch ratio, and
- Slot to tooth width ratio.

The linear search method is applied to obtain the surface plots of Figure 65, Figure 66 and Figure 67. The points of minimum cogging, minimum torque ripple and maximum torque from the graphs are given in Table 6.

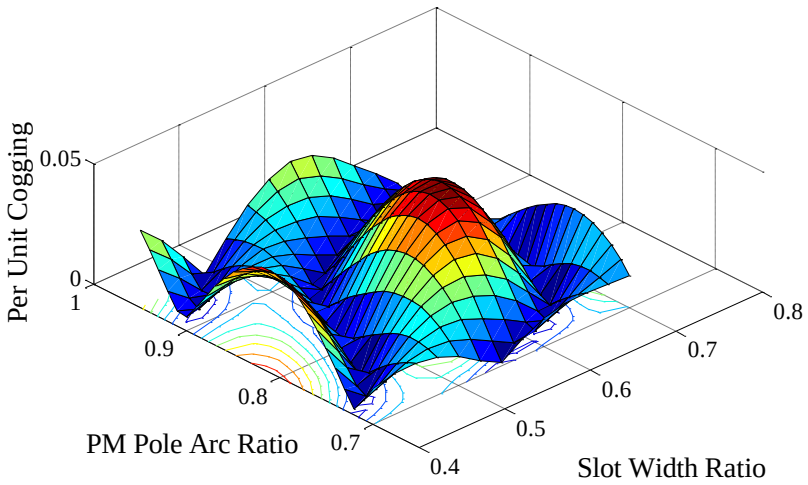

Figure 65. Per unit peak to peak cogging torque surface plot for double-layer machine.

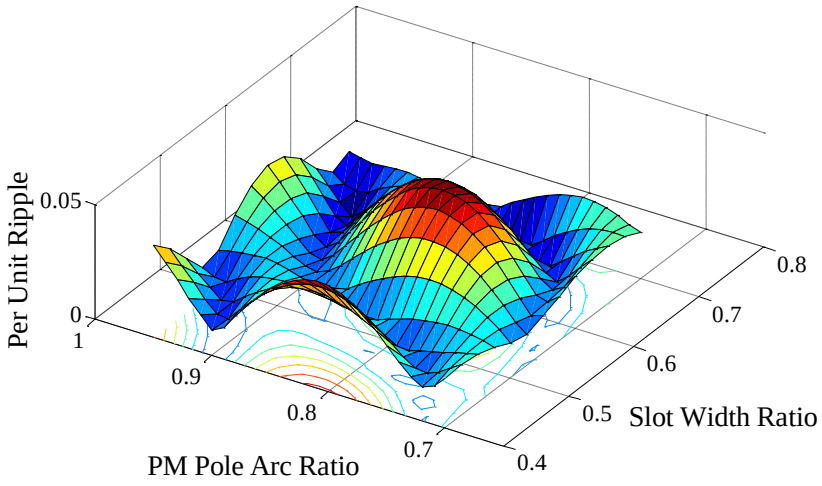

Figure 66. Per unit peak to peak ripple torque surface plot for double-layer machine.

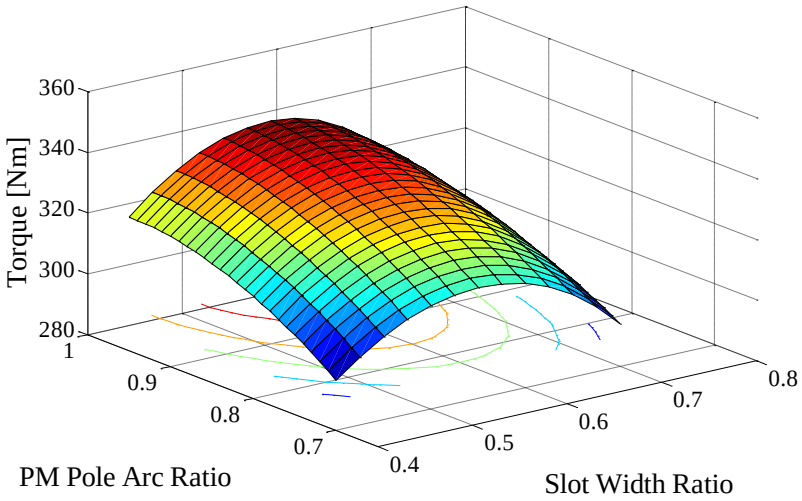

Figure 67. Average torque surface plot for double-layer machine.

B. Single-Layer with equal teeth (SL)

Similar to the double-layer machine, for the SL machine with equal teeth, the optimisation parameters are two:

- Magnet to pole pitch ratio, and
- Slot to tooth width ratio.

For this case the Powell optimisation algorithm is used and results are presented in Table 6.

C. Single-Layer with un-equal teeth (SLu)

For the SL machine with equal teeth the winding factor is limited to 0.966, but by introducing un-equal teeth the winding factor is adjustable. With the addition of un-equal teeth the optimisation parameters are three:

- Magnet to pole pitch ratio,
- Slot to tooth width ratio, and
- Tooth width ratio.

For the torque quality investigation of this machine, the Powell optimisation method is used. Figure 68 shows the machine model with un-equal teeth, and the optimisation results are presented in Table 6.

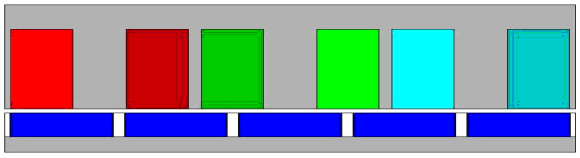

Figure 68. Linear model of single-layer machine with un-equal teeth (not to scale).

Table 6. Optimisation Results of 30-Pole 36-Slot Machines

		Slot Width Ratio k_{ST}	PM Pole Arc Ratio α_i	Tooth Ratio k_{TW}	Winding Factor k_{wn1}	Torque	Percentage p-p Cogging	Percentage p-p Ripple
A	DL Min Cogging	0.45	0.76	1	0.945	318.5	0.1	0.133
	DL Min Ripple	0.65	0.92	1	0.945	331.7	0.12	0.33
	DL Max Torque	0.55	0.95	1	0.945	345	0.029	3.36
B	SL Min Cogging	0.623	0.91	1	0.966	364	0.31	1.3
	SL Min Ripple	0.65	0.91	1	0.966	359.5	0.64	0.77
	SL Max Torque	0.562	0.915	1	0.966	368.7	1.4	2.6
C	SLu Min Cogging	0.623	0.91	1	0.966	364	0.31	1.3
	SLu Min Ripple	0.653	0.91	1.008	0.9677	359.7	1.05	0.44
	SLu Max Torque	0.555	0.93	1.083	0.9864	377	5.11	3.84

From the results and shown in Figure 69 the lowest cogging torque is obtained by the DL machine, but it suffers with a low average torque at that point. The SL machines each have the same level of cogging as in both cases the optimisation algorithm settles upon the same point. Un-equal teeth provided no advantages for cogging torque reduction in this investigation. On the minimum torque ripple results and shown in Figure 70, the DL machine

presents the smoothest torque, but again with a low average torque. The single-layer machine with un-equal teeth is not too far off and has the best average torque. From the maximum torque results and shown in Figure 71, the single-layer machine with un-equal teeth is best, but with the worst torque quality.

Relating back to the work done relating to un-equal teeth, [61] found that under BLAC operation machines with un-equal teeth have the worst torque quality. Here it is found that the single-layer un-equal teeth machine can be optimised to produce higher and smoother torque than its equal teeth single-layer equivalent.

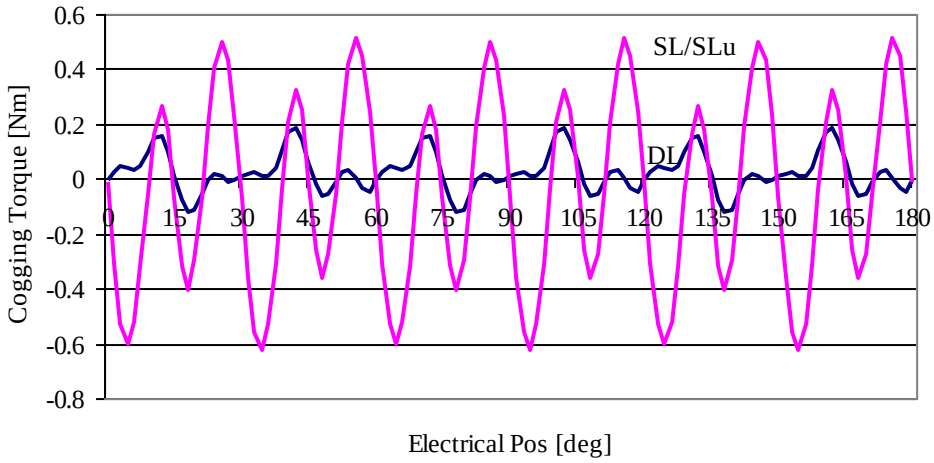

Figure 69. Optimised cogging torque waveforms.

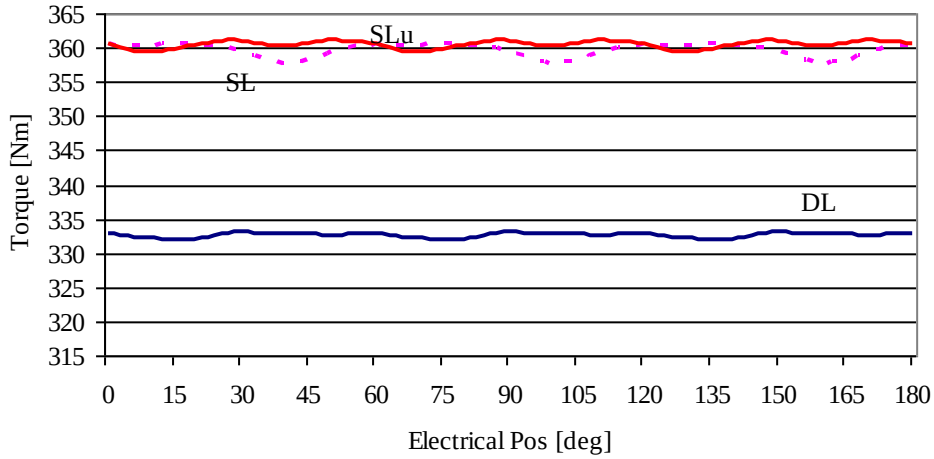

Figure 70. Optimised torque ripple waveforms.

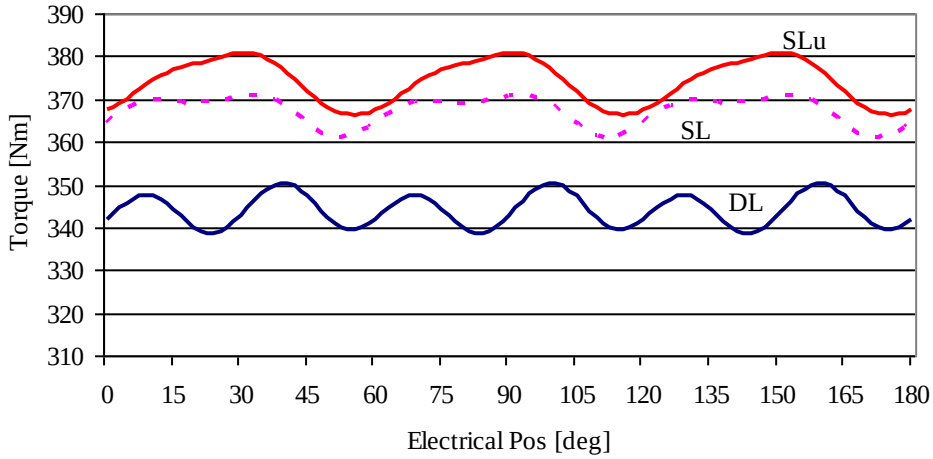

Figure 71. Optimised maximum torque waveforms.

4.8 Conclusions

In this chapter, linearised 2D FEM is used to obtain several AFPM machine designs. An optimisation algorithm further enhanced the designs for maximum efficiency, power density and torque quality. The power density optimisations led to small and compact machine designs which are ideal for hub drive applications.

In the section on torque quality optimisation, the approach adopted essentially treated the machines as “black boxes” and yet proved a simple and effective method to directly improve torque quality. The best torque quality is obtained by the double-layer machine, but it is found that single-layer machine with un-equal teeth presents the best average torque per ripple characteristic.

5. Prototype Machine

In order to verify the FE design results, a prototype machine is built. The machine selected for prototyping is the 30-pole 27-slot double-layer machine PM2 optimised for power density. Several load and no-load tests are performed in this chapter along with cogging and temperature measurements. Closing is a short investigation into the reduction of rotor iron losses.

5.1 Mechanical Layout

The PM machine was built in house by the Department of Electrical Engineering, Stellenbosch University. Appendix D presents the prototype machine specifications along with those of a radial flux counterpart machine previously built as Stellenbosch University. Figure 72 shows the unassembled machine and Table 7 presents the mass of various machine parts. In Appendix E, the mechanical layout of the prototype machine is shown. The rotor was made by assembling N40SH grade magnets into an in-set mild steel disk using adhesive glue. A company in china [63] was identified who manufacture high quality axial flux machine rotors and stators by the incremental punching method, unfortunately this was ill-timed and the prototype machine stator was made from M5 GOSS toroidal core with open stator slots machined into. Non-overlap pre-formed coils were placed over each tooth, insulated using Nomex paper. An aluminium cooling pipe was hand formed and placed upon the outer end windings. Two temperature sensors were placed into the winding and the stator was placed into a mould. Epoxy resin was poured into the mould and the complete stator was oven cured at for 3 hours.

Table 7. Mass of Prototype Machine Components

Active Structures	**Mass [kg]**
Stator Core	5.831
Coils (27)	4.657
Rotor Disk	5.003
Magnets (30)	3.423
TOTAL	18.914

Support Structures	**Mass [kg]**
Back Stator Support	2.55
Stator Support Blocks	2.619
Epoxy	1.6
Bearing Housing	3.385
Hub	5.179
Resolver Support	0.123
Bearing	1.86
TOTAL	17.316

The total mass of AFPM hub motor is 36.23 kg. The hub, bearing and its housing cannot truly be attributed solely to the machine, as these structures are also related to supporting the vehicle wheels and mass. Disregarding these structures, the overall mass of the machine can be more realistically realised as 25.8 kg, just slightly over the design objective of 25 kg. The assembled machine is shown in Figure 73.

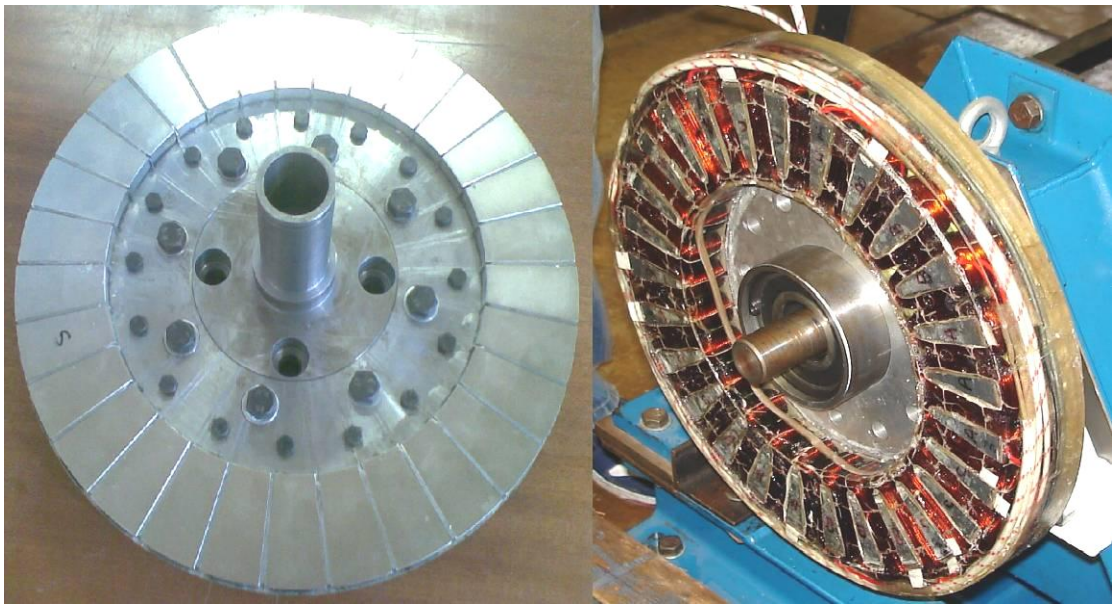

(a) (b)

Figure 72. Unassembled prototype machine, a) rotor with hub and b) stator with bearing housing.

(a) (b)

Figure 73. Assembled hub machine a) without rim and b) with rim fitted.

5.2 Test Bench Layout

On the test bench the AFPM machine is coupled to a 36 kW induction machine via a 1000 Nm torque sensor and 3:1 gearbox as shown in Figure 74. During loading conditions, the

induction machine was used as load; this was achieved by running the induction machine under a speed control algorithm and over-running it with the AFPM machine. During this over-run into the second quadrant of operation, the induction machine drive would dynamically brake excess energy into a water cooled resistive load bank (not shown).

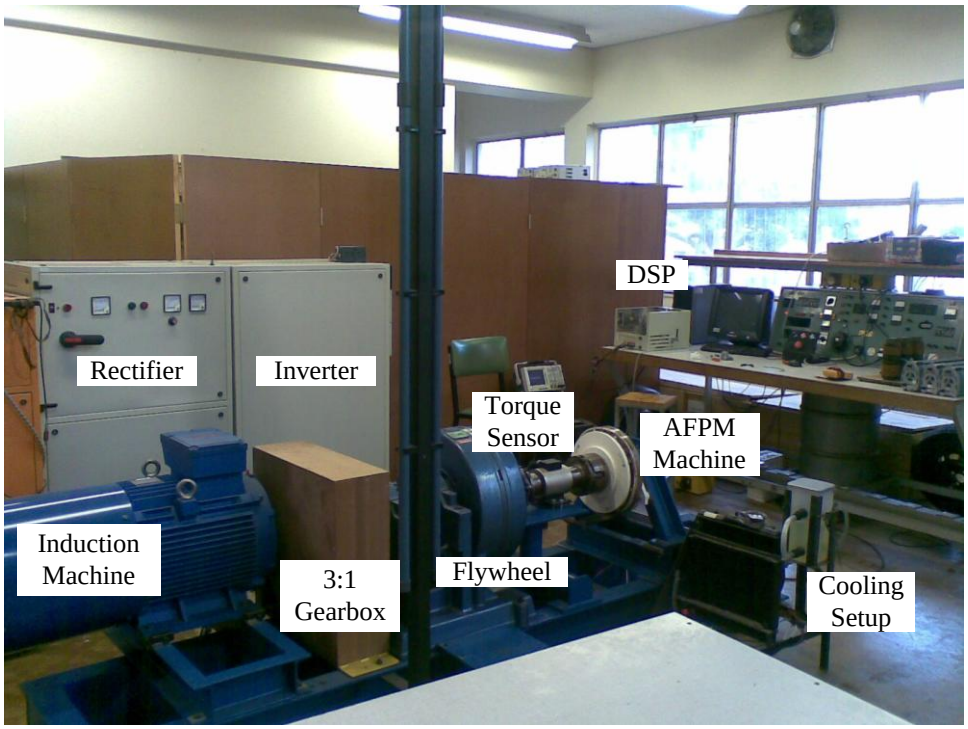

Figure 74. Laboratory setup.

5.3 Generator Tests

Before performing any motor tests on the machine, a series of generator tests were carried out; specifically the open and short circuit tests. Just before the generator tests were carried out, the phase resistance of each of the machine windings was measured using a Milli-Ohmmeter, with the results presented in Table 8. The FE and measured results are fairly similar.

Table 8. Measured and FE Phase Resistance

Phase	A	B	C	FE
Resistance [Ω]	0.23	0.23	0.229	0.245

5.3.1 Open Circuit Test Results

The open circuit test was performed by having the machine terminal open circuit and driving the machine with the induction motor until rated speed was reached and measurements taken. The scoped three-phase open circuit voltage waveforms are shown in Figure 75, and the measured and FE values are given in Table 9. The torque measured during the test was 12 Nm at 450 r/min, equating to open circuit losses of 565.5 W.

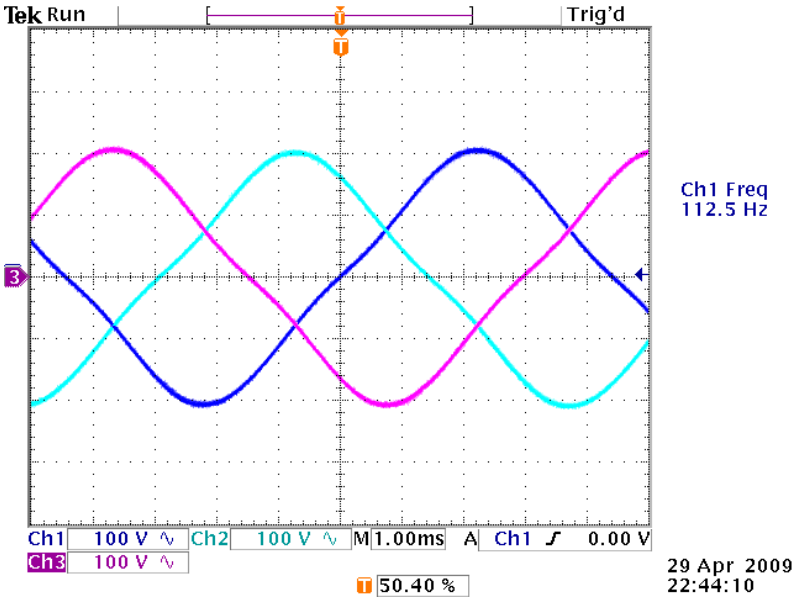

Figure 75. Measured three-phase open circuit voltage waveforms.

Table 9: Measured, Calculated and FE Voltages

Calculated	159.4 V_{RMS}
FE	155.5 V_{RMS}
Measured	151.3 V_{RMS}
FE Error	2.70 %

In FE the instantaneous back EMF e can be calculated by taking the flux linkage time derivative as the machine is rotated

$$e = \frac{d\lambda}{dt} = \frac{\lambda - \lambda'}{x - x'}, \tag{5.1}$$

where λ and λ' are flux linkages based on positions x and x'. In Figure 76 the measured and FE results are compared.

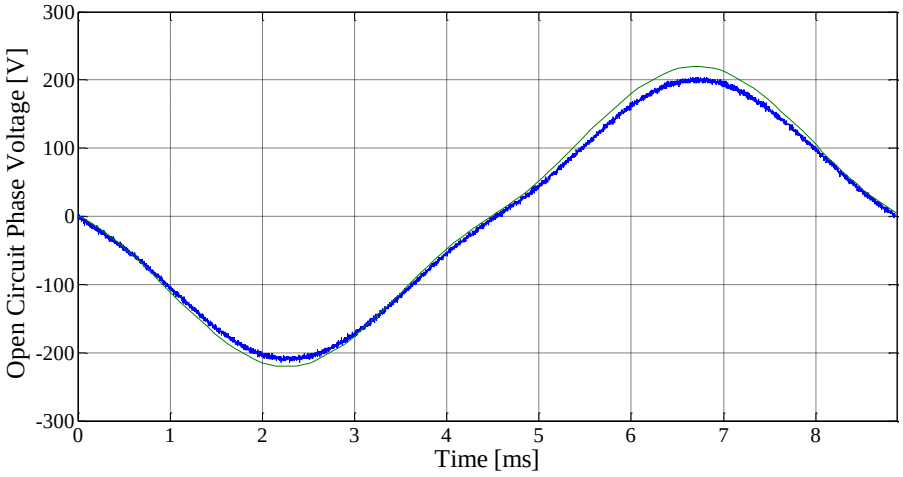

Figure 76. Measured and FE open circuit voltage waveforms.

5.3.2 Short Circuit Test Results

The short circuit test was carried out by shorting the machine terminals and driving the machine until rated current flowed in the windings. In Table 10 the recorded results during the test are presented.

Table 10: Short Circuit Test Results

$I = I_{sc}$	38.5 A
T	222 Nm
Speed	60 r/min
E_{sc}	19.1 V

Total losses measured during the test are 1394.9 W. Taking into account the copper losses (1200 W), a balance of 194.7 W is recorded. Form the short circuit test, the synchronous reactance can be determined by

$$X_s = \frac{E_{sc}}{I_{sc}}, \tag{5.2}$$

where E_{sc} is the open circuit voltage at short circuit test speed, and I_{sc} is the short circuit test current. The calculated and finite element synchronous reactances and inductances are presented in Table 11 and are quite similar.

Table 11: Measured and FE Inductances

	L_s [mH]	$X_{s\ (15.15Hz)}$ [Ω]
Measured	4.32	0.412
FE	4.35	0.414

5.4 Cogging Torque Measurements

The cogging torque was measured by taking several static torque measurements with a setup as shown in Figure 77. An offset weight was wound with a rope around the machine hub so as to avoid the torque pulsation around '0' as the torque changes sign. A threaded holding assembly was used to slowly rotate the machine and hold positions as measurements were taken. Two sets of results were taken for clockwise and anti-clockwise rotation. The offset weight effect was subtracted, and the two results averaged. The measured result and the FE result are shown in Figure 78.

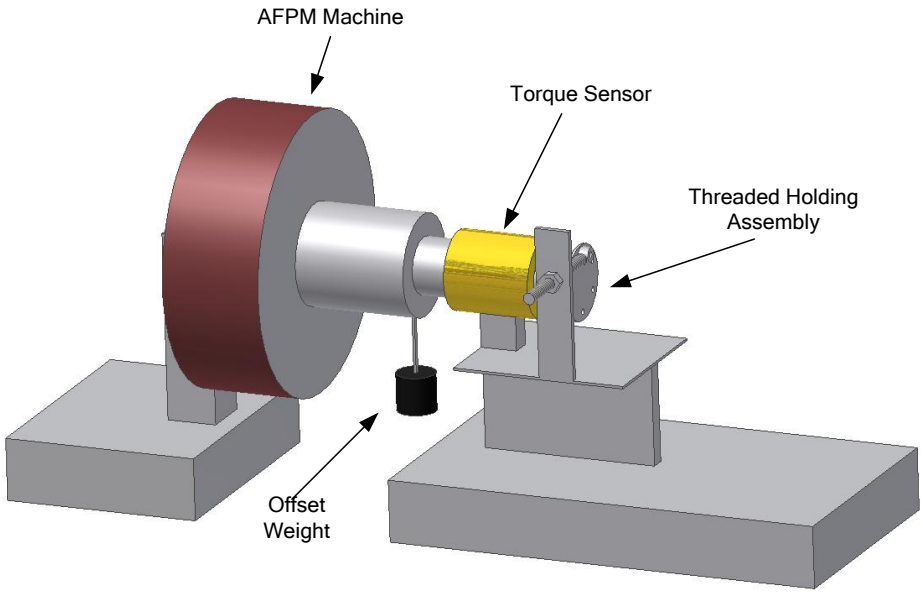

Figure 77. Experimental setup for cogging torque measurement.

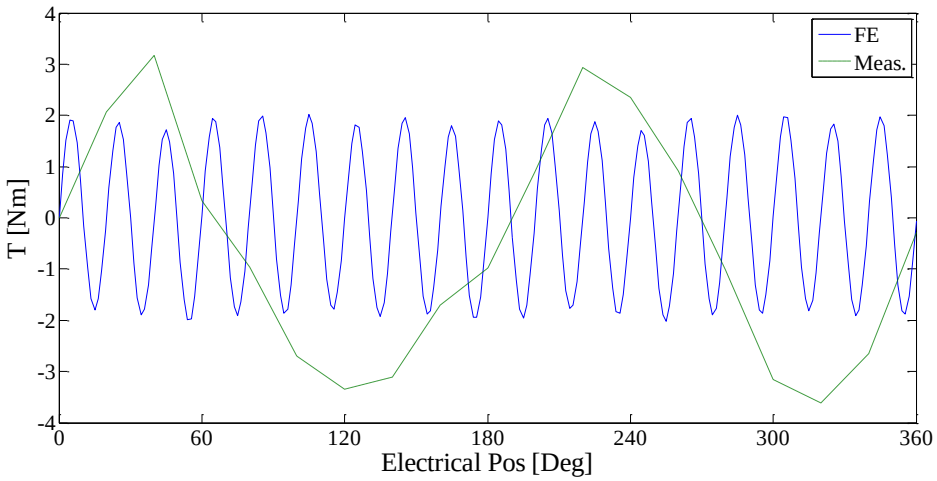

Figure 78. Measured and FE cogging torques.

From the cogging torque measurements it is evident that the theoretical and measured results are unlike. Instead of 270 high frequency cycles per one mechanical revolution, only 27 low frequency cycles (period 200°) are observed with a peak to peak value of 6.78 Nm (2 %). In investigating this further, a Gauss meter was used to measure the magnetic flux density above all the magnets in the motor, with the results shown in Figure 79.

From the measured results of Figure 79 it is clear that all flux densities above the magnets are not uniform, this most likely due to magnetisation differences from the magnet supplier, an un-equal airgap effected during assembly or anisotropy effects in the iron laminations. By using an error band of 1.0375 - 1.0525, magnets falling above these boundaries were set slightly stronger, and those falling below set slightly weaker and incorporated into the FE model. In order to incorporate all 30 magnets, a full model of the machine had to be modelled, due to the unsymmetrical distribution of the un-equal magnets. This model shown in Figure 80 and the FE and measured cogging results are presented in Figure 81. By incorporating un-equal magnets, a much closer FE result is obtained, with a large low frequency component realised. Unfortunately due to the small mechanical rotation angles and unavailability of precise angle measuring tool, along with poor sensitivity of the available torque sensor, a more precise measurement encompassing the higher frequency cogging component could not be achieved. A similar problem of capturing the higher frequency cogging torque components was also reported in [63].

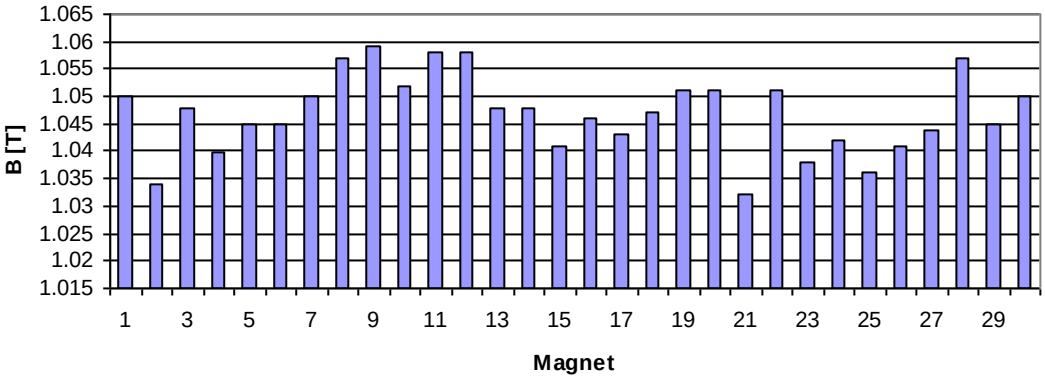

Figure 79. Measured flux density above prototype machine magnets.

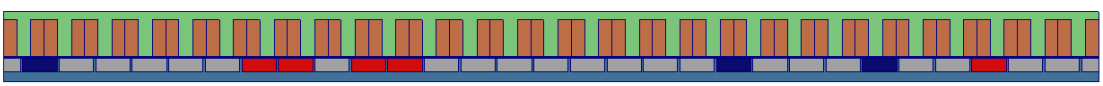

Figure 80. Full FE model with un-equal magnets. Blue weak and red strong.

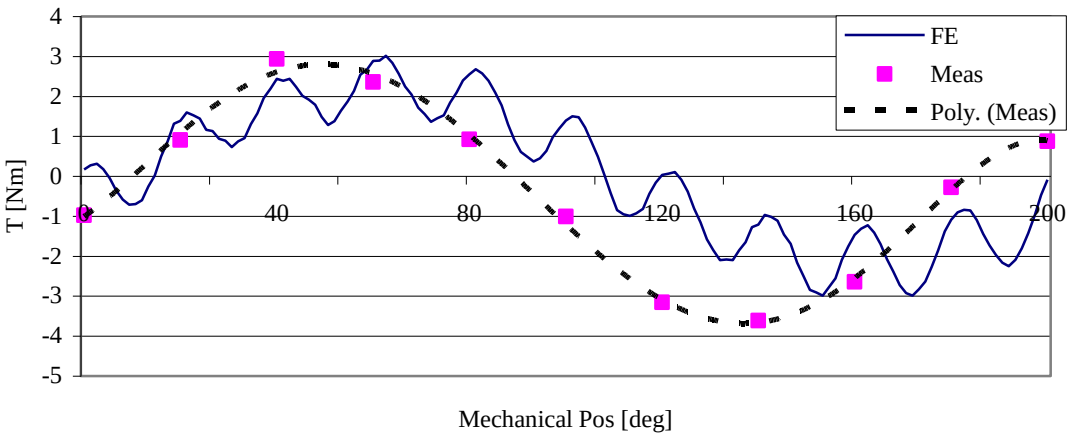

Figure 81. Measured and un-equal magnets FE results.

5.5 Drive Tests

In order for motoring tests to be carried out, a digital signal processor (DSP) controller had to be used. The unit used is based upon a Texas Instruments TMS320VC33 chipset and was developed in house for the Electrical Machines group. The DSP controller was connected up similar as in Figure 6 and was used to produce PWM voltages via IGBT switches of the half bridge inverter. Optic fibre links were used to connect the DSP to the IGBT switches to ensure electrical isolation to protect the DSP. Figure 82 shows the layout of the DSP controller and in Figure 83 the DSP is shown with the PC interface. The analogue to digital (ADC) converters received measurements of currents and position, with digital to analogue (DAC) converters used to enable viewing of parameters via oscilloscope. Field orientated control was implemented in the DSP to control the AFPM machine under a torque / current control algorithm.

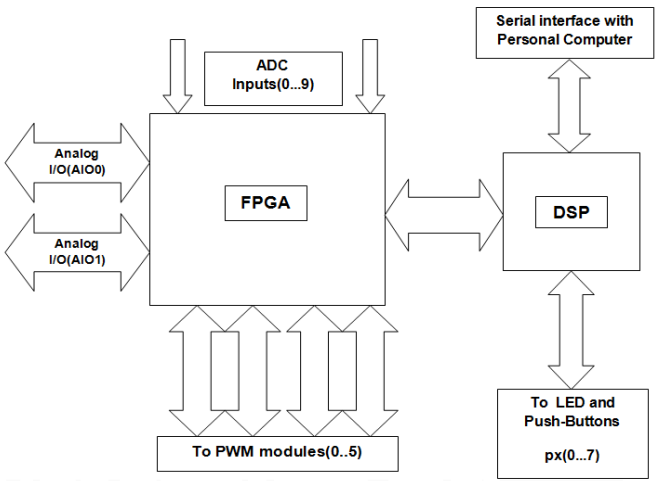

Figure 82. Layout of DSP controller.

Figure 83. DSP and PC interface.

5.5.1 Motor Tests

Two motoring tests were carried out to verify the performance of the AFPM machine. In Figure 84, the measured and FE torque versus current result is shown with $i_d = 0$. In Figure 85, the torque response is measured at fixed torque loadings of $\frac{1}{3}^{rd}$, $\frac{2}{3}^{rd}$ and rated; with each loading the current angle is varied. The results show the measured results the FE results matching up quite well.

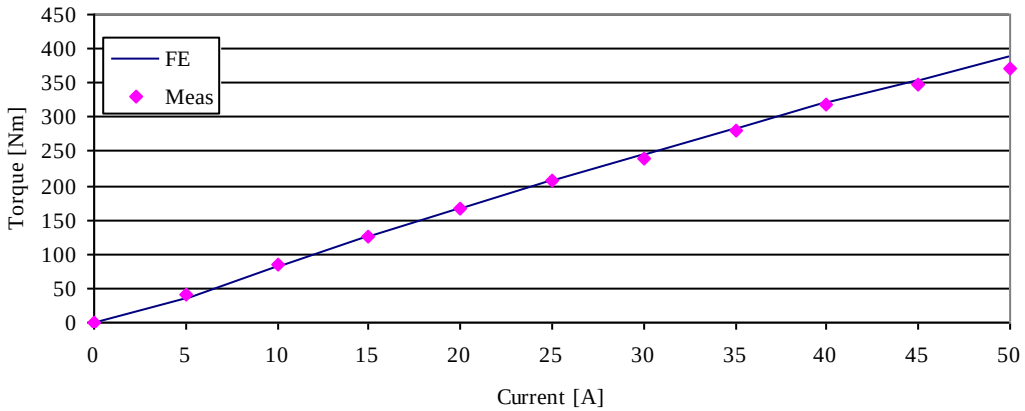

Figure 84. Measured and FE torque with current loading with i_d=0.

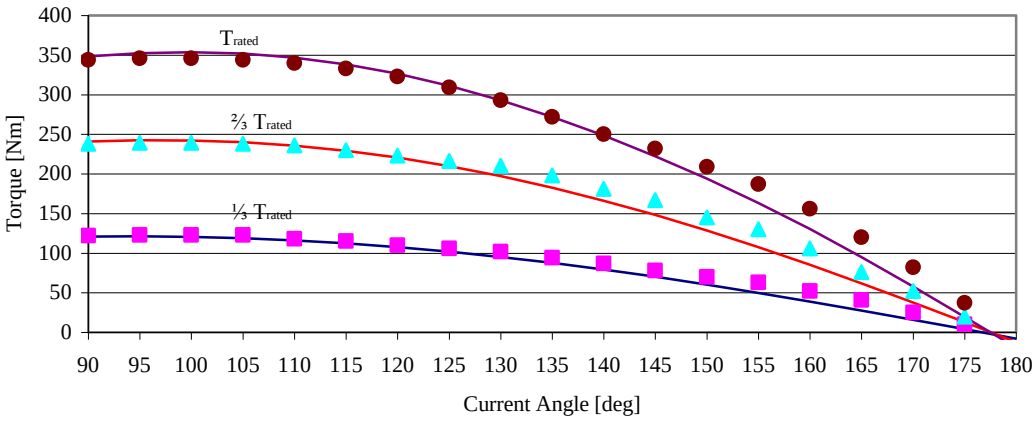

Figure 85. Measured and FE torque results against current angle.

5.5.2 Flux Weakening Performance

The flux weakening performance of the machine can be determined in the FE program by increasing the speed and by increasing the current angle accordingly, as show in the flow diagram of Figure 86. Figure 87 shows the torque speed characteristics for different loadings and for the cases of surface and in-set magnets. As can be seen from Figure 87, by using in-set magnets, the flux weakening performance is extended. From the FE simulation, the maximum speed obtainable by the AFPM machine is 1150 r/min, 2.5 times the machine's base speed. Returning to the vehicle requirements (Section 2.4) of 87 Nm per motor at 120 km/h (1200 rpm), the maximum performance the vehicle can obtain is 105 km/h (1050 rpm), just short of the design requirement. No measurements in the high speed flux weakening region were conducted due to problems that are described in the next section.

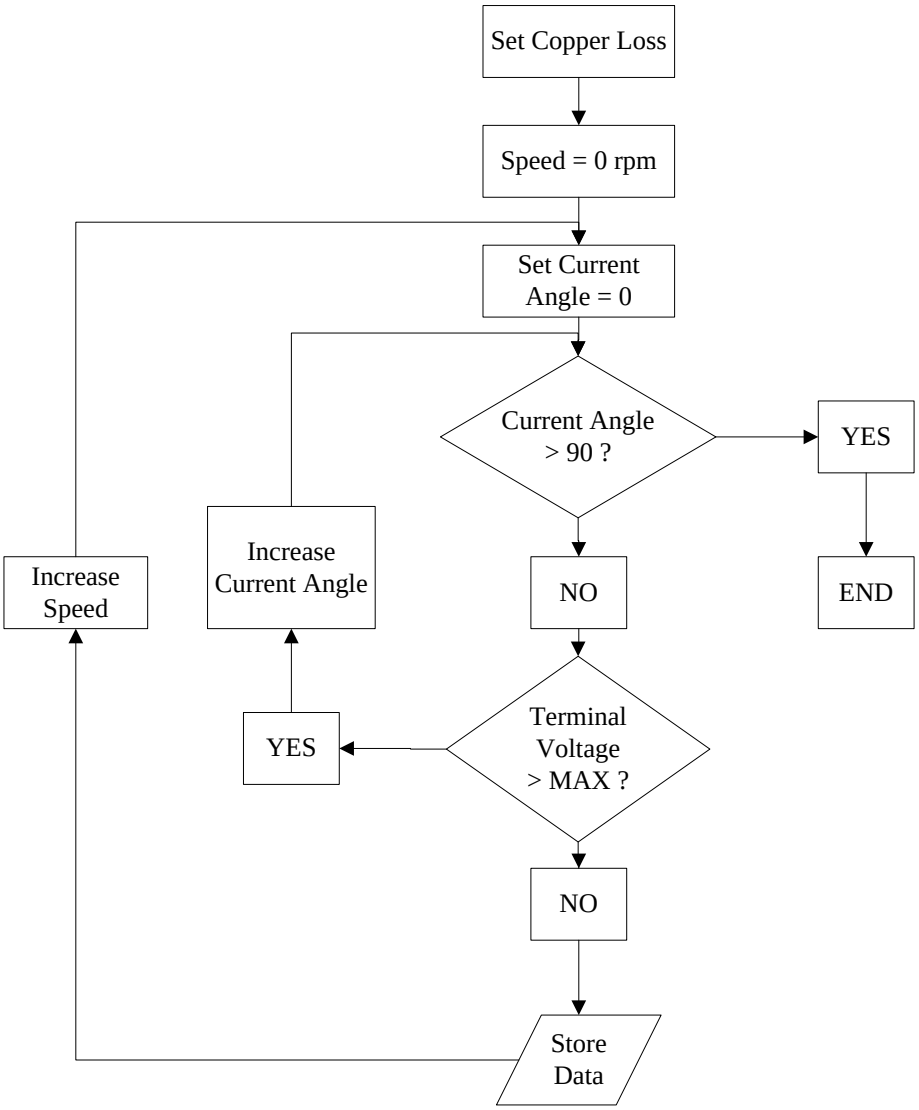

Figure 86. Flow chart of FE method to obtain flux weakening performance.

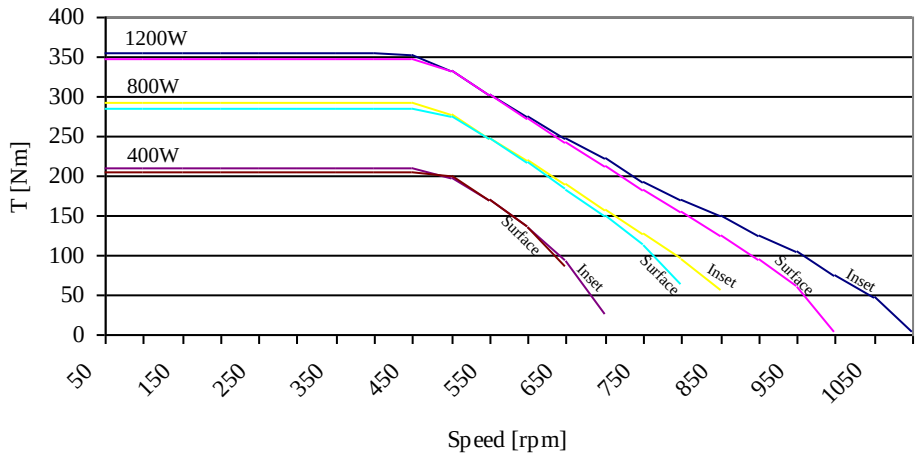

Figure 87. FE flux weakening results.

5.6 Temperature Measurement

Temperature tests were carried out in the rotor and stator parts of the machine. For tests of the rotor circuit, the machine was run open circuit at rated speed over period of time with the results shown in Figure 88. An infrared temperate sensor was used to measure temperature on the outer surface of the rotor disk. During the test, the temperature rise was very high and the test was abandoned to avoid demagnetising the magnets. Due to the high rotor losses at base speed, no tests were carried out in the high speed flux weakening regions. The high temperatures measured can only be owing to high losses in the rotor circuit, which is discussed in the next section.

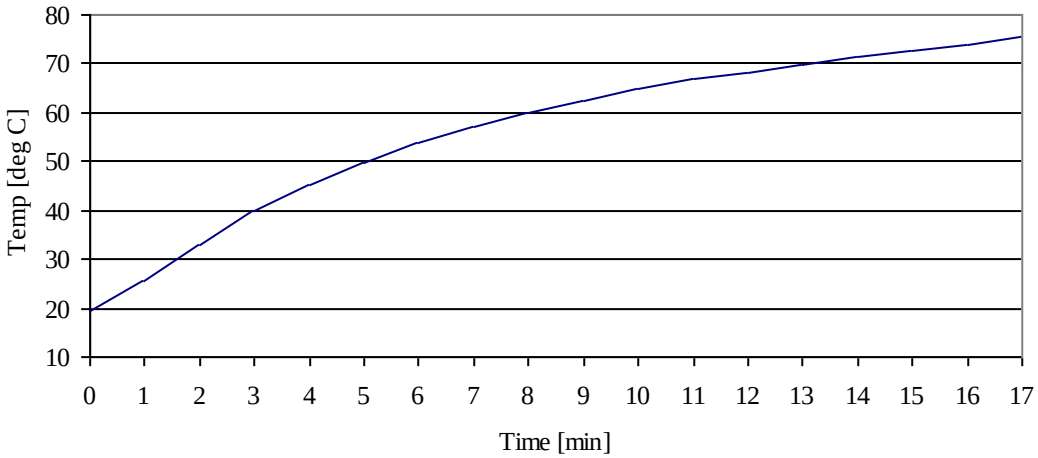

Figure 88. Measured no load rotor disk temperature rise at base speed.

For the stator, the temperature test was done by short circuiting the machine windings (to keep all other losses low) and driving the machine until rated current flowed in the windings. Liquid cooling was provided along the outer end windings of the machine via a 24 mm^2 aluminium cooling duct, with a water flow rate of 3.5 L/min. Temperature measurements were taken using three PT100 RTD sensors, two positioned at opposite sides of the stator and one in the water output duct. The measured temperatures for the three zones are shown in Figure 89. The copper used in winding the machine was insulated with armoured polyesterimide (API) rated up to 220°C. During the test this limit was nearly reached, and thus the cooling deemed inadequate. From the water measurement, it can be noted that the sluggish temperature rise is a sign of poor heat transfer.

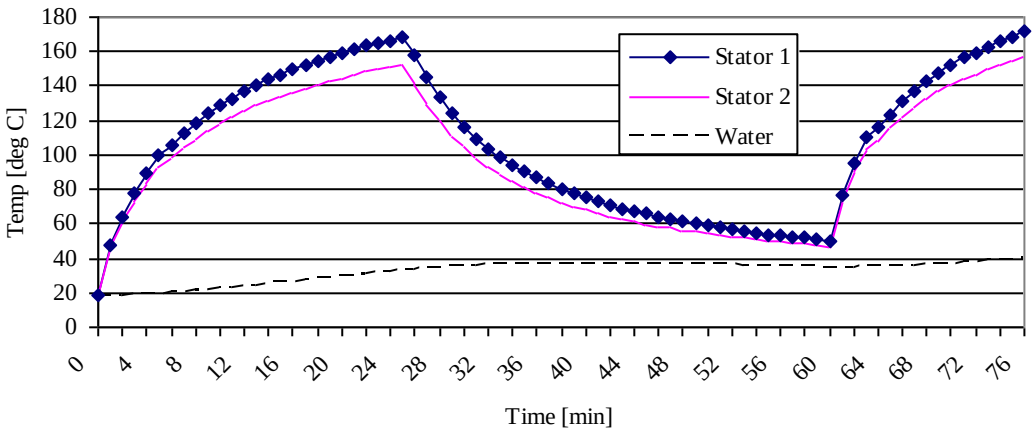

Figure 89. Measured stator and cooling water temperatures over duty cycle.

The cooling configuration for the stator was novel and never had been tested at Stellenbosch University for axial flux machines. Problems could be attributed to the cooling duct not uniformly touching the windings as it was hand formed, and that epoxy had displacing the pipe from the windings in a few areas. From FE based cooling simulations in Appendix F, the heat from the winding is first transferred to the iron laminations, and then the aluminium back plate, a suggestion for future designs is to have the stator cooling ducts machined into the back aluminium stator support disk.

5.7 Reducing Rotor Yoke Losses

During the design stage of the AFPM machine, sourcing of very thin width (6 mm) toroidal tape wound laminated iron for the rotor yoke was difficult and the structural integrity of such thin laminated tape was questionable. A choice was made to use a solid iron disk instead and the rotor eddy current losses were underestimated during the design stage and the prototype machine was beset with high rotor temperatures. Towards the end of this study a new version of Magnet 6® finite element package was obtained that could determine rotor losses. FE simulations into rotor losses were carried out and Figure 90 (a) shows the concentration of the losses in the rotor; these can be seen concentrated within the regions between the magnets of the in-set design. Had the magnets been surface mounted, the distribution would be as shown in Figure 90 (b). From the FE results, it was found that the losses associated with the inner magnet in-set pieces contribute to 25 % of the total rotor losses when using a solid mild steel rotor.

As the magnets of the prototype are fixed in the in-set design removal of the inner iron could not be done. FE was used to investigate the effect of removing material from the back of the rotor yoke, in the area in-between the magnets as shown in Figure 91. The aim of this modification is to push the associated iron area into a high degree of saturation to limit the eddy current circulations.

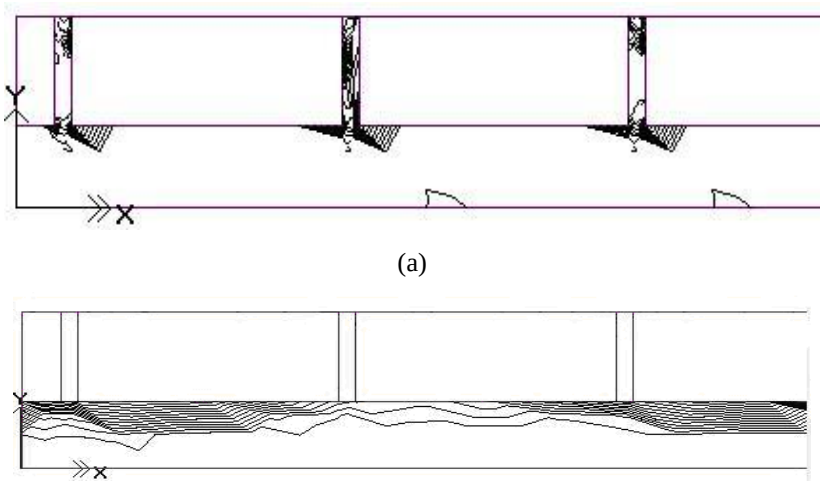

(a)

(b)

Figure 90. Distribution of rotor losses in a) inset rotor and b) surface rotor.

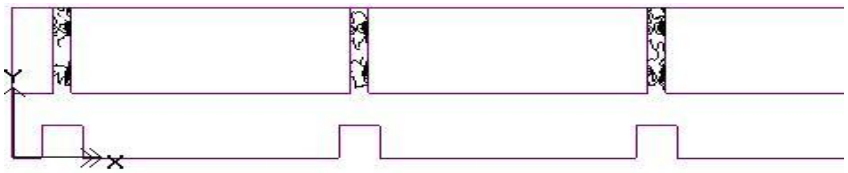

Figure 91. Distribution of losses of inset rotor with yoke modification.

Several rotor designs shown in Figure 92 were investigated for rotor yoke losses:

- a) Inset magnets,
- b) Surface magnets,
- c) 0.5 x 6mm slits,
- d) 4 x 4 mm slits,
- e) 4 x 6 mm slits,
- f) 6 mm diameter holes,
- g) 2 mm thin yoke, and a
- h) M19 laminated silicon steel rotor,

The resulting FE predicted losses are given in Table 12. The conductivity used for the mild steel disk simulations was 2 x 10^6 S/m. The simulations were carried under full load conditions for a variety of speeds. It is found from FE that at no-load eddy current losses are about half of the full load losses.

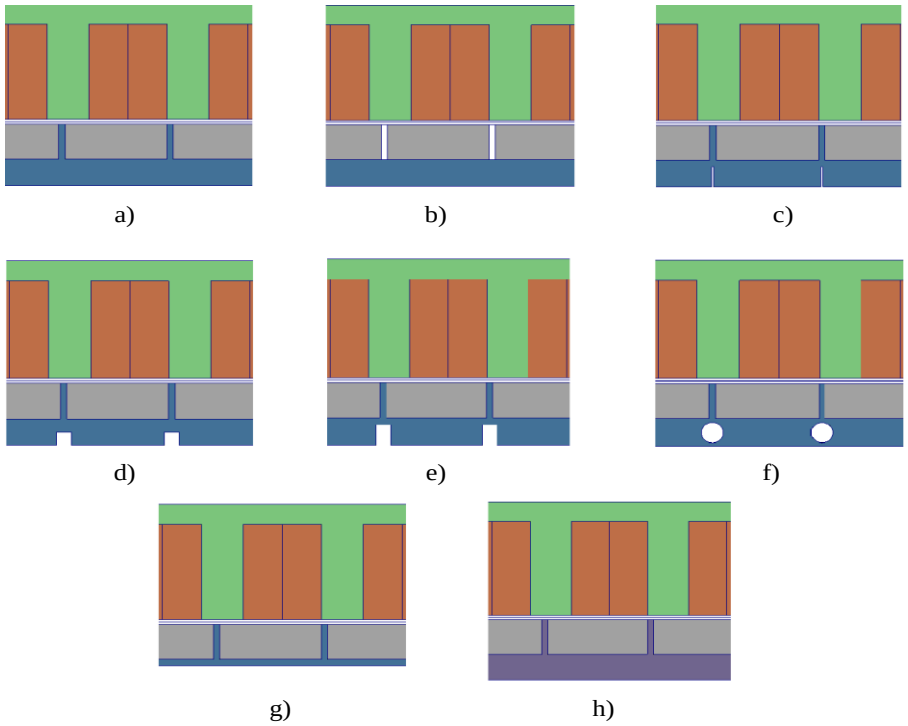

Figure 92. Investigated modifications to reduce rotor eddy current losses, a) In-set, b) surface, c) 0.5 x 6 mm cuts, d) 4 x 4 mm cuts, e) 4 x 6 mm cuts, f) 6 mm holes, g) 2 mm yoke and h) M19 Laminated Steel.

Table 12. Full Load Rotor Eddy Current Losses for Various Rotor Designs

	a) Inset	b) Surface	c) 0.5 x 6 mm cuts	d) 4 x 4 mm cuts	e) 4 x 6 mm cuts	f) 6 mm holes	g) 2mm yoke	h) M19 Laminated Steel
Speed [r/min]	Full Load Rotor Eddy Current Losses [W]							
50	21	6.3	5.4	9.3	3.6	6.9	1.05	29.46
100	61.5	21	19.5	28.5	12	24	3.6	30.15
450	900	255	300	525	210	420	67.5	44.1
900	2700	810	1320	1710	825	1500	240	82.44
1350	5400	1500	2700	3375	1725	3300	510	143.4
T_{avg} [Nm]	332.4	338.6	322	340.7	301.2	305.4	278.38	344.86

From the FE results, it is found that the best reduction in eddy current loss using a solid mild steel disk is obtained by using a very thin rotor yoke of 2mm, the disadvantage of this is that it also yields the lowest average torque. Secondly the results of using surface mounted magnets show the next best reduction of rotor losses and demonstrate how critical it is to correctly implement in-set rotor designs. The best results were obtained by simulation with a M19 laminated steel rotor. The laminated disk yields the lowest losses and also the highest average torque. Interestingly, the losses in the solid mild steel disks at low speeds are less than the case of the laminated disk. For low speed applications, this phenomenon could be quite advantageous as solid disk are easily manufactured and sourced. Measured results of rotor modifications are not obtained due to the complexities involved with machining the rotor disk with magnets attached.

To verify the structural integrity of cutting of the rotor disk, a structural FE model is setup. In the model, the worst case scenario of a complete cut right through the rotor disk between the magnets is considered. The FE result is given in Appendix C and it is found that the deformation of disk due to the attraction force reduces the airgap length at the outer peripheral only by 2.2 %, which is within reasonable limits.

Thermal FE simulations are carried out to show the heating of the rotor due to the eddy current losses. The maximum temperature tolerable by N40SH magnets is 175 °C depending on the operating point. To ensure a safe buffer, the maximum temperature is assumed 85 % (148 °C) and this is obtained with 210 W losses induced (shown in Appendix F). From the FE solutions all the solid rotor disk variants violate the 210 W limit (violations in Table 12 shown in red), only the case with a M19 laminated rotor satisfies the thermal limits; on this basis it can be assumed that solid mild steel rotor disks are unsuitable for this application.

In summary, modifications to the solid iron rotor disk do not provide substantial eddy current loss reduction suitable for hub drive applications. The best initiative would be to use only laminated electrical steels. It is worth noting that solid mild steel rotor disks are appealing to low speed applications, such as low speed direct drive wind turbines as solid disks are easier to manufacture and are more structurally sound.

5.8 Losses and Efficiency

FE is used to calculate the losses in various part of the machine as deducing them by measurement is difficult. Table 13 gives the FE calculated losses in the AFPM machine. In

order to attain the required output power, the copper losses had to be increased due to the high rotor losses. The no-load losses can be verified by measurement results from the no-load test. The measured and FE efficiencies are given in Table 14 and the results both show low machine efficiency. Had a laminated steel rotor disk been used, the machine efficiency could be increased up to 89 % and even higher by reducing the magnet loss by segmentation.

Table 13. FE Calculated Losses

	No-Load	On-Load
Copper [W]	0	1400
Stator Core [W]	25	59
Rotor Core [W]	390	900
Magnet [W]	180	330
Winding Eddy Current [W]	13.7	13.7
Wind and Friction [W]	75	75
Total [W]	683.7	2777.7
Measured [W]	565.5	n/a

Table 14. FE and Measured Efficiencies

	FE	Measured
Input Power [W]	18778	19364
Output Power [W]	16000	16022
Losses [W]	2778	3342
Efficiency [%]	85.2	82.7

6. Conclusions and Recommendations

Many different in-wheel machine topologies are reviewed in this thesis along with different stator and rotor configurations. The machine topology selected for investigation was the single-sided axial flux PM machine with non-overlap windings and open stator slots. Two pole-slot combinations of this topology are explored; the 30-pole 27-slot and 30-pole 36-slot machines with single and double-layer non-overlap windings.

In this thesis it was found that optimising for power density is more appropriate than efficiency based optimisation, particularly for this application as the results show. A 16 kW, 30-pole 27-slot prototype machine with double-layer windings was built, and it met the design requirements, only falling short upon the maximum speed. The well known axial flux attraction force problems were encountered and they were overcome by suitable bearing selection and mechanical design. The prototype machine and FE results are found in good agreement affirming the use of FE as design technique. The main findings in this work that have significant contribution are that:

- By optimising the slot with ratio, magnet to pole pith ratio and tooth ratio in un-equal teeth machines very low torque ripple can be achieved. The lowest value obtained is 0.3 % by the double-layer 30-pole 36-slot machine. The single-layer 30-pole 36-slot machine un-equal teeth machine is close with 0.4 % and it has the best torque per ripple characteristic.

- From the cogging torque measurements, the theoretical and practical cogging torques are found contradictory. It is found that measured cogging torque does not have a simple period corresponding to the theoretical period. The measured cogging torque is found to be of lower frequency and higher amplitude. The reason for this is that practical machines are not ideal as assumed in FE due to material and manufacturing tolerances. To verify the measured result magnetic variations are introduced in the FE model and the results are found to be more realistic.

- The use of solid mild steel rotor disks is found unsuitable for this application due to the high rotor losses present in non-overlap PM machines; therefore the use of laminated steels is suggested.

6.1 Recommendations for Further Research

Although the objectives of this work have been realised, there are still some concerns and it is recommended that further research be done.

- The end winding cooling method used in prototype machine was found inadequate due to rudimentary construction and the use of poor thermal epoxies. It is recommended that axial flux cooling techniques be investigated further and with possible integration into the stator backing supports.

- PM machines losses, particular those generated by MMF harmonic components need to be further investigated. A method of linking the harmonics to an optimisation algorithm for reduction could yield new findings.

- The measurement method used for cogging torque was rather basic and could not capture the higher frequency components. A more precise method of measurement should be investigated.

- Further applications for the single-sided AFPM topology should be considered. One potential use could be in vertical axis wind generator applications. The low speeds enable the use of solid steel disks, and the attraction forces can be counter balanced by the mass of the blades and / or flywheel.

Appendix A: Bearing Calculations

In order to select a suitable bearing for the AFPM machine, the axial load due to mainly the attraction forces and the radial load mainly due to the vehicle weight had to be known. The axial load was found to be 11 000N and the radial load was taken as 7500 N. This equivalent load can be calculated by

$$P = XF_r + YF_a ,$$

where P is the equivalent load, F_r the radial load, F_a the axial load, X the radial load factor and Y the axial load factor. The values of X and Y are obtainable from bearing tables. From bearing tables, a suitable bearing is chosen and then its equivalent loading is calculated. If the equivalent bearing loading is less than the manufacturers permissible dynamic load factor C, and providing the bearing would yield a suitable life span given by fatigue factor

$$f_h = f_n \frac{C}{P},$$

where f_n is the speed factor. The task is quite iterative as often several bearing have to be checked until a suitable one is found. For use in this project, two SKF 3308 double row angular contact bearing is used. The bearings has dynamic load rating C = 64 000 N, static rating C_0 of 44 000 N and fatigue load point of 1860 N.

The equivalent dynamic load for each bearing was calculated as P = 12 121 N, a loading of about 20 % of the maximum. The fatigue factor was calculated as 1.32, corresponding to basic life of 2453 hours. Assuming a constant speed of 100 km/h, this bearing life would yield over 245 300 km, a very reasonable range. In order to calculate bearing losses, first the frictional moment M must be calculated, given by

$$M = 0.5\mu Pd ,$$

where μ is the bearing constant coefficient of friction and d the bearing bore diameter. For the loading case, with μ = 0.0024, the frictional moment is found to be 0.5818 Nm. With the friction moment know, the power loss can be obtained by

$$N_R = 1.05 \times 10^{-4} Mn ,$$

with n the rotational speed. For a speed of 1000 r/min, the power loss was calculated to be 35.54 W for each bearing, 71.08 W in total.

Appendix B: Finite Element Program

The FEM analysis involves four main steps to obtain a solution.

Pre-processing

This is the initial setup involving modelling of the machine structure and material properties, setup of Dirichlet and Neumann boundary conditions, calculation of the magnetising currents, and estimation of the losses in the magnetic circuit.

Meshing

Mesh generation involves division of machine cross-section into a set of triangular elements. The accuracy of the FE solution is dependent on the topology of the mesh, thus, attention should be paid in the creation of the mesh.

Solving

Here the magnetic vector potentials at different nodes are solved for by Newton-Raphson method. It involves a set of non-linear equations due to the non-linearity of the magnetic materials.

Post-processing

From the solution of the nodal magnetic vector potentials, the flux linkages, inductances, airgap flux density and the torque of the machine can be calculated.

B.1 Magnetic Vector Potential

When working with 2D finite element models, the magnetic vector potential A at the Razek nodes is directed only along the Z direction, given in the Cartesian coordinates as

$$A = A(x, y) \cdot a_z ,$$

where a_z is the z-directed unit vector. The airgap magnetic flux density distribution in FE is calculated by taking the partial derivative of the vector potential along the linear model given by

$$B_{gap_y} = \frac{\partial A}{\partial x} .$$

B.2 Flux Linkage

The magnetic flux linkage linking a winding is also calculated based upon the magnetic vector potential. By using the relation

$$B = \nabla \times A,$$

and by substituting into the Stoke's theorem, the flux through a surface S is

$$\begin{aligned}\Phi &= \int_S B \cdot dS \\ &= \int_S \nabla \times A \cdot dS \\ &= \int_C A \cdot dl\end{aligned}$$

In finite element turns, the flux linkage for a phase winding is [47]

$$\lambda_\phi = \frac{2pzl}{n_a S} \sum_{j=1}^{u} \left(\frac{\Delta_j \zeta}{3} A_{ij} \right),$$

where z is the number of turns, l the active length, n_a the number of meshed coil elements, u the number of meshed coil elements in the pole region, S the surface area, Δ_j the area of triangular element j, $\zeta = \pm 1$ the integration direction in or out of the Z-plane, and A_{ij} the magnetic vector potential at node i of triangular element j.

B.3 Instantaneous Torque: Virtual Work Method

For instantaneous torque calculations and in order to obtain precise waveforms to observe torque quality in electromagnetic circuits there are computational methods such as the Virtual Work and Maxwell stress Tensor method.

As a magnetic circuit changes form during operation, the principle of virtual work can be used to estimate force and torque. The instantaneous torque of an electrical machine can be calculated by the co-energy method given by

$$T_{VW} = \frac{dW'}{ds} \cdot r_{avg} = \frac{\Delta W'}{\Delta s} \cdot r_{avg}.$$

Where W' is the magnetic co-energy, r_{avg} the average airgap radius, and s some small displacement.

B.4 Instantaneous Torque: Maxwell Stress Tensor

The Maxwell Stress Tensor is an alternative to the Virtual Work method, and is faster in that it requires only one FE solution as opposed to two. The torque by the Maxwell Stress Tensor method is given by

$$T = \frac{p r_{avg}{}^2 L}{\mu_0} \int_{\theta_1}^{\theta_2} B_r B_\theta d\theta,$$

where p is the number of pole pairs, L the machine axial length, and B_r and B_θ the flux density components from the macro air-gap element.

For some investigations requiring instantaneous torque profiling; particularly torque quality. The average torque results are ineffective for torque profiling as the result is simply just that, an average. The Maxwell Stress Tensor and Virtual work methods instead give instantaneous values during machine rotation. A comparison of the two methods is shown in Figure 93. From the result, it can be seen that the two methods are very identical, with the Virtual Work method giving a higher result by only 1 Nm.

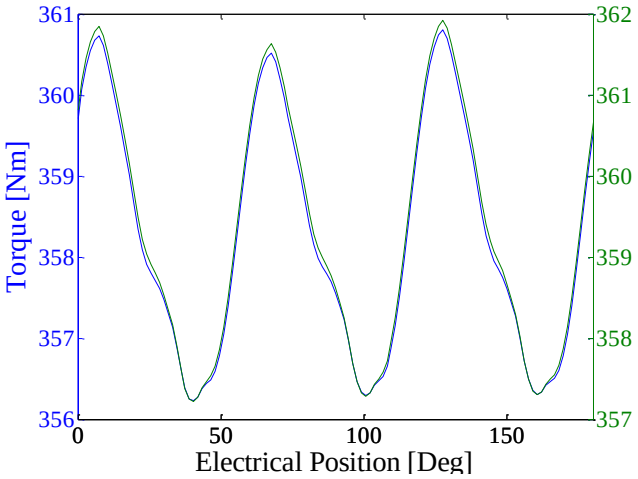

Figure 93. Instantaneous torque using Virtual Work and Maxwell Stress Tensor methods.

Appendix C: FE Strength Analysis

The attractive force between the stator and rotor in single-sided AFPMs is a serious drawback for the topology. These forces cause bending of the rotor and stator support structures and must be evaluated. The attractive forces can be determined analytically by [12]

$$A_F = \frac{B_g^2 S_m \alpha_m}{2\mu_0},$$

where A_F is the attraction force, B_g the flux density in the airgap, S_m the airgap surface area, α_m the percentage of magnet to airgap area, and μ_0 the permeability of free space. Finite element analysis can also be used to calculate the attraction force and the structural integrity of the rotor disk.

The electromagnetic FE solution of the 30-pole 27-slot model attraction force by Infolytica Magnet 6® is shown in Figure 94. The attraction force varies as the machine rotates due to the permeance variations. For this analysis the maximum value is value is taken and multiplied by 3 (1/3rd FE model). This yields an attraction force of 7680 N.

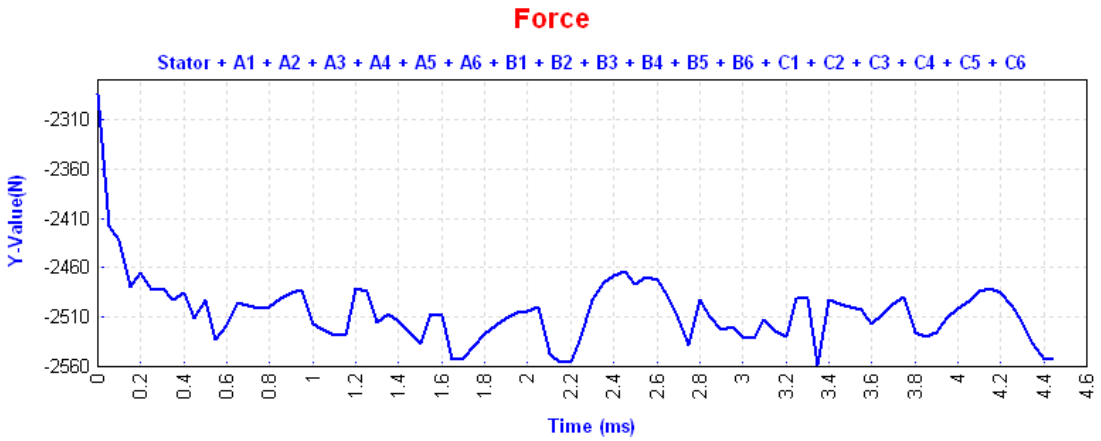

Figure 94. FE attraction force.

Further structural FE analysis using Autodesk Inventor® (ANSYS based) is used to evaluate deformation caused by the attraction force shown in Figure 95. The Young's Modulus of the mild steel disk used is 2.2 x 10^5 MPa. The maximum deformation found is 0.0268 mm, leading to a 1.68 % reduction in the machine airgap, which is well within limits. Figure 96 shows the structural FE result if only the inner magnet material is completely cut through.

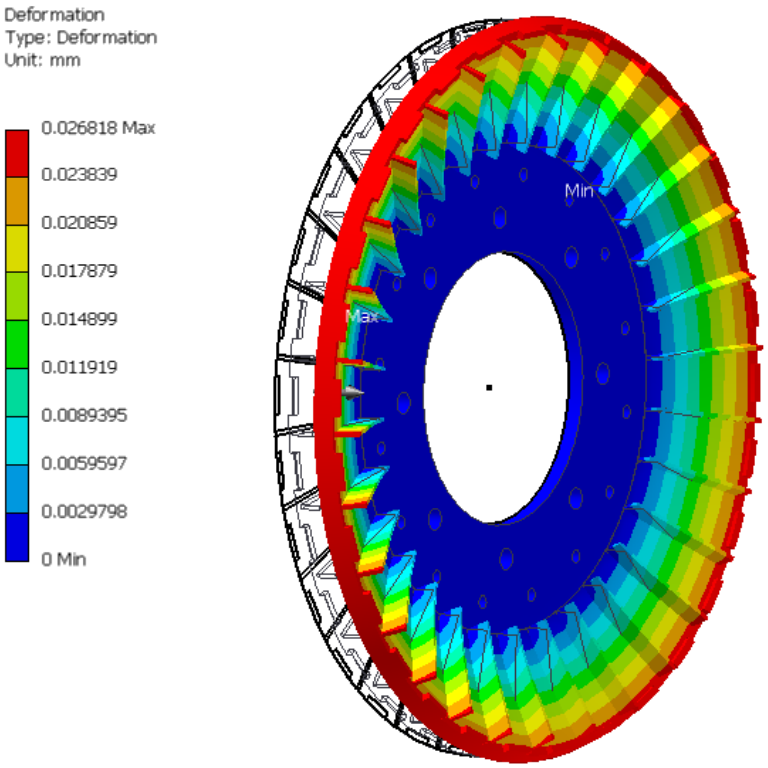

Figure 95. Structural FE rotor deformation due to attraction forces.

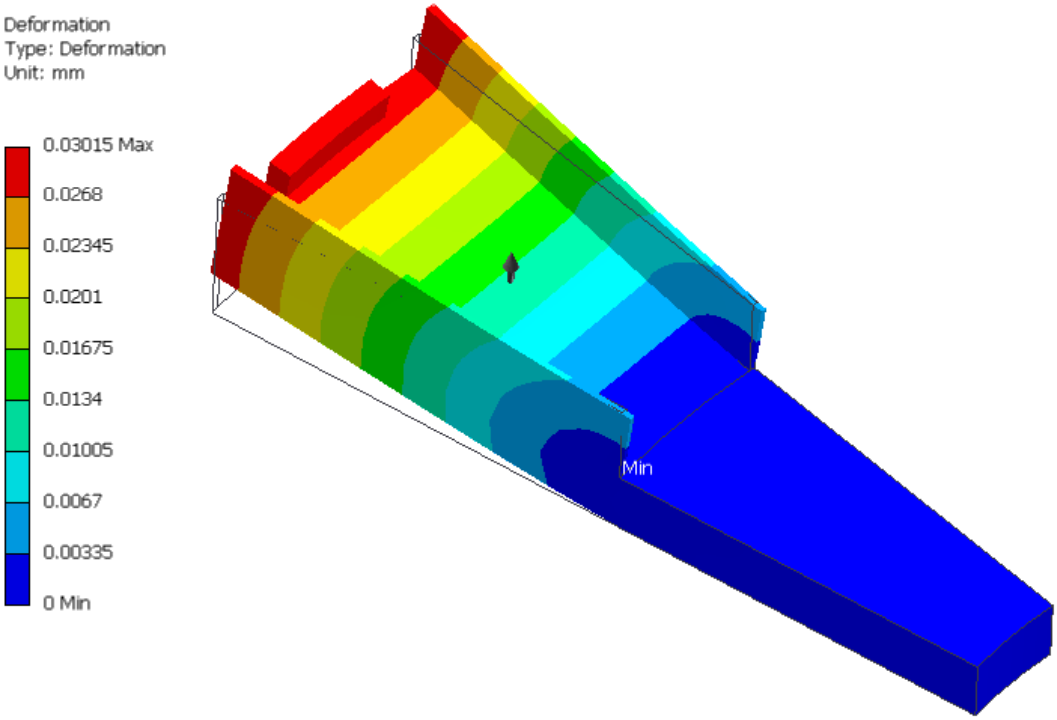

Figure 96. Structural FE deformation of rotor disk with complete inner magnet cut.

Appendix D: Radial and Axial Flux Prototype Specifications

Previously at the Stellenbosch University, a radial flux prototype hub drive machine was built as part of doctoral research project. The prototype radial machine has almost the exact properties of the axial flux machine built in this research. Both prototype machines feature same pole/slot combination and power level. The main differences between the two machine are the dimensions, slot configuration and steel materials. One aim of this research is to try and have the machines built as similar as possible to each other, but this is not possible due to certain constraints. In terms of outer dimensions, axial flux machines take on a flat pancake shape whereas radial flux machines are a more cylindrical shape. One machines design could not be constrained to the others dimensions as each machine is optimal in its own profile. The slot configuration of the axial flux machine could no take on a semi-closed shape due to the complexity in manufacturing and materials wise, tape wound toroidal core of 0.5mm M36 type steel could not be sourced and 0.3mm M3 GOSS steel had to be used instead. For the rotor yoke of the axial flux machine, a narrow laminated steel toroid (6mm) could not be sourced, therefore a solid mild steel disk was used instead. Table 15 presents the specifications of the two machines and the reader can draw further from the results.

Table 15. Specifications of 30-Pole 27-Slot RFPM and AFPM Prototype Machines

	HM2	AFPM2
Rated (base) speed	450 r/min	450 r/min
Rated (base) frequency	112.5 Hz	112.5 Hz
Rated Torque	340 Nm	340 Nm
No-load (open circuit) line voltage	274 V	274 V
Rated line current	53 A (rms)	44 A (rms)
Rated current density	11.5 A (rms) / m^2	11.5 A (rms) / m^2
Rated mechanical output power	16 kW	16 kW
Rated power factor	0.916 (lagging)	0.922 (lagging)
Rated stator copper losses	1.2 kW	1.2 kW
Rated wind and friction losses	50 W	75 W
Rated total open circuit losses	200 W	500 W
Rated total losses	1.4 kW	3.3 kW
Number of poles	30	30
Number of stator slots	27	27
Number of stator coils	27	27
Number of turns per coil	51	101

Number of parallel circuits	3	3
Connection of 3-phase stator	Star	Star
Stack length	100.0 mm	65.0 mm
Stator axial length	100.0 mm	38.0 mm
Total axial length	100.0 mm	53.25 mm
Total radial length	54.04 mm	65.0 mm
Stator outer diameter	244.2 mm	330 mm
Stator inner diameter	162 mm	224 mm
Stator slot width	11.735 mm	20.5 mm
Stator slot height	31.59 mm	29.0 mm
Stator yoke height	5.9 mm	6.0 mm
Stator coil side width	5.9 mm	10.25 mm
Stator conductor diameter	1.4 mm	1.25 mm
Stator conductor fill factor	0.386	0.41
Synchronous inductance per phase	2.816 mH	4.32 mH
Synchronous reactance per phase	2.0 Ω	3.05 Ω
Resistance per phase	142 mΩ	230 mΩ
Air gap length	1.4 mm	1.4 mm
Average air gap diameter	245.6 mm	277.0 mm (avg)
Rotor outer diameter	270 mm	330 mm
Rotor inner diameter	162 mm	224 mm
Rotor magnet height	5.6 mm	10.6 mm
Ratio of magnet pitch to pole pitch	0.9	0.94
Number of rotor magnet segments	1	1
Rotor yoke height	5.9 mm	8.0 mm
Stator core mass	10.66 kg	5.83 kg
Rotor yoke mass	4.04 kg	5.0 kg
Rotor magnet mass	3.31 kg	3.423 kg
Total Active Mass	18.01 kg	14.257 kg
Rotor permanent magnet type	N40SH sintered NdFeB	N40SH sintered NdFeB
Stator Lamination steel	26GaM19/C5	0.3 mm M5 GOSS
Rotor Lamination steel	26GaM19/C5	Mild steel
Active surface area	0.078 m^2	0.0541 m^2

Appendix E: Mechanical Layout

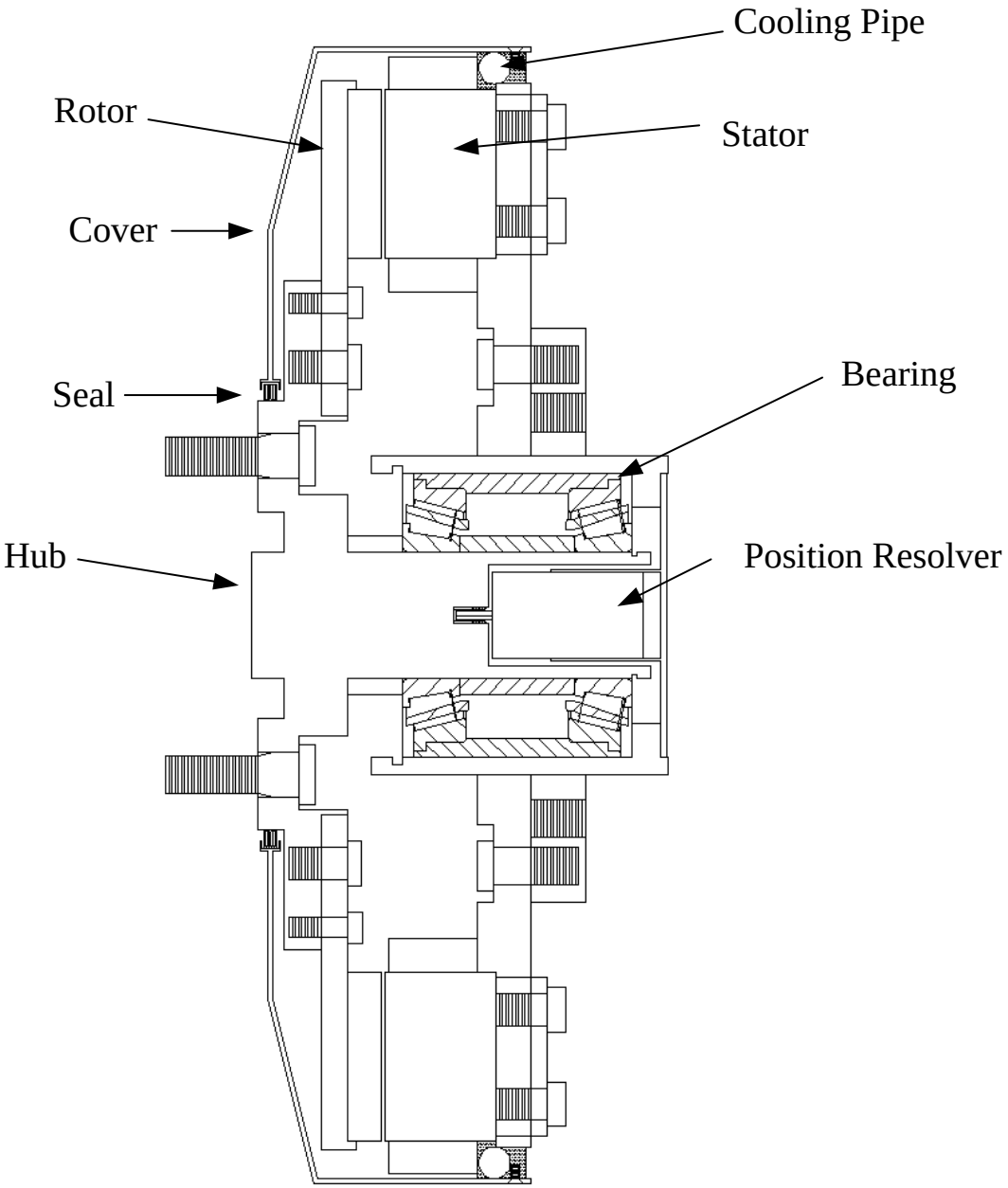

Figure 97. Mechanical cross section of AFPM prototype.

Appendix F: FE Thermal Analysis

F.1 Stator Winding

Finite Element analysis was also used to obtain the temperature distribution in the stator of the AFPM machine with assumed 1200 W copper losses in the windings. As can be seen in Figure 98 a maximum temperature of 157.6 °C in found in the copper windings. The temperature is acceptable as the maximum temperature rating of the API Class enamelled copper wire is 220 °C.

Material	Conductivity [W/m-K]	Convection [W/m2K]	Temp [°C]
Steel	20	*	*
Aluminium	180	*	*
Copper	386	*	*
Epoxy	0.5	*	*
Water	0.6	500	30
Air	*	10	30

* not applicable

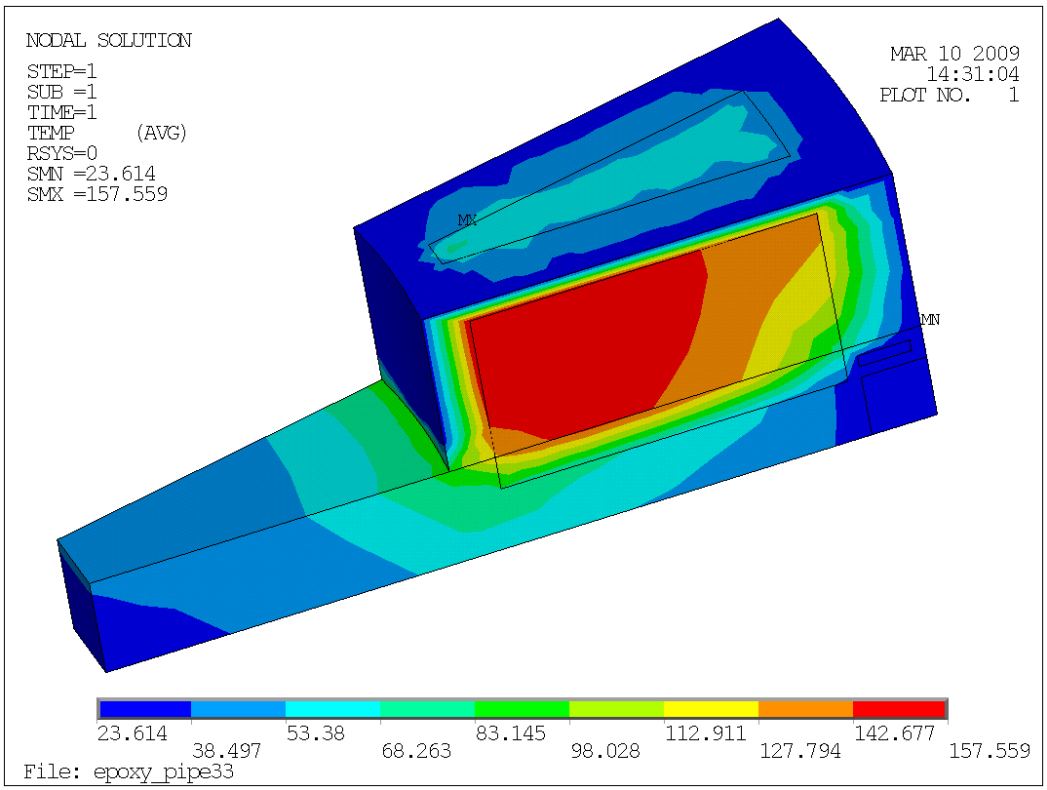

Figure 98. Thermal FE solution of AFPM machine with water cooling duct on outer end windings.

F.2 Rotor Disk

In order to find the temperature caused by the rotor eddy current losses in the rotor yoke FE is used. For the simulations the thermal conductivity of mild steel 20 W/m-K was used, along with air surface boundary conditions with film constant of 10 W/m^2K at temperature 30 °C. The FE result is shown in Figure 99 and the temperature found in 147.6 °C.

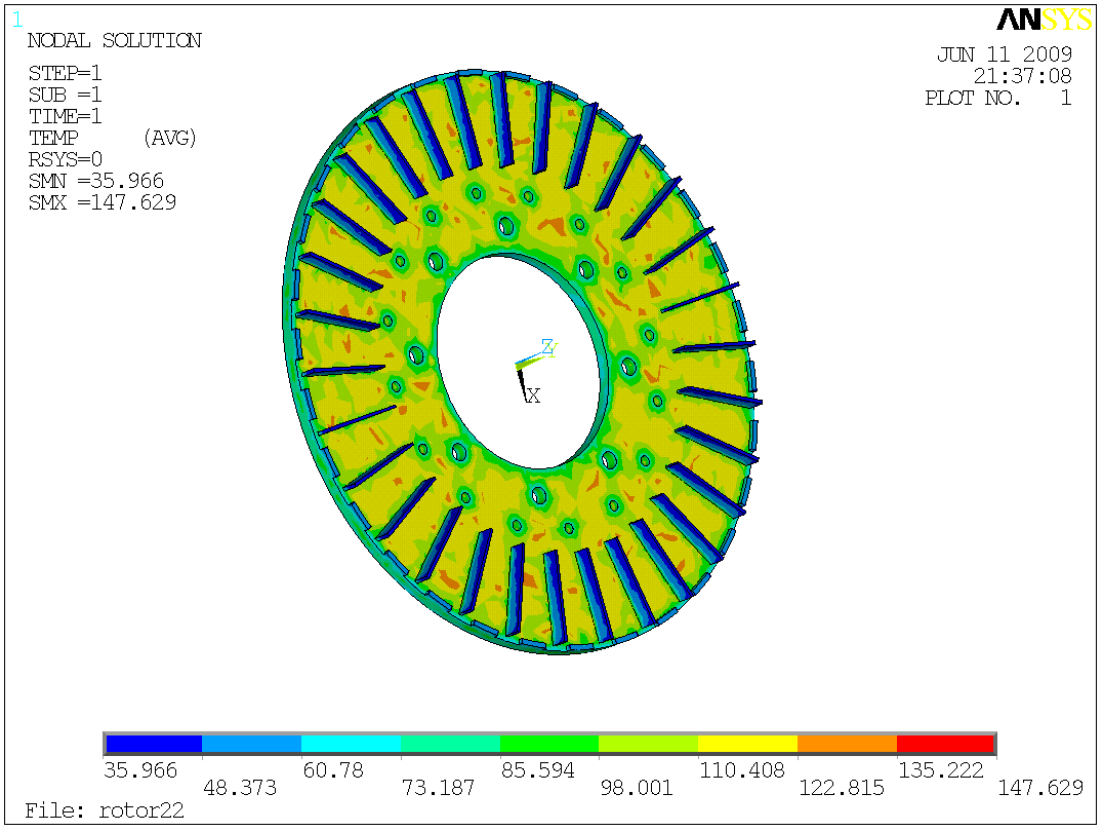

Figure 99. Thermal FE simulation of rotor losses.

Bibliography

[1] Toyota Motor Corporation, Japan.

[2] General Motor Corporation, Detroit, USA.

[3] Rahman K., Patel N., Ward T., Nagashima J., Caricchi F. and Crescimbini F., "Application of Direct-Drive Wheel Motor for Fuel Cell Electric Vehicle and Hybrid Electric Vehicle Propulsion System," IEEE Transactions on Industry Applications, Vol. 42, No. 5, September/October 2006.

[4] Raser Technologies, Inc., Utah, USA

[5] Protean Electric Ltd., Hampshire, UK

[6] Yang YP., Chuang DS., "Optimal Design and Control of a Wheel Motor for Electric Passenger Vehicle," IEEE Transactions on Magnetics, Vol. 43, No. 1, January 2007

[7] Patterson D. and Spèe R., "The Design and Development of an Axial Flux Permanent Magnet Brushless DC Motor for Wheel Drive in a Solar Powered Vehicle," IEEE Transactions on Industry Applications, vol. 31, no. 5, pp. 1054-1061, Sept./Oct. 1995.

[8] Wrobel R. and Mellor P., "Design Considerations of a Direct Drive Brushless PM Machine with Concentrated Windings," IEEE ICEM, pp. 655-658, May 2005.

[9] Caricchi F., Crescimbini F., Mezzetti F., Santini E., "Multistage Axial-Flux PM Machine for Wheel Direct Drive," IEEE Transactions on Industry Applications, Vol. 32, No. 4, July/August 1996.

[10] Hendershot J. R. Jr., Miller TJE, "Design of Brushless Permanent-Magnet Motors," Magna Physics Publishing and Clarendon Press, Oxford, 1994.

[11] Collocott S., Dunlop J., Gwan P., Kalan B., Lovatt H., Wu W and Watterson P., "Application of Rare-Earth Permanent Magnets in Electrical Machines: From Motors for Niche Applications to Hybrid Electric Vehicles," China Magnet Symposium, Xi'an, China, May 2004.

[12] Gieras J. F., Wang R., Kamper M. J., "Axial Flux Permanent Magnet Machines," Kluwer Academic Publishers, The Netherlands, (2004)

[13] Aydin M., Huang S., Lipo T. A., "Axial Flux Permanent Magnet Disc Machines: A Review," Research Report, Wisconsin Power Electronics Research Centre, September 2004.

[14] Nasar S., "Permanent Magnet, Reluctance, and Self-Synchronous Motors," CRC Press Inc, 1993, Florida, USA.

[15] Magnussen and Sadarangani, "Winding Factors and Joule Losses of Permanent Magnet Machines with Concentrated Windings," IEEE IEMDC, pp. 333-339, June 2003.

[16] Zhu Q., Shi Y. and Howe D., "Comparison of Torque-speed Characteristics of Interior-magnet Machines in Brushless AC and DC modes for EV/HEV Applications," Journal of Asian Electric Vehicles, vol. 4, no. 1, June 2006.

[17] Campbell P., "The Magnetic Circuit of an Axial Field D.C. Electrical Machine," IEEE Trans. Magnetics, vol. Mag-11, no. 5, pp. 1541-1543, Sept. 1975.

[18] Sitapati K., Krishnan R., "Performance Comparisons of Radial and Axial Field, Permanent Magnet, Brushless Machines," IEEE Transactions on Industry Applications, Vol. 37, No. 5, September / October 2001

[19] Huang S., Luo J., Leonardi F., Lipo T., "A General Approach to Sizing and Power Density Equations for Comparison of Electrical Machines," IEEE Transactions on Industry Applications, Vol. 34, No. 1, January/February 1998

[20] Cavagnino A., Lazzari M., Profumo F., Tenconi A., "A Comparison Between the Axial Flux and the Radial Flux Structures for PM Synchronous Motors," IEEE Transactions on Industry Applications, Vol. 38, No. 6, November/December 2002

[21] Huang S., Luo, J., Leonardi F., Lipo T. A., "A Comparison of Power Density for Axial Flux Machines Based on General Purpose Sizing Equations," IEEE Transactions on Energy Conversion, Vol. 14, No. 2, June 1999

[22] Profumo F., Zhang Z., Tenconi A., "Axial Flux Machines Drives: A New Viable Solution for Electric Cars," IEEE Transactions on Industry Electronics, Vol. 44, No. 1, February 1997

[23] Sitapati K., Krishnan R., "Performance Comparisons of Radial and Axial Field, Permanent Magnet, Brushless Machines," IEEE Transactions on Industry Applications, Vol. 37, No. 5, September / October 2001

[24] SimÕes M. G., Vieira P. Jr., "A High-Torque Low-Speed Multiphase Brushless Machine – A Perspective Application for Electric Vehicles," IEEE Transactions on Industry Electronics, Vol. 49, No. 5, October 2002

[25] Chul Oh S., Emadi A., "Test and Simulation of Axial Flux – Motor Characteristics for Hybrid Electric Vehicles," IEEE Transactions on Vehicular Technology, Vol. 53, No. 3, May 2004

[26] Larmine J., Lowry J., "Electric Vehicle Technology Explained," John Wiley & Sons, England (2003)

[27] Terashima M., Ashikaga T., Mizuno T., Natori K., Fujiwara N., Yada M., "Novel Motors and Controllers for High Performance Electric Vehicle with Four In-Wheel Motors," IEEE Transactions on Industry Electronics, Vol. 44, No. 1, February, 1997

[28] Singh B., Singh B. P. and Dwivedi S., "A State of Art on Different Configurations of Permanent Magnet Brushless Machines," IE(I) Journal-EL, vol. 87, pp. 63-73, June 2006.

[29] Staunton S., Nelson S., Otaduy P., McKeever J., Bailey J., Das S. and Smith R., "PM Motor Parametric Design Analyses For a Hybrid Electric Vehicle Traction Drive Application," Oak Ridge National Laboratory, Report for United States Department of Energy, 2004.

[30] Salminen P., Niemelä M. and Pyrhönen J.,"High-Torque Low-Torque-Ripple Fractional-Slot PM-Motors," IEEE ICEM, pp. 143-148, May 2005.

[31] Colton J., Patterson D. and Hudgins J., "Design of a Low-Cost and Efficient Integrated Starter-Alternator," IEEE PEMD Conference, pp.357-361, April 2008.

[32] Neji R., Tounsi S. and Sellami F., "Contribution to the Definition of a Permanent Magnet Motor with Reduced Production Cost for the Electric Vehicle Propulsion," European Transactions on Electrical Power, vol. 16, pp. 437-460, 2006.

[33] Salminen P., Pyrhönen J., Libert F. and Soulard J., "Torque Ripple of Permanent Magnet Machines with Concentrated Windings," ISEF, Spain, Sept. 2005.

[34] Rix A., Kamper M. J., Wang R., "Torque Ripple and Flux Density Variation Due to Stator Slot Opening of Concentrated Coil Permanent Magnet Machine," SAUPEC

[35] Electron Energy Corporation, Landisville, PA, USA

[36] Krause P. C., "Analysis of Electric Machinery," McGraw-Hill Book Company,

[37] de Kock H., Rix A. J. and Kamper M. J., "Optimal Torque Control of Interior Permanent Magnet Synchronous Machines in the Full Speed Range," IEEE ICEM, September 2008.

[38] Kamper M. J., Rix A. J., Wills D. A., Wang R., "Formulation, Finite-Element Modelling and Winding Factors of Non-Overlap Winding Permanent Magnet Machines," IEEE ECEM, September 2008.

[39] Bianchi N., Dai Prè M., Alberti L. and Fornasiero E., "Theory and Design of Fractional-Slot PM Machines," IEEE-IAS Tutorial Course Notes, September 2007.

[40] Bianchi N., Bolognani S., Dai Prè M. and Grezzani G., "Design Considerations for Fractional-Slot Winding Configurations of Synchronous Machines," IEEE Trans. Ind. Appl., vol. 42, no. 4, pp. 997-1006, Jul./Aug. 2006.

[41] Bianchi N., Bolognani S. and Dai Prè M., "Magnetic Loading of Fractional-Slot Three-Phase PM Motors With Nonoverlapped Coils," IEEE Trans. Ind. Applications, vol. 44, no. 5, pp. 1513-1521, Sept./Oct. 2008.

[42] Ishak D., Shu Z. and Howe D., "Comparison of PM Brushless Motors, Having Either All Teeth or Alternate Teeth Wound," IEEE Trans. Energy Conservation, vol. 21, no. 1, pp. 95-103, Mar. 2006.

[43] Magnussen F. and Lendenmann H., "Parasitic Effects in PM Machines With Concentrated Windings," IEEE Trans. Ind. Applications, vol. 43, no. 5, pp. 1223-1232, Sept./Oct. 2007.

[44] Wang R. J., "Design Aspects and Optimisation of an Axial Field Permanent Magnet Machine with an Ironless Stator," PhD Dissertation, Stellenbosch University, 2003.

[45] Skaar S., Krøvel Ø., Nilssen R., "Distribution, coil-span and winding factors for PM machines with concentrated windings," IEEE ICEM September 2006.

[46] Hwang C., Wu M. and Cheng S., "Influence of pole and slot combinations on cogging torque in fractional slot PM motors," Journal of Magnetism and Magnetic Materials 304, e430-e432, 2006.

[47] Kamper M. J., "Design Optimisation of Cageless Flux Barrier Rotor Reluctance Synchronous Machine," PhD Dissertation, Stellenbosch University, 1996.

[48] Atallah K., Howe D., Mellor P. H. and Stone D. A., "Rotor Loss in Permanent-Magnet Brushless AC Machines," IEEE Trans Ind. Applications, vol. 36, no. 6, pp. 1612-1618, Nov/Dec 2000.

[49] Toda H., Xia Z., Wang J., Atallah K. and Howe D., "Rotor Eddy-Current Loss in Permanent Magnet Brushless Machines," IEEE Trans. Magnetics, vol. 40, no. 4, July 2004.

[50] Jussila H., Salminen P., Parviainen A., Nerg J. and Pyrhönen J., "Concentrated Winding Axial Flux Permanent Magnet Motor with Plastic Bonded Magnets and Sintered Segmented Magnets," IEEE ICEM, September 2008.

[51] Bottauscio O., Pellegrino G., Guglielmi P., Chiampi M. and Vagati A., "Rotor Loss Estimation in Permanent Magnet Machines With Concentrated Windings," IEEE Trans. Magnetics, vol. 41, no. 10, October 2005.

[52] Aydin M., Huang S. and Lipo T., "Torque Quality and Comparison of Internal and External Rotor Axial Flux Surface-Magnet Disk Machines," IEEE Trans. Ind. Electronics, vol. 53, no. 3, pp. 822-830, June 2006.

[53] Jahns T. and Soong W., "Pulsating Torque Minimization Techniques for Permanent Magnet AC Motor Drives - A Review," IEEE Trans. Ind. Applications, vol. 43, no. 2, pp. 321-330, April 1996.

[54] Zhu Z. Q. and Howe D., "Influence of Design Parameters on Cogging Torque in Permanent Magnet Machines," IEEE Trans. Energy Conservation, vol. 15, no. 4, pp. 407-412, Dec. 2000.

[55] Caricchi F., Capponi F., Crescimbini F. and Selero L., "Experimental Study on Reducing Cogging Torque and Core Power Loss in Axial-Flux Permanent-Magnet Machines with Slotted Winding," IEEE Trans. Ind. Applications, vol. 2,no. 2, pp. 1295-1302, 2002.

[56] Aydin M., Zhu Z., Lipo T. and Howe D., "Minimization of Cogging Torque in Axial-Flux Permanent-Magnet Machines: Design Concepts," IEEE Trans. Magnetics, vol. 43, no. 9, pp. 3614-3622, September 2007.

[57] Bianchi N. and Bolognani S., "Design Techniques for Reducing the Cogging Torque in Surface-Mounted PM Motors," IEEE Trans. Ind. Applications, vol. 38, no. 5, pp. 1259-1265, Sept./Oct. 2002.

[58] Cros J., Viarouge P. and Gelinas C., "Design of PM Brushless Motors Using Iron-Resin Composites for Automotive Applications," IEEE Trans. Ind. Applications, vol. 1, no. 1, pp. 5-11, October 1998.

[59] Cros J. and Viarouge P., "Synthesis of High Performance PM Motors With Concentrated Windings," IEEE Trans. Energy Conservation, vol. 17, no. 2, pp. 248-253, June 2002.

[60] Koch T. and Binder A., "Permanent Magnet Machines with Fractional Slot Windings for Electric Traction," IEEE ICEM, 2002.

[61] Ishak D., Zhu Z. and Howe D., "Permanent-Magnet Brushless Machines With Unequal Tooth Widths and Similar Slot Pole Numbers," IEEE Trans. Ind. Appl., vol. 41, no. 2, pp. 584-590, Mar./Apr. 2005.

[62] Parviainen A., Niemelä M. and Pyrhönen J., "Modeling of Axial Flux Permanent-Magnet Machines," IEEE Trans. Ind. Applications, vol. 40, no. 5, pp. 1333-1340, Sept./Oct. 2004.

[63] Taizhou Sanmin Special Motor Co., Ltd, China.

[64] Riesen D., Schlensok C., Schmülling B., Schöning M. and Hameyer K., "Cogging Torque Analysis on PM-Machines by Simulation and Measurement," Technisches Messen Journal, vol. 74, pp. 393-401, August 2007.